Università degli Studi di Trieste

XXXI Ciclo del Dottorato di Ricerca in Earth Science and Fluid Mechanics

MEANDERING

Part 1: Turbulent Mixing in Sharp Meander Bends
Part 2: Mathematical Model for Meandering Rivers with Spatial Width Variations

Settore scientifico-disciplinare: ICAR/01

Ph.D. Student:	Francesca Campomaggiore
Ph.D. Program Coordinator:	Prof. Pierpaolo Omari
Thesis Supervisor:	Prof. Vincenzo Armenio
Thesis Co-Supervisor:	Prof. Stefano Lanzoni

Academic Year 2017-2018

Author: Francesca Campomaggiore

e-mail: francesca.campom@gmail.com

Affilation: Doctoral School in
"Earth Science and Fluid Mechanics".
Dipartimento di Ingegneria e Architettura,
University of Trieste, Piazzale Europa 1,
I-34127 Trieste, Italy

Supervisor: Prof. Vincenzo Armenio

e-mail: armenio@dica.units.it

Affilation: Dipartimento di Ingegneria e Architettura,
University of Trieste, Piazzale Europa 1,
I-34127 Trieste, Italy

Co-Supervisor: Prof. Stefano Lanzoni

e-mail: stefano.lanzoni@dicea.unipd.it

Affilation: Dipartimento di Ingegneria Civile Edile ed Ambientale,
University of Padua, via Loredan 20,
I-35131 Padova, Italy

to **myself***:*

"Never be afraid of the difficulty you encounter.
Remember that the kite rises with the opposite wind,
never with that in favour ..."

(Anonymous)
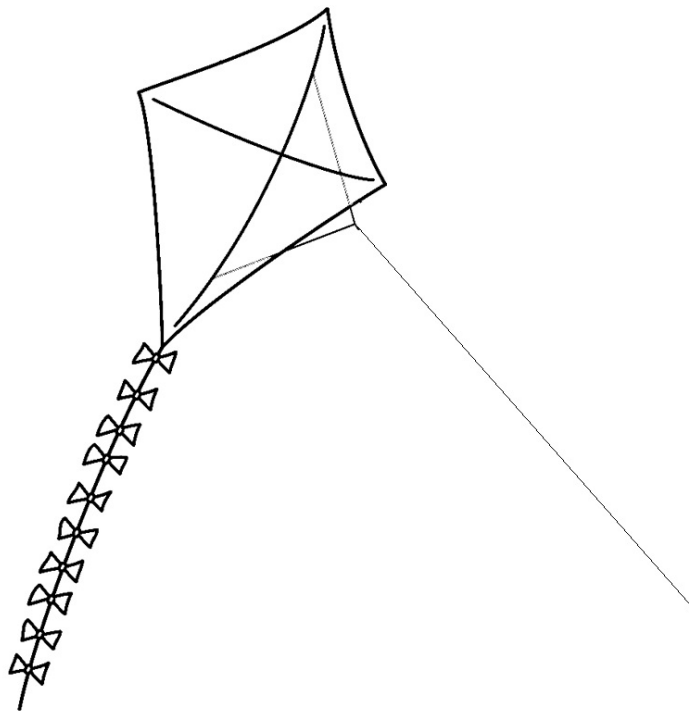
Abstract

This thesis concerns the investigation of the meandering phenomena, focusing on the hydrodynamic (Part I) and on the morphodynamic (Part II) of meandering rivers.

In the first part of this work, sharp curved single-bend open channel flow with a flat bed, representative of the early phase of bed erosion, is investigated by the use of Large Eddy Simulation (LES). The three-dimensional (3D) numerical simulation can provide flow field information that are difficult to obtain in the laboratory or in a real river. The focus is to provide insight into the physics of sharp meandering bends, highlighting the main flow and secondary flow characteristics and the role of turbulence. The latter plays an important role in many processes that are key in natural rivers, such as the phenomena of spreading and mixing of suspended matter, of sediment transport and scour processes. Turbulence affects the strength of the curvature-induced secondary flow in the core of the flow domain, a typical feature of curved open-channel flow. It rules the intensity of the bed shear stresses and the friction losses along the bend. It is especially important in the flow regions near the banks, affecting the stability of the channel banks. At the inner bank, the model predicts, rather accurately, the boundary layer detachment and the formation of an internal shear layer. Furthermore, the model adequately reproduces the outer-bank cell of secondary flow and the local increase of turbulent kinetic energy. In this work, two curved channels are investigated with the intent to underline the influence of the water depth on the flow features. Finally, the effects of the super-elevation of the free

surface on the meandering hydrodynamics are analysed using a Detached Eddy Simulation (DES) model available in the free software OpenFOAM.

In the second part of this work, a mathematical model for meandering rivers with spatial width variations is developed. The mathematical modelling of the long-term evolution of meandering rivers needs an efficient computation of the flow field. Therefore, the development of a mathematical model based on the complete response of a meandering river to spatially varying channel axis curvature and width is necessary. For this purpose, we elaborate a morphodynamic model able to predict the spatial distribution of the flow field and the equilibrium bed configuration of an alluvial river characterized by arbitrary distributions of both the channel axis curvature and the channel width. Owing to analytical character of the model, it provides a computationally efficient tool that can be easily incorporated in long-term river planform evolution models. Furthermore, it can be used to rapidly evaluate the morphological tendencies of an alluvial river in response to variations in planform geometry or hydrodynamic forcing. The model is tested by comparison with the bed topography observed in a typical reach of the Po River, showing that in presence of wide, mildly curved and long bend and weak width variations, the river topography is described with a good accuracy.

Contents

List of Figures

II   Mathematical model for meandering rivers with spatial width   62

List of Tables

Chapter 1

Meandering

Most of the rivers are of alluvial origin, that is, they are formed in materials that have been and can be transported by the stream. Furthermore, alluvial rivers can continually undergo modification of their position and planform shape with time, as a consequence of hydraulic forces exerted on the bed and banks. These changes may be gradual or rapid and may be the result of natural causes or human activities [54]. Natural rivers may be classified according to the planimetric evolution of their patterns. They are rarely straight, rather display a single-channel, sinuous planform (*meandering rivers*, see Figure 1.1(a)) or consist of a network of interconnecting channels (*braiding rivers*, see Figure 1.1(b)).

The most fascinating of these patterns is river meandering. The name "meander" derives from the Greek $M\alpha\iota\alpha\nu\delta\rho o\varsigma$ (*maiandros*) which is found for the first time in the Greek literature and exactly in Homer's Iliad (book 2, line 869: "The sons of Nomion were from near the waters of *Maiandros* and led the Karians to Troy."). Meander formation typically occurs for those rivers characterized by relatively fine sediments in floodplains with low gradient. The bank erosion shifts outward the channel axis producing curvature, while the inner bend deposition tends to keep the river width rather constant. As a result, the channel centreline takes a variety of patterns, which impressive feature is their regularity. In this regard, we can report the Yalin
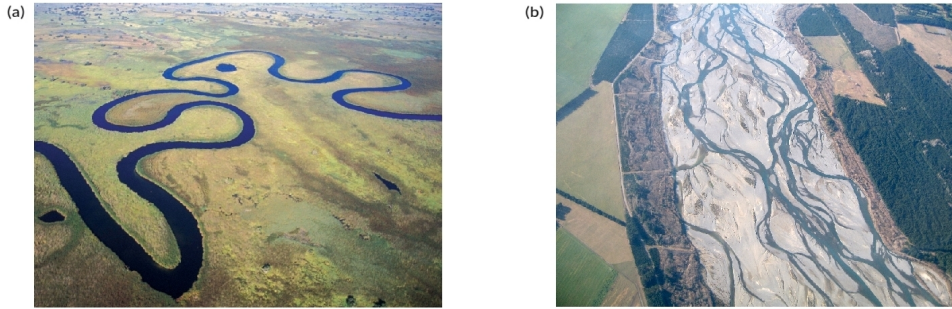
Figure 1.1: (a) River meandering: Okavango River in Africa (Source: http://www.botswanatourism.co.bw/explore/okavango-delta).
(b) River braiding: Waimakariri River in the South Island of New Zealand (Source: https://commons.wikimedia.org/wiki/File:Waimakariri01_gobeirne.jpg, photo by Greg O'Beirne).

[99] definition about the meandering, as a "self-induced plan deformation of a stream that is (ideally) periodic and anti-symmetrical with respect to an axis, x say, which may or may not be exactly straight". Thus, the meandering is a pattern which offers a fascinating example of the nature ability to develop highly regular forms.

The evolution of meandering rivers in nature undergoes a number of cyclic events. In the initial stage, meanders are weakly curved and coexist with migrating alternate bars. As the outer bank erosion progresses, meanders amplify and migrate typically downstream. This amplification eventually leads adjacent reaches of a meander loop to approach each other, until the stream undergoes a so called "neck cutoff" and the abandoned loop becomes an "oxbow lake" [17]. In Figure 1.2 we can observe a sketch of a river meander with its characteristic parts. The process of meander evolution, previously described, acts on periods of years, depending on the soil erodibility, and typically end with meander cutoff (see Figure 1.3).

An equally fascinating planform pattern is that of braiding river observed in wide rivers. Braiding rivers usually display steeper slopes and coarser
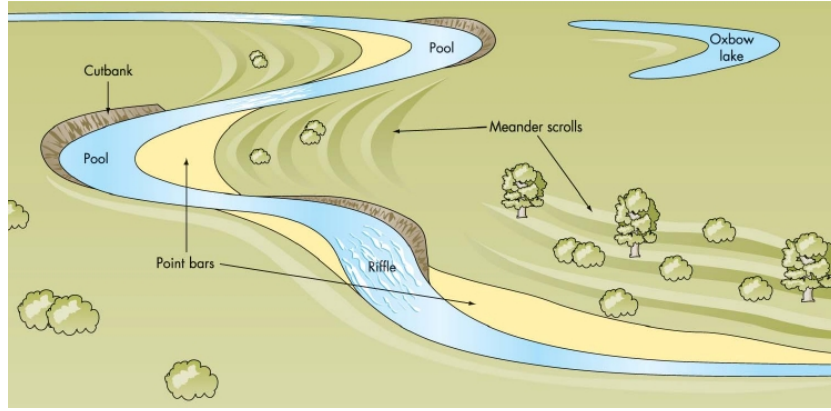
Figure 1.2: Sketch of a river meander.

grain size than meandering rivers. The stream of braiding rivers splits into a network of small channels (braids) separated by migrating bars, which may turn into fixed or temporary islands. Both channels and bars are typically highly mobile, such that the pattern of river may undergo significant changes after the flood events [17].

The rivers are very important for human civilization, they ensure the availability of water resources necessary for several human activities such as agriculture, transportations and power supply. Therefore, the study of meandering rivers, in particular, has attracted the attention of engineering and scientific communities from the end of the 19th century.

The aim of this work is to provide a further contribution to the knowledge of the charming world of the "Meandering". In particular, the text is organized in two parts focusing on the hydrodynamic (Part I) and on the morphodynamic (Part II) of meandering rivers.

In Part I, two sharp curved single-bend open channel flows with a flat bathymetry are investigated by the use of Large Eddy Simulations (LES)s employing the LES-COAST model. The focus is to provide insight into the physics of sharp meandering bends, highlighting the main and secondary flow characteristics, the role of turbulence and underlining the influence of the water depth on these flow features. Finally, an analysis on the influence

Figure 1.3: Timelapse of Pucallpa river in Perù from 1984 to 2016, images from Google Earth.

of the transverse inclination of the free surface on the flow field is conducted. In this regard, the freely available OpenFOAM software has been employed by means a Detached Eddy Simulation (DES).

In Part II, a mathematical model for meandering rivers with spatial width variations is developed. The goal is to improve an existing morphodynamic model able to predict the spatial distribution of the flow field and the equilibrium bed configuration of an alluvial river characterized by arbitrary distributions of both the channel axis curvature and the channel width. To this aim, the second order effect of the channel axis curvature and the interactions between channel axis curvatures and width variations are accounted for. In the end, the model is employed to evaluate the channel morphodynamics of the Italian Po River.

Part I

Turbulent mixing in sharp meander bends

Chapter 2

Introduction

Meandering river flows are characterized by important processes of interaction between the three-dimensional flow field, the bathymetry and the sediment transport. Therefore, the knowledge of hydrodynamic of meandering rivers is a major topic in environmental engineering and river management. It has many practical consequences, i.e. it affects the bank stability and the channel navigability, so the knowledge of 3D flow and a correct prediction of the planimetric evolution of the river can be useful in the design of river revitalization projects, the maintenance and optimization of navigation fairways, the improvement of ecological river functions, etc. For these reasons, the flow in meandering bends has been the subject of a number of recent experimental and theoretical studies focused on the analysis of the mean stream and the turbulence flow features. Actually, the tools mainly employed to predict flow, bathymetry and sediment transport in rivers are the two-dimensional (2D) depth-averaged models [38, 59]. These models yield satisfactory results in simplified river configurations, such as weakly to moderately curved open-channel bends. In literature several results are present of experimental studies on single-bend open-channel flows either through a rectangular cross-section or over deformed topography [6, 14, 66, 75]. These studies allowed to understand the mean flow and turbulence features in curved open channels, but they are often based on rather inaccurate velocity measurements

on coarse measuring grids. From the numerical point of view, Reynolds Averaged Navier Stokes equations are commonly used for the investigation of the meandering flows, although results are not always very satisfactory [27, 102, 93], especially in relation to the secondary flow pattern. In particular, the RANS models with isotropic turbulence closures are much less successful in predicting the details of the secondary flow and tend to overestimate the friction losses [92, 94].

In the past few decades, due to the significant enhancement in computational resources, increasing interest is emerging in the use of Large Eddy Simulation (LES) for the study of high Reynolds number flows. In literature there are many works in which LESs are employed to simulate straight open-channel flows [22, 23] and curved duct flows [61, 64, 82]. Conversely, LES has been rarely used to study curved channel flows which have higher width-to-depth ratio. Focusing on meandering open-channel flows, the following studies are worth of mention: Booij [19], Stoesser et al. [87] and Moncho-Esteve et al. [62] have performed measurements and LESs of flows in some curved flumes; van Balen et al. [93] have analysed the hydrodynamic of a mildly curved single-bend open-channel flow, while van Balen et al. [92] and Koken et al. [28] have studied the turbulence structure in a sharp meandering flow. Since LES directly resolves the anisotropic large scales of motion, it appears adequate to reproduce the velocity redistribution in open channel bends at conditions corresponding to the start of the scour and erosion process (flat bed). Therefore LES can be considered a powerful tool to study continuous spatial distribution of these types of flows, contrary to some cross-sections experimental studies.

Natural river flow can generally be reproduced as an high Reynolds number open-channel flow having a large aspect ratio (width-to-depth) and a strong local curvature. The principal feature of a meandering open channel flow is the establishment of a centrifugal secondary flow (also called helical flow or cross-stream circulation) that deeply influences the flow behaviour. This type of flow is highly three-dimensional and the cross-stream motion

is very important in terms of velocity redistribution, direction and magnitude of the boundary shear stresses and sediment transport. Thereby, the curvature-induced secondary flow affects the evolution of river bathymetry and planimetry and increases the turbulence activity enhancing the mixing and spreading of suspended matter like nutrients or contaminants. Most of previous research limited to weakly or moderate curved open-channels. However, the secondary flow, energy losses and turbulence tend to saturate in sharp bends. Accordingly, they do not grow proportionally to the relative curvature predicted by standard models. Understanding these processes is very important, but it is also hindered by the lack of observations and detailed experimental data.

In natural river flow, owing to the movable character of the bed, the near-bed turbulence determines the formation of ripples and/or dunes on the small scales. Instead, on large scales, the secondary flow strongly affects the topography of the bed especially in the curved parts of the river, where it enhances the ability of the flow to erode and transport sediments. It deviates the motion of sediments creating regions of sediment deposition, called "point bars", near to the inner bank of the bend and regions of sediment erosion, called "pools", at the outer bank of the bend (see Figure 1.2). In curved open channel with non-erodible bed, a "free vortex" effect prevails. The flow at the inner bend, initially, accelerates relative to the outer bend; proceeding downstream, secondary flow drives a net transfer of momentum toward the outer bend, hence the thread of high velocity progressively moves from the inner to the outer bend. Another important feature of the meandering flow is its capacity to separate from the inner bank of the flume bend with the consequent formation of internal shear layers, which are localized regions of large shear-driven turbulence production. In natural river, the formation of a convex bank flow separation has been noticed and measured. Ferguson et al. [35] and Blanckaert [8] argued on the influence of the inner bank flow separation on the outer bank flow. It increases the strength of the secondary currents affecting the sedimentation processes and the stability of erodible

channel banks. In order to better understand the complex behaviour of the river flow, it is often downscaled to laboratory dimensions. Although there are discrepancies between natural river flow and laboratory flume flow, this downscaling allows to investigate the hydrodynamic processes of meandering flow under optimized and controlled conditions.

In this work, we use the LES to highlight the role of the secondary flow and turbulence in a sharp curved single-bend open channel flow with a Re number typical of the laboratory-scale. The channel configuration was designed in order to highlight important processes that occur in natural rivers. In previous experimental investigations of curved channel (e.g. [5, 11, 12, 13, 15]), the ratio of centreline radius of curvature (R) to channel width (B) was larger than 3.5 ("mildly curved bends"). In this condition, the strength of the cross-stream motions is less important on the hydrodynamics of the flow. On contrary, in the present case the value of R/B is close to 1.3 ("sharp curved bend") and this condition determines an increase of the strength and importance of the secondary flow and the turbulence activity. This experiment was performed by Blanckaert [6, 9], whose analysis is mainly focused on the depth-averaged statistics and the role of the flow separation at convex banks. This configuration was also investigated numerically through a RANS model by Zeng et al. [102] and van Balen et al. [92]. However, the simulated flow showed a poor accuracy in predicting the velocity redistribution and the cross-stream motion within the channel.

Another aim of the present work is to investigate the influence of the water depth on the secondary flow distribution and the turbulence structures in sharp meandering open-channel flows. For this purpose, two different curved channels have been employed.

Finally, we also wanted to analyse the influence of the free surface on the hydrodynamics of the investigated curved channel and, in this regard, a DES has been employed. During recent years, DES has been shown to predict the mean flow and turbulence structure more accurately than wall-modeled LES for complex turbulent riverine flows. Of particular interest

are the works of Constantinescu et al. [27] and Koken et al. [52] in which DES was used to investigate the structure of turbulent flow and the sediment erosion mechanisms in an open channel bend of strong curvature with either deformed bed or flat bathymetry. The results of a work still in progress will be presented in the closure section of Part I.

The first part of the thesis is structured as follows. The numerical model and the turbulence closure model are described in Chapter 3, while the numerical domains as well as the boundary conditions are presented in Chapter 4. The analysis of the main flow, secondary flow and turbulence structures are elaborated in Chapters 5, 6 and 7, respectively. The prediction of the bed shear stress distribution is shown in Chapter 8. The influence of the transverse inclination of the free surface on the flow field characteristics is investigated in Chapter 9. The results obtained and the future goals are summarized in Chapter 10.

Chapter 3

Numerical method

3.1 LES-COAST model

LES-COAST model is used to perform LES of incompressible fully developed turbulent flows (see, e.g., [70]). It solves the curvilinear form of the Navier Stokes equations under the Boussinesq approximation (in case of stratified flow, where the density anomalies are small compared with velocity gradient).

Using LES methodology, the large, energy-carrying eddies are resolved completely while the small structures are modelled. In order to obtain the separation between large and small scales, the Navier-Stokes equations are filtered through an application of a spatial low-pass filter. The filtering operation reads as:

$$\overline{f}_i = \int_D G(x, x') f_i(x') dx' \tag{3.1}$$

where f is the flow field variable before the filtering, $\overline{f}$ is the filtered (or resolved) variable, D is the domain and G is the filter function. There are various kind of filter functions. In the present solver a top-hat filter is used, defined as:

$$G(x) = \begin{cases} 1/\overline{\Delta}, & \text{if } |x| \leq \overline{\Delta}/2 \\ 0, & \text{otherwise} \end{cases} \tag{3.2}$$

where $\overline{\Delta}$ is the filter width, defined as the grid cell size. The solution f_i will be the sum of the subgrid-scale (SGS) part f_i' and of the resolved part $\overline{f}_i$. The
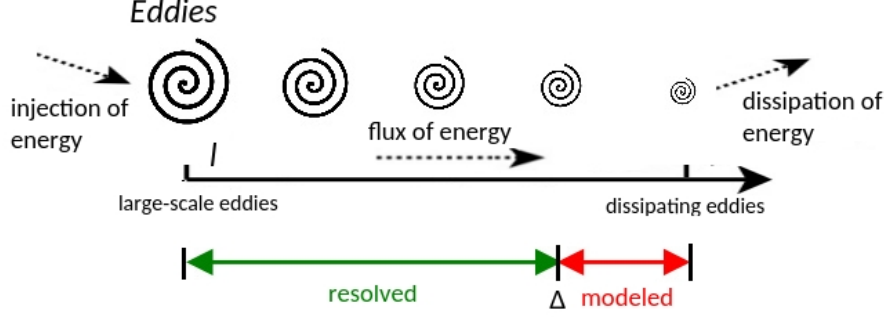
Figure 3.1: Sketch of LES methodology.

base concept of LES is shown in Figure 3.1: large-scale eddies continuously break up into smaller eddies until they are too small and they dissipate into heat. The eddies with length scale greater than Δ are directly resolved, while the smaller ones are modelled with a SGS model.

The Cartesian form of the filtered governing equations reads as:

$$\frac{\partial \overline{u}_j}{\partial x_j} = 0 \tag{3.3}$$

$$\frac{\partial \overline{u}_i}{\partial t} + \frac{\partial \overline{u}_j \overline{u}_i}{\partial x_j} = -\frac{1}{\rho_0} \frac{\partial \overline{p}}{\partial x_i} + \nu \frac{\partial^2 \overline{u}_i}{\partial x_j \partial x_j} - \frac{\partial \tau_{ij}}{\partial x_j} \tag{3.4}$$

They are the continuity and momentum equations, respectively. The symbol "$-$" represents the filtering operation, u_i is the i-th components of velocity vector (namely u, v and w), x_i is the i-direction space coordinate (namely x, y and z), t is time, p is the kinematic pressure divided by reference density ρ_0, ν is the kinematic viscosity and τ_{ij} are the SGS stresses which arise from the non linearity of the advection term.

3.1.1 Sub-grid scale model

In order to reproduce the flows motion properly on the sub-grid scale, the SGS stresses τ_{ij} are modeled by the dynamic eddy viscosity model described in Armenio and Piomelli [1]. The model is founded on the Germano identity [39], which relates subgrid-scale stresses computed at two different filter widths:

$$L_{ij} = T_{ij} - \widehat{\tau_{ij}} \tag{3.5}$$

in which the individual terms are defined as:

$$L_{ij} = \widehat{\overline{u}_i \overline{u}_j} - \widehat{\overline{u}}_i \widehat{\overline{u}}_j; \quad T_{ij} = \widehat{\overline{u}_i u_j} - \widehat{\overline{u}}_i \widehat{\overline{u}}_j \tag{3.6}$$

where $\overline{\cdot}$ represents filtering at scale $\overline{\Delta}$, whereas $\widehat{\cdot}$ represents filtering at scale $\widehat{\overline{\Delta}} > \overline{\Delta}$. The quantity L_{ij} is the "resolved turbulent stresses", instead the term T_{ij} is the "subtest scale stresses", that appears when the test filter is applied to the filtered Navier-Stokes Equations (3.3 and 3.4). The deviatoric part of τ_{ij} at scale $\overline{\Delta}$ is modelled as:

$$\tau_{ij} = -C_d 2\overline{\Delta}^2 |\overline{S}|\overline{S}_{ij} \tag{3.7}$$

in which C_d is the constant of the model, $\overline{S}_{ij} = (\partial \overline{u}_i/\partial x_j + \partial \overline{u}_j/\partial x_i)/2$ is the resolved strain rate tensor, $|\overline{S}| = \sqrt{2\langle S_{ij}S_{ij}\rangle}$ is its magnitude and $\overline{\Delta} = 2(\Delta x \Delta y \Delta z)^{1/3}$ is the filter width, proportional to the grid size in all directions. Adopting a least squares procedure [56], the constant C_d is evaluated as:

$$C_d^2 = -\frac{1}{2}\frac{\langle L_{ij}M_{ij}\rangle}{\langle M_{mn}M_{mn}\rangle} \tag{3.8}$$

with:

$$M_{ij} = \widehat{\overline{\Delta}}^2 |\widehat{\overline{S}}|\widehat{\overline{S}}_{ij} - \overline{\Delta}^2 \widehat{|\overline{S}|\overline{S}}_{ij} \tag{3.9}$$

and where $\langle\cdot\rangle$ represents an appropriate ensemble or local averaging required to avoid the mathematical inconsistency that one encounters when removing C_d from a filtering operation.
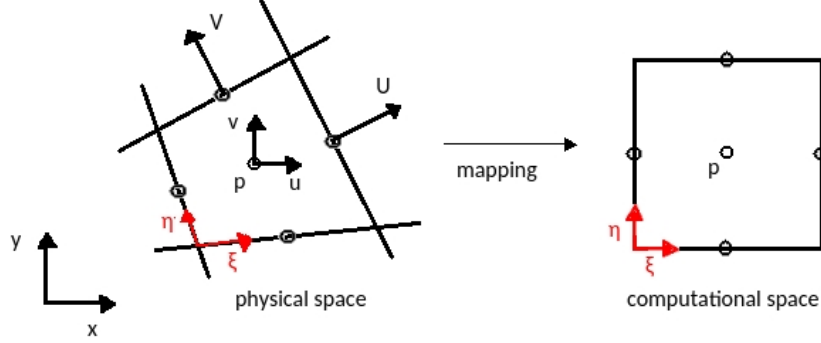
Figure 3.2: Frame of reference transformation from physical to computational space, two dimensional view.

3.1.2   Computational domain

The complex and irregular geometries, typical of the environmental engineering, can not be treated in the Cartesian frame of reference, therefore the governing Equations 3.3 and 3.4 are transformed into a curvilinear form. Velocity gradient in the Cartesian coordinates can be written as:

$$\frac{\partial u_i}{\partial x_j} = \frac{\partial u_i}{\partial \xi_k} \frac{\partial \xi_k}{\partial x_j} \tag{3.10}$$

hence, in the curvilinear coordinate framework the Equations 3.3 and 3.4 become:

$$\frac{\partial U_m}{\partial \xi_m} = 0 \tag{3.11}$$

$$\frac{\partial J^{-1}\overline{u}_i}{\partial t} + \frac{\partial U_m \overline{u}_i}{\partial \xi_m} = -\frac{1}{\rho_0} \frac{\partial}{\partial \xi_m} \left(J^{-1} \frac{\partial \xi_m}{\partial x_i} \overline{p} \right) + \frac{\partial}{\partial \xi_m} \left(\nu G^{mn} \frac{\partial \overline{u}_i}{\partial \xi_n} \right)$$
$$- J^{-1} \frac{\partial \xi_m}{\partial x_j} \frac{\partial \tau_{ij}}{\partial \xi_m} \tag{3.12}$$

where ξ_m are the transformed coordinates (ξ, η, ζ), J^{-1} is inverse of the Jacobian of the coordinate transformation or the cell volume, U_m is volume flux or the contravariant velocity multiplied by the Jacobian, normal to the

surface of constant ξ_m and G^{mn} is mesh skewness tensor. The aforementioned quantities are given by:

$$J^{-1} = \det \frac{\partial x_i}{\partial \xi_j} \tag{3.13}$$

$$U_m = J^{-1} \frac{\partial \xi_m}{\partial x_j} \overline{u}_j \tag{3.14}$$

$$G^{mn} = J^{-1} \frac{\partial \xi_m}{\partial x_j} \frac{\partial \xi_n}{\partial x_j} \tag{3.15}$$

In LES-COAST, the governing equations are solved on a structured non-staggered grid, where the Cartesian velocity components and pressure are defined at the center of the cells and the volume fluxes are defined at the corresponding faces (see Figure 3.2).

3.1.3   Fractional step method

The solution of Equations 3.11 and 3.12 is based on fractional step method (see Zang et al. [101]). Spatial discretization in the computational space is carried out using second order central finite differences, whereas temporal integration is carried out by using the second order accurate Adams Bashforth scheme for the convective term, and implicit Crank-Nicolson scheme for the diagonal viscous terms. A multigrid technique is used for the solution of the pressure equation. The discretised form of the Equations 3.11 and 3.12 reads as:

$$\frac{\delta U_m}{\delta \xi_m} = 0 \tag{3.16}$$

$$J^{-1} \frac{\overline{u}_i^{n+1} - \overline{u}_i^n}{\Delta t} = \frac{3}{2}(C_i^n + D_E(\overline{u}_i^n)) - \frac{1}{2}(C_i^{n-1} + D_E(\overline{u}_i^{n-1}))$$
$$+ R_i(\overline{p}^{n+1}) + \frac{1}{2}(D_I(\overline{u}_i^{n+1} + \overline{u}_i^n)) \tag{3.17}$$

in which $\delta/\delta\xi_m$ defines the discrete finite difference operator in the computational space and the superscripts (such as n) represent the time step. The quantities C_i (convective terms), R_i (the discrete operator for the pressure gradient terms), D_E (discrete operator representing the off-diagonal diffusive

terms, treated explicitly) and D_I (discrete operator representing the diagonal viscous terms, treated implicitly) are expressed as:

$$C_i = -\frac{\delta}{\delta\xi_m}\left(U_m\overline{u}_i\right) \tag{3.18}$$

$$R_i = -\frac{\delta}{\delta\xi_m}\left(J^{-1}\frac{\delta\xi_m}{\delta x_i}\right) \tag{3.19}$$

$$D_I = \frac{\delta}{\delta\xi_m}\left(\nu G^{mn}\frac{\delta}{\delta\xi_n}\right) \qquad m = n \tag{3.20}$$

$$D_E = \frac{\delta}{\delta\xi_m}\left(\nu G^{mn}\frac{\delta}{\delta\xi_n}\right) \qquad m \neq n \tag{3.21}$$

By applying the fractional step method described in Zang et al. [101] to Equation 3.17, the momentum equation is solved for each iteration splitting it into two steps called *predictor* and *corrector*.

In the first step (*predictor*), Equation 3.17 is solved for an unphysical velocity u_i^* which satisfies advective and diffusive transport only:

$$\left(I - \frac{\Delta t}{2J^{-1}}D_I\right)(u_i^* - u_i^n) =$$
$$\frac{\Delta t}{J^{-1}}\left[\frac{3}{2}(C_i^n + D_E(\overline{u}_i^n)) - \frac{1}{2}(C_i^{n-1} + D_E(\overline{u}_i^{n-1})) + D_I(u_i^n)\right] \tag{3.22}$$

where I is the identity matrix. The approximate factorization technique is used to invert the matrix D_I, so the Equation 3.22 becomes:

$$\left(I - \frac{\Delta t}{2J^{-1}}D_1\right)\left(I - \frac{\Delta t}{2J^{-1}}D_2\right)\left(I - \frac{\Delta t}{2J^{-1}}D_3\right)(u_i^* - u_i^n) =$$
$$\frac{\Delta t}{J^{-1}}\left[\frac{3}{2}\left(C_i^n + D_E(\overline{u}_i^n)\right) - \frac{1}{2}\left(C_i^{n-1} + D_E(\overline{u}_i^{n-1})\right) + D_I(u_i^n)\right] \tag{3.23}$$

where:

$$D_k = \frac{\delta}{\delta\xi_k}\left(\nu G^{kk}\frac{\delta}{\delta\xi_k}\right) \qquad k = 1, 2, 3 \tag{3.24}$$

Afterwards, the second step (*corrector*) adjusts the flow-field considering the pressure gradient. It consists in finding out the velocity u_i^{n+1} from the intermediate velocity u_i^* such that the continuity equation is satisfied. From

Equations 3.17 and 3.22, the velocities u_i^{n+1} and u_i^* are related to the pressure gradient by:

$$u_i^{n+1} - u_i^* = \frac{\Delta t}{J^{-1}} \left[R_i(\phi^{n+1}) \right] \tag{3.25}$$

in which the projector operator ϕ satisfies the following relation:

$$R_i(p) = \left(J^{-1} - \frac{\Delta t}{2} D_I \right) \left(\frac{R_i(\phi)}{J^{-1}} \right) \tag{3.26}$$

Once written the Equation 3.25 in the chain-rule-conservation-law form, it can be interpolated on the cell face yielding:

$$U_m^{n+1} = U_m^* - \Delta t \left(G^{mn} \frac{\delta \phi^{n+1}}{\delta \xi_n} \right) \tag{3.27}$$

where $U_m^* = J^{-1}(\delta \xi_m / \delta x_j) u_j^*$ is called the intermediate volume flux.

Replacing Equation 3.27 into Equation 3.16, the Poisson equation for the pressure ϕ^{n+1} is obtained as:

$$\frac{\delta}{\delta \xi_m} \left(G^{mn} \frac{\delta \phi^{n+1}}{\delta \xi_n} \right) = \frac{1}{\Delta t} \frac{\delta U_m^*}{\delta \xi_m} \tag{3.28}$$

The elliptic equation 3.28 is solved using a mixed line/point-SLOR algorithm together with a multigrid method in order to speed up the convergence. In Zang et al. [101], more details about the method are presented.

3.2   OpenFOAM software

OpenFOAM, Open Field Operation and Manipulation [97] is a free, open source computational fluid dynamics (CFD) software. The model is three-dimensional and it is structured with a set of flexible modules written in C++, that are employed to build solvers to simulate specific problems in fluid mechanics and engineering [47]. Pre- and post-processing tasks are accessible to the solvers through utilities as well as libraries to create toolboxes for turbulence models, mesh transformation and combustion. The model is free in its hierarchical design and structure, making the solvers, utilities and libraries entirely extensible. OpenFOAM uses finite volume numerics to solve

systems of partial differential equations on either structured or unstructured meshes. The fundamental equations are developed within a robust, implicit, pressure-velocity, iterative solution framework and computed with a domain decomposition method, in which the geometry and other fields are divided and allocated to separate processors. To solve the conservation equations in a finite volume scheme, the values of the flow variables are required at the face centres. In this work, we use the pisoFOAM solver based on the PISO (Pressure-Implicit Split Operator) algorithm originally proposed by Issa [44] and Issa et al. [45]. The spatial derivatives are discretized using second-order central differences. A standard second order finite volume discretization of a Gaussian integration scheme (Gauss linear) is used for the gradient terms. The implicit, second order backward scheme is applied for the temporal derivatives, whereas the Gauss upwind scheme is adopted for the turbulence model.

3.2.1   The PISO algorithm

The incompressible continuity and momentum equations are given by:

$$\nabla \cdot \mathbf{u} \;=\; 0 \tag{3.29}$$

$$\frac{\partial \mathbf{u}}{\partial t} + \nabla \cdot (\mathbf{u}\mathbf{u}) - \nabla \cdot (\nu \nabla \mathbf{u}) \;=\; -\nabla p \tag{3.30}$$

where the non-linearity in the convection term $(\nabla \cdot (\mathbf{u}\mathbf{u}))$ is handled using an iterative solution technique:

$$\nabla \cdot (\mathbf{u}\mathbf{u}) \approx \nabla \cdot (\mathbf{u}^o \mathbf{u}^n) \tag{3.31}$$

with $\mathbf{u}^o$ the currently available solution and $\mathbf{u}^n$ the new solution. The algorithm cycles until $\mathbf{u}^o = \mathbf{u}^n$. In incompressible flow the coupling between density and pressure is removed, therefore there is no pressure equation. On contrary, the continuity equation imposes a scalar constraint on the momentum equation. The pressure-velocity system contain two complex coupling terms, the non-linear convection term with the $\mathbf{u} - \mathbf{u}$ coupling and the linear pressure-velocity coupling. The idea behind the PISO algorithm is as follows:

- on small time-step, the pressure-velocity coupling is much stronger than the non-linear coupling;

- it is therefore possible to repeat a number of pressure correctors without updating the discretization of the momentum equation (without updating $\mathbf{u}^o$);

- in this set-up, the first pressure corrector will create a conservative velocity field, while the second and the following will establish the pressure distribution.

In order to derive a pressure equation, the momentum equation is discretized, keeping the pressure gradient in its original form (for more details see Jasak [46]):

$$a_P \mathbf{u}_P + \sum_N a_N \mathbf{u}_N = \mathbf{r} - \nabla p \qquad (3.32)$$

where a_N is the matrix coefficient corresponding to the neighbour N, a_P is the coefficient of the computational point P located at the centroid of the control volumes and $\mathbf{r}$ is the source term. Introduce the $\mathbf{H}(\mathbf{u})$ operator:

$$\mathbf{H}(\mathbf{u}) = \mathbf{r} - \sum_N a_N \mathbf{u}_N \qquad (3.33)$$

so that:

$$\mathbf{u}_P = \frac{1}{a_P} \left[\mathbf{H}(\mathbf{u}) - \nabla p \right] \qquad (3.34)$$

Substituting this in the incompressible continuity equation 3.29, a pressure equation for incompressible flow is obtained:

$$\nabla \cdot \left[\frac{\nabla p}{a_P} \right] = \nabla \left[\frac{\mathbf{H}(\mathbf{u})}{a_P} \right] \qquad (3.35)$$

The discretised form of the continuity equation 3.29 is:

$$\nabla \cdot \mathbf{u} = \sum_f \mathbf{s}_f \mathbf{u} = \sum_f F \qquad (3.36)$$

where F is the face flux that is calculated, substituting the expression of the velocity 3.34, as:

$$F = -\frac{\mathbf{s}_f \cdot \nabla p}{a_P} + \frac{\mathbf{s}_f \cdot \mathbf{H}(\mathbf{u})}{a_P} \qquad (3.37)$$

When the Equation 3.35 is satisfied, the face fluxes are guaranteed to be conservative. Summarizing, the PISO loop consists of an implicit momentum predictor followed by a series of pressure solutions and explicit velocity corrections. The loop is repeated until a pre-determined tolerance is reached [46].

3.2.2 Detached-eddy simulation

Detached-eddy simulation is a nonzonal technique that resolves time-dependent, 3D turbulent motions (as in LES) and applicable to high Reynolds numbers (as the RANS methods).

The Spalart-Allmaras (SA) model [86] is used as the base model. The one equation SA model solves a transport equation for the modified eddy viscosity, $\tilde{\upsilon}$. The DES version of SA is obtained by replacing the turbulence length scale d (distance to the nearest wall) in the destruction term of the transport equation for $\tilde{\upsilon}$ with a new length scale $\tilde{d} = min(d, C_{DES}\Delta)$, where Δ is the local grid size and the model parameter C_{DES} is equal to 0.65 [81, 25]. Close to solid boundaries, DES reduces to RANS [52] ensuring an accurate solution of the near-wall flow. In the case of rough wall, the roughness effects are taken into account by redefining the distance to the boundary as $d = d_{min} + 0.03k_s$ [85], with d_{min} the distance to the closest boundary and k_s the equivalent roughness height. Away from the solid boundaries, the closure is a one-equation model for the modified SGS eddy viscosity [26]:

$$\frac{\partial \tilde{\upsilon}}{\partial t} + u_j \frac{\partial \tilde{\upsilon}}{\partial x_j} = C_{b1}[1 - f_{t2}]\tilde{S}\tilde{\upsilon} + \frac{1}{\sigma}\{\nabla \cdot [(\upsilon + \tilde{\upsilon})\nabla\tilde{\upsilon}] + C_{b2}|\nabla\tilde{\upsilon}|^2\}$$
$$- \left[C_{w1}f_w - \frac{C_{b1}}{\kappa^2}f_{t2}\right]\left[\frac{\tilde{\upsilon}}{\tilde{d}}\right]^2 \quad (3.38)$$

The turbulent eddy viscosity is given by:

$$\nu_T = \tilde{\upsilon}f_{v1} \qquad\qquad f_{v1} = \frac{\chi^3}{\chi^3 + C_{v1}^3} \qquad\qquad \chi = \frac{\tilde{\upsilon}}{\upsilon} \qquad (3.39)$$

where υ is the molecular viscosity. The production term is expresses as:

$$\tilde{S} = S + \frac{\tilde{\upsilon}}{k^2\tilde{d}^2}f_{v2} \qquad\qquad f_{v2} = 1 - \frac{\chi}{1 + \chi f_{v1}} \qquad (3.40)$$

with S the magnitude of the vorticity. The function f_w is given by:

$$f_w = g \left[\frac{1 + C_{w3}^6}{g^6 + C_{w3}^6} \right]^{1/6} \qquad g = r + C_{w2}(r^6 - r) \qquad r = \frac{\tilde{v}}{\tilde{S}k^2\tilde{d}^2} \qquad (3.41)$$

The function f_{t2} is defined as:

$$f_{t2} = C_{t3}exp(-C_{t4}\chi^2) \qquad (3.42)$$

The wall boundary condition is $\tilde{v} = 0$ and the constants are:

$$C_{v1} = 7.1 \quad C_{t3} = 1.1 \quad C_{t4} = 2.0 \quad C_{b1} = 0.1355 \quad C_{b2} = 0.622$$

$$\sigma = 2/3 \quad k = 0.41 \quad C_{w2} = 0.3 \quad C_{w3} = 2.0 \qquad C_{w1} = \frac{C_{b1}}{k^2} + \frac{(1 + C_{b2})}{\sigma}$$

When the production and destruction terms of the model are balanced, the turbulence length scale $\tilde{d} = C_{DES}\Delta$ becomes proportional to the local grid size and yields an eddy viscosity proportional to the mean rate of strain and Δ^2, as in LES with a dynamic Smagorisky model. Indeed, the role of Δ is to allow the energy cascade down to the grid size similar to the classical LES.

Chapter 4

Description of simulation cases

The laboratory data of Blanckaert [6, 9] are used for validation purposes. The channel consists of a straight inflow reach of $4\,m$, a curved reach of $193°$ and a straight outflow reach of $3.5\,m$, all with a flat bed, representative of the early phase of bed erosion (see Figure 4.1).
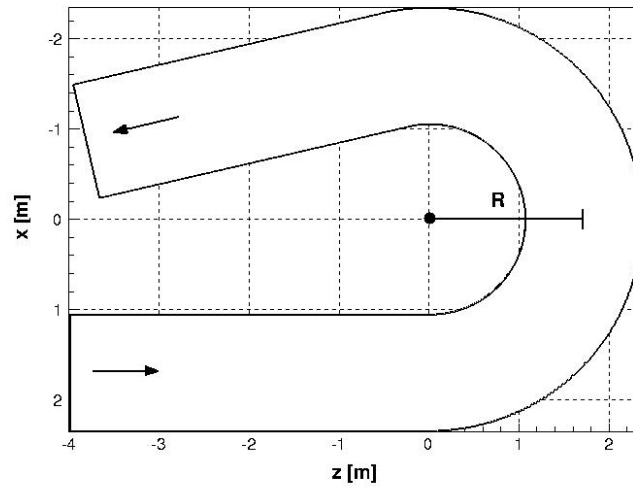
Figure 4.1: Sketch of flow geometry. The arrows denote the flow direction.

The radius of curvature at the center line of the channel is $R = 1.7\,m$. The channel has a rectangular cross-section, with width $B = 1.3\,m$ and average water depth $H = 0.159\,m$ (run n°1). The vertical sidewalls of the laboratory channel are rigid and hydraulically smooth, whereas the channel bed is hydraulically rough. In the experiment the bed was covered with quasi uniform sand ($d_{50} = 0.002\,m$). In the present thesis, an additional curved channel is considered, with $H = 0.141\,m$ (run n°2). The flow rate Q is the same for the two simulations and equals to $89\,l/s$. According to van Rijn [95], the Nikuradse equivalent roughness can be assumed as three times the sand diameter ($k_s = 0.006\,m$); the two Reynolds numbers are such that $Re \gg 4000$. The flow in the two simulations is fully rough turbulent ($Re_* > 70$) and sub-critical ($F_r < 1$). Moreover, to account for the influence of the super-elevation of the free surface on the flow field characteristics, the test case run n°1 is also conducted reproducing the steady water surface detected by Blanckaert [9] in its experiment (see Figure 4.2). This last test is presented in the Chapter 9 and it is indicated as run n°1FS.

The hydraulic and geometric conditions are summarized in Table 4.1.
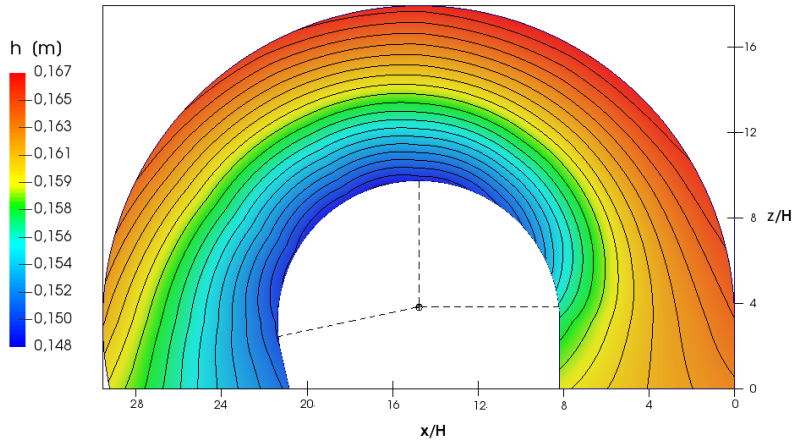
Figure 4.2: Water surface level with an interval of $0.001\,m$, reconstructed through Blanckaert experimental data [9].

| Run | Q | B | H | W_{av} | Re | F_r | k_s | R | R/H | B/H |
n°	(m^3/s)	(m)	(m)	(m/s)	(-)	(-)	(m)	(m)	(-)	(-)
1	0.089	1.3	0.159	0.43	68400	0.34	0.006	1.7	10.7	8.2
2	0.089	1.3	0.141	0.49	68000	0.41	0.006	1.7	12	9.2

Table 4.1: Hydraulic conditions for the two numerical simulations. Q denotes the discharge, B the width of the flume, H the water depth, W_{av} the bulk velocity, Re the Reynolds number, F_r the Froude number, k_s the Nikuradse equivalent roughness and R the radius at the center line. Re and F_r are based on the bulk velocity W_{av} and the water depth H.

4.1   Simulations setup

The inflow conditions are provided by the output of simulations carried out by considering the corresponding straight open-channel flows with periodic boundaries in streamwise direction. A convective boundary condition is instead used at the outflow. Since the Reynolds number is too large for solving directly the near wall viscous sub-layer, a wall-layer approach is employed in the LESs. For the vertical lateral walls, the standard smooth law of the wall is used in the logarithmic layer:

$$v_n^+ = 2.5 \ln z_n^+ + 5.5 \tag{4.1}$$

where v_n^+ is the wall-normal velocity dimensionless with the average shear velocity u_τ and z_n^+ represent the wall-normal coordinate expressed in wall units (ν/u_τ). A numerical validation of the wall layer model implemented in the LES-COAST code is reported in the Appendix A. For the channel bed a modified log law (see, e.g., [96]) is used:

$$v_n^+ = 2.5 \ln \frac{z_n}{k_s} + 8.5 \tag{4.2}$$

where k_s is the roughness height (see Table 4.1).
The free surface in run n°1 and n°2, is treated as a horizontal, impermeable rigid lid where the free-slip condition is applied, namely the normal

gradient of the velocities parallel to the surface and the wall-normal velocity component are set to be zero [52, 92]:

$$\frac{\partial w}{\partial y} = 0, \quad \frac{\partial u}{\partial y} = 0, \quad v = 0 \qquad (4.3)$$

The use of this condition is justified by the low Froude number of the flows ($F_{r1} = 0.34$ and $F_{r2} = 0.41$), such that the free surface deformation is practically negligible. Instead in run n°1FS, the free surface is not horizontal but inclined as in Figure 4.2.

The simulations are performed on a very high resolution grids consisting of 9 million cells ($128 \times 64 \times 1024$ points in spanwise, vertical and streamwise directions), with a uniform discretization in all three directions. The equations were integrated in time until a statistical steady state was reached. After that, data for the statistics were collected for a sampling time of $\Delta t = 230\,s$ in all simulations, corresponding to 620 time unit ($\Delta t \cdot U/H$) for run n°1, n°1FS and 800 time unit for run n°2. Note that $5\,s$ of real time requires $24\,h$ of computational time running at the supercomputing facility of Italian computing center CINECA, employing 16 processors with the LES-COAST code and 64 processors with the OpenFOAM software.

In the following, all variables are presented in non-dimensional form, using H and U as the length scale and velocity scale, respectively.

Chapter 5

Main flow characteristics

In this section, the primary flow characteristics for the test cases run n°1 and run n°2 are discussed. In particular, we highlight the role of the water depth on the main flow features and the computation results of run n°1 are compared with Blanckaert experimental results [6, 9] in order to validate the numerical model here applied. In the figures the arrows denote the flow direction.

5.1   Mean velocity field

The contours of streamwise velocities at the free surface are shown for run n°1 and run n°2 in Figures 5.1(a) and 5.1(b), respectively. The figures show how turbulent channel flow enters the bend and how this flow is subjected to centripetal forces in the curved part of the bend, giving rise to secondary flow cells. This mechanism is evidenced by the presence of higher streamwise velocity near the inner bank of the channel, at the entry of the bend, and by a clear outward shift of momentum. Moving forward, the main flow detaches from the inner bank because of the formation of an internal shear layer. The comparison of the two figures shows the importance of the aspect ratio (the ratio between the channel width B and the water depth H) on these main features of the flow, whose strength increase when the ratio B/H decreases

26
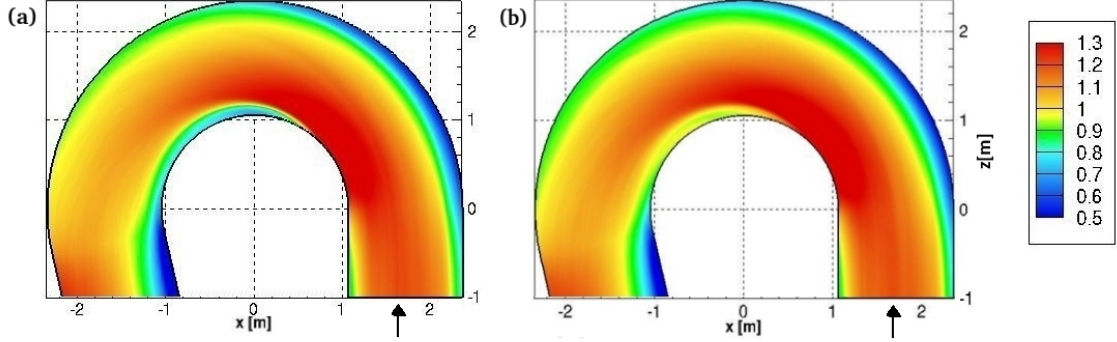
Figure 5.1: Streamwise velocities at free surface, scaled with the bulk velocity W_{av}: (a) run n°1 ($B/H = 8.2$) and (b) run n°2 ($B/H = 9.2$).

(see Table 4.1). The generation of the flow separation is mainly due to the sharpness of the bend R/B (see [2]). In the case of mildly curved bends, no separation or development of an internal shear layer takes place. In sharp bends characterized by values of $R/B < 3$, the flow begins to separate near the convex inner bank, also if in this zone it is still rather stagnant. When the sharpness of the bend is relatively small ($R/B < 2$), vortex energy sinks and flow reversal begin to form in the flow. The present results clearly show the convex bank flow separation also identified by van Balen et al. [92] and Koken et al. [52]. Its generation is strongly related to turbulence: the boundary separation develops when the turbulent flow moves rapidly into a region with adverse pressure gradient. Flow separation implies the failure of the RANS with isotropic turbulence models to reproduce correctly the flow in sharp bends [92, 102].

In the plan of view of velocity vectors depicted in Figure 5.2, the blue coloured vectors show the near-bed velocity components and the red coloured vectors show the near-free surface velocity components. We can observe a shifting of the high-velocity core from the inner bank to the outer bank. At the bend apex, the near-bed flow is oriented towards the inner bank,
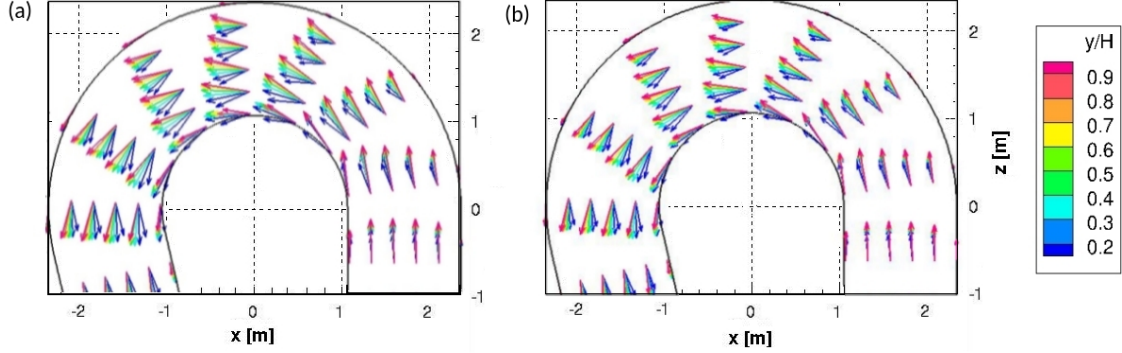
Figure 5.2: Plan view of velocity vectors: (a) run n°1 ($B/H = 8.2$) and (b) run n°2 ($B/H = 9.2$). Colors in the vectors define the vector elevation.

while the near free-surface flow is oriented towards the outer bank. This hydrodynamic structure indicates the presence of the helicoidal recirculation typical of meandering channels [100]. In Figure 5.2 the near-bed and near-free surface vectors start to deviate from each other around the 30° cross-section and the highest angular deviation is observed at the 90° cross-section. A comparison between Figures 5.2(a) and 5.2(b) shows that the angular shifting and, thus, the associated helicoidal recirculation, are less pronounced in case of shallower conditions.

For a more quantitative investigation of the flow field, the vertical profiles of the streamwise velocities and transverse velocities are highlighted in Figures 5.3 and 5.4, respectively. The profiles are located at 60°, 120° and 180° cross sections in the bend and they are given in the transverse direction for six different locations of the verticals: $0.2\,B$; $0.35\,B$; $0.5\,B$; $0.65\,B$ and $0.8\,B$ (from inner to outer bank). In Figures 5.3 and 5.4, the predicted vertical profiles (solid lines) are compared with the measurements (circle) for the run n°1. The streamwise and transverse vertical profiles of velocities are influenced by the along bend evolution of the cross stream circulation zone and the streamwise vorticity [10, 15, 102]. The streamwise velocity profiles undergo a flattening due to the advective momentum transport by
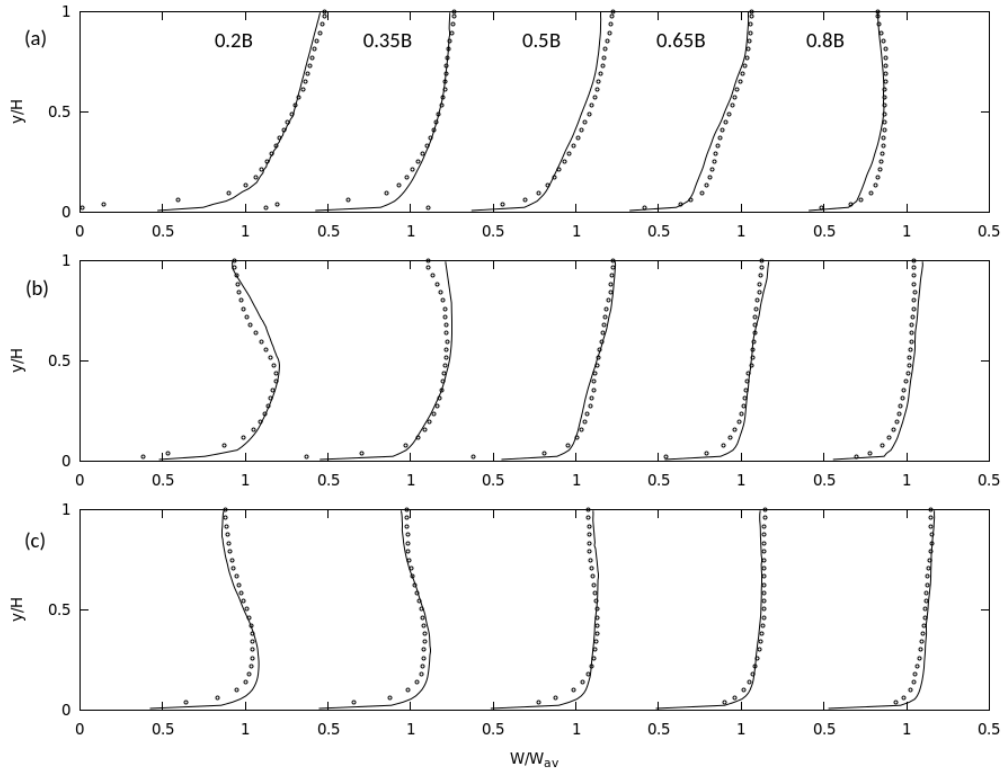
Figure 5.3: Streamwise velocities at three cross sections in the flow field: (a) 60°, (b) 120° and (c) 180° cross section. The circles represent the experimental results of Blanckaert [9] while the solid lines are the predicted results of run n°1. The values are made non-dimensional by the bulk velocity W_{av}.

the secondary flow, consequently decreasing the driving force of the cross-stream circulation. Figure 5.3 shows that the streamwise velocity profiles are about logarithmic in the upstream part of the bend and flatten when moving toward the inner bank. On the other hand, downstream of the 90° cross section, the streamwise profiles located in the inner half of the bend, are non monotonic with maximum velocities in the lower part of the water column. Furthermore, we can note an inflexion point in the velocity profiles that coincides with the zone of steepest gradient where the internal shear layer characterized by eddies and vortices occurs.
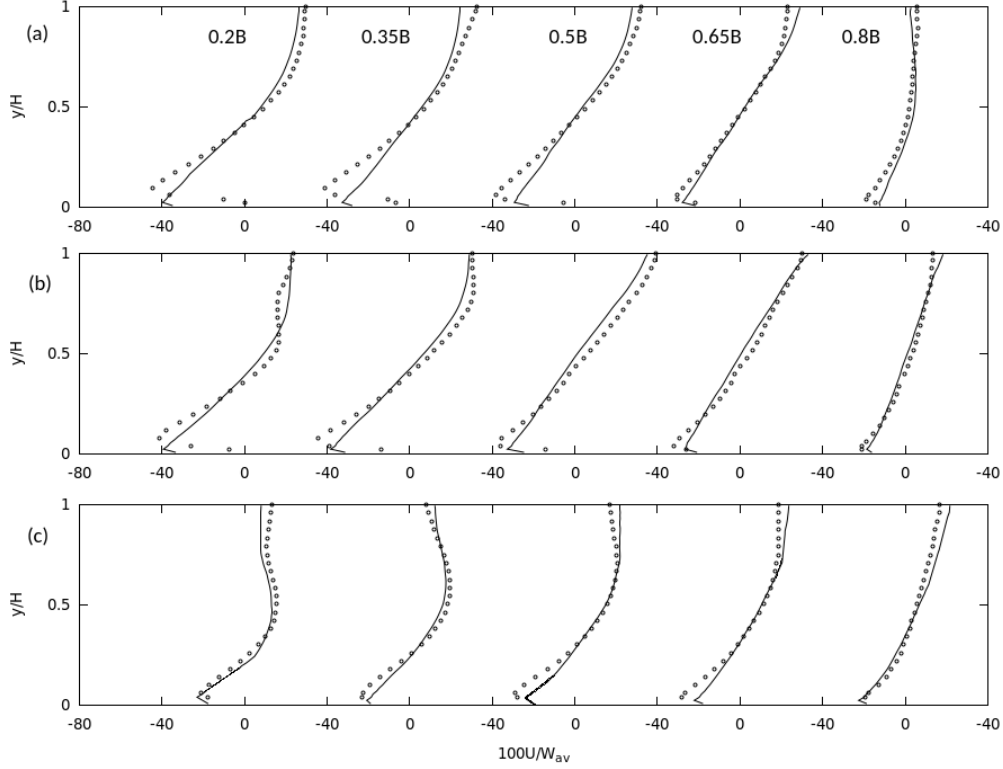
Figure 5.4: Transverse velocities at three cross sections in the flow field: (a) 60°, (b) 120° and (c) 180° cross section. The circles represent the experimental results of Blanckaert [9] while the solid lines are the predicted results of run n°1. The values are made non-dimensional by the bulk velocity W_{av}.

The transverse velocity profiles, represented in Figure 5.4, reveal the principal characteristics of the curvature induced cross-stream circulation cell. The latter occupies the large part of the cross section, within which fluid particles follow a helicoidally path with inward (i.e., negative) transverse velocities in the lower part and outward (i.e., positive) transverse velocities in the upper part.

The comparison between measured and predicted vertical profiles of streamwise and transverse velocities reveals minimal differences. The major discrepancies are visible close to the water surface near the outer bank, where the

streamwise predicted velocity profiles do not show the decrease of the measured velocity towards the water surface. The disagreements near the water surface might be due to the rigid-lid assumption for the free surface but also to the reduced accuracy of the measurements in this zone.

5.2 Vertical vorticity

In Figure 5.5, we show the vertical vorticity ω_y at the free surface resulting from the two simulations. The spatial distribution of the vorticity reveals the rotational structure at the free surface and clearly show the detachment of the boundary shear layer at the inner bank. It clearly appears that the detachment of this shear layer is shifted downstream in the channel bend and that the peak values of the vorticity are somewhat lower in the case of run n°2 (Figure 5.5(b)). The influence of the internal shear layer increases in strength with increasing water depth ($B/H = 8.2$) and in a real river context, it is relevant for bank accretion, river planimetry and meander formation.
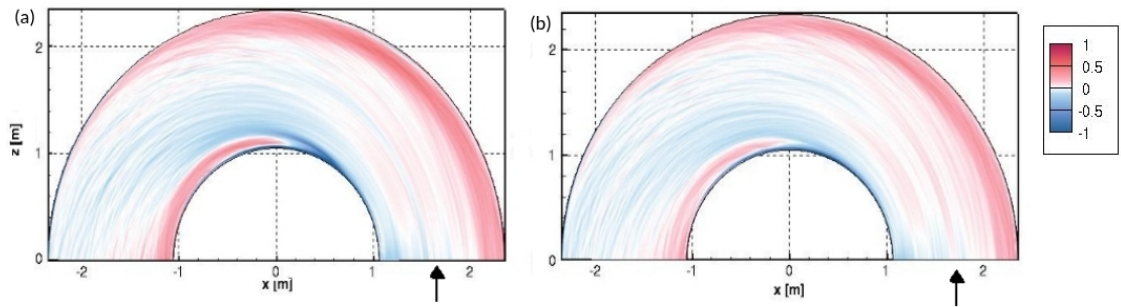
Figure 5.5: Vertical vorticity, scaled with the bulk velocity W_{av} and the mean water depth H: (a) run n°1 ($B/H = 8.2$) and (b) run n°2 ($B/H = 9.2$).

Chapter 6

Secondary flow features

Secondary flow is a key element of the hydrodynamic of meandering channels and its correct prediction is fundamental as regards, for example, the outer banks erosion and inner bank accretion and, hence, planimetry evolution.

In the following, in order to render the flow pattern along the bend, the results are shown at six cross sections located in the curved part of the channel at 30°, 60°, 90°, 120°, 150° and 180°, respectively.

6.1 Streamwise vorticity

When the turbulent channel flow enters the bend, it is subject to centrifugal forces in the curved part of the geometry, giving rise to secondary flow cells. In Figure 6.1 we illustrate the patterns of streamwise vorticity for the two runs. It highlights the rotational strength of the secondary flow. Near the inner bank, a flow reversal occurs and a recirculating vortex develops in the separation zone. The formation of an internal shear layer is identified by the existence of a belt of positive vorticity values at the free surface. We notice that the detachment of this shear layer is shifted more downstream when increasing the width to depth ratio (Figure 6.1(b)) and that the peak values of the vorticity are somewhat lower. The principal coherent structure

related to secondary flow is the main cross-stream circulation cell, that tends
to cover a large part of the channel bend cross sections when the bed is not
deformed [9] or weakly deformable [7]. Such circulation cell is represented
in the central region of the section in Figure 6.1, filling the major area of
negative vorticity. Furthermore, we can observe the generation of an outer-
bank cell, corresponding to an area of positive vorticity near the outer bank
close to the free surface. It is the strongest in the upstream part of the bend,
whereas it loses strength in the downstream part of the bend. It is evident
as the outer bank cell strength increases with decreasing the aspect ratio
(Figure 6.1(a)). This secondary counter-rotating cell of cross-stream circula-
tion has been also observed in natural channels [3, 4, 32, 91] and identified
in previous studies of mildly and sharp channel bends [8, 11, 75]. It affects
the bank stability and for this reason the effects of the secondary flow are
incorporated in the prediction of bank erosion models [71].

Figure 6.1: Streamwise vorticity at 30°, 60°, 90°, 120°, 150° and 180° cross
sections: (a) run n°1 ($B/H = 8.2$) and (b) run n°2 ($B/H = 9.2$). The values
are made non-dimensional using the mean water H and the bulk velocity
W_{av}.

6.2 Vertical velocity

Figure 6.2 shows the contour of the vertical velocity for run n°1 and run n°2. It reveals the complex structure of the secondary flow. Near the inner bank an alternating pattern of up-welling and down-welling is observed. This pattern is associated with the internal shear layer separating from the inner bank. The flow near the outer bank is obviously dominated by down-welling associated with the main secondary flow motion due to the presence of the centripetal forces. The spatial distribution of the vertical velocities is almost the same for the two test cases, with an evident greater intensity for run n°1 (see Figure 6.2(a)).
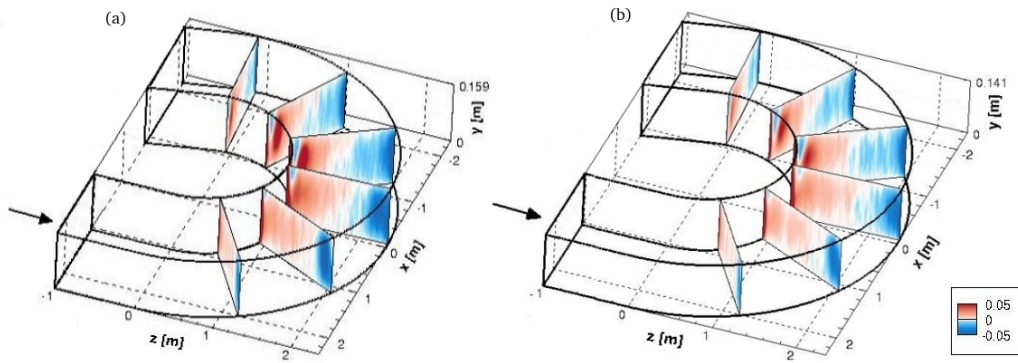
Figure 6.2: Vertical velocity at 30°, 60°, 90°, 120°, 150° and 180° cross sections: (a) run n°1 and (b) run n°2. The values are made non-dimensional using the bulk velocity W_{av}.

Chapter 7

Turbulence structures

In the context of the meandering spatial evolution, the knowledge of the mean flow hydrodynamics is not sufficient and also the turbulent flow structure is important. This section analyses the turbulence parameters in sharp meandering bends, emphasizing the influence of the water depth. Hereafter the symbol $\langle \cdot \rangle$ denotes a quantity averaged in time.

7.1   Turbulence stresses

Figure 7.1 illustrates the along bend distribution of the turbulent shear stresses computed in run n°1 at six cross-sections located in the curved part of the channel at 30°, 60°, 90°, 120°, 150° and 180°, respectively. The behaviour of the transverse-vertical $\langle u_s' v' \rangle$ stress is shown in Figure 7.1(a) and it is strongly related to the secondary flow. The $\langle u_s' v' \rangle$ negative values are dominant in the bend, although a core of positive values is localized near the inner bank in correspondence of the internal shear layer.

In Figure 7.1(b), the streamwise-vertical stress $\langle v' w_s' \rangle$ exhibits an area of negative values in the first part of the bend, that fully coincides with the outer bank circulation cell [14, 93]. In the second part of the bend, the $\langle v' w_s' \rangle$ values become dominant in the upper part of the water column and in particular near the inner bank, where the internal shear layer develops. Conversely, the
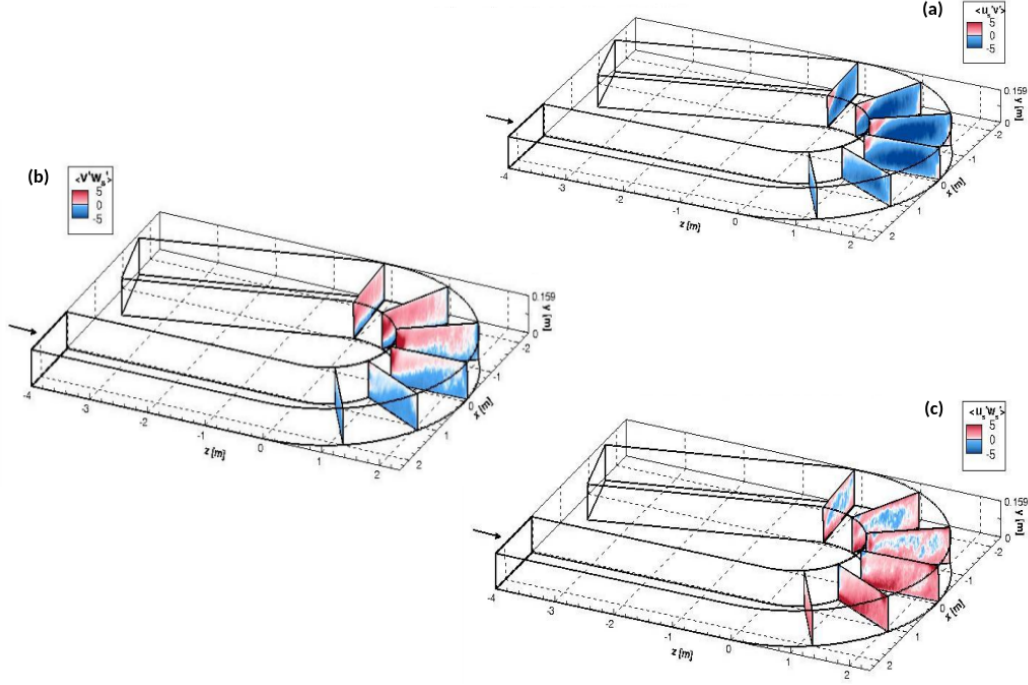
Figure 7.1: Reynolds stresses for run n°1 at 30°, 60°, 90°, 120°, 150° and 180° cross sections: (a) transverse-vertical stresses, (b) streamwise-vertical stresses and (c) streamwise-transverse stresses. The values ($\times 10^3$) are made non-dimensional by the bulk velocity squared W_{av}^2.

$\langle v' w_s' \rangle$ negative values are concentrated in the near-bed region.

The along bend distribution of the streamwise-transverse stress $\langle u_s' w_s' \rangle$ is represented in Figure 7.1(c). In the first half of the bend, it presents a core of high positive values and a strong local increase near the free surface where the outer bank cell and the center region cell touch. This behaviour does not appear for the streamwise-vertical $\langle v' w_s' \rangle$ and transverse-vertical $\langle u_s' v' \rangle$ stresses, since at the free surface the vertical velocity is set to be zero. In the second half of the bend, the patterns of $\langle u_s' w_s' \rangle$ present a less pronounced core of negative values, that tends to increase in the downstream part.

The distribution of Reynolds stresses in run n°2 are reported in Figure
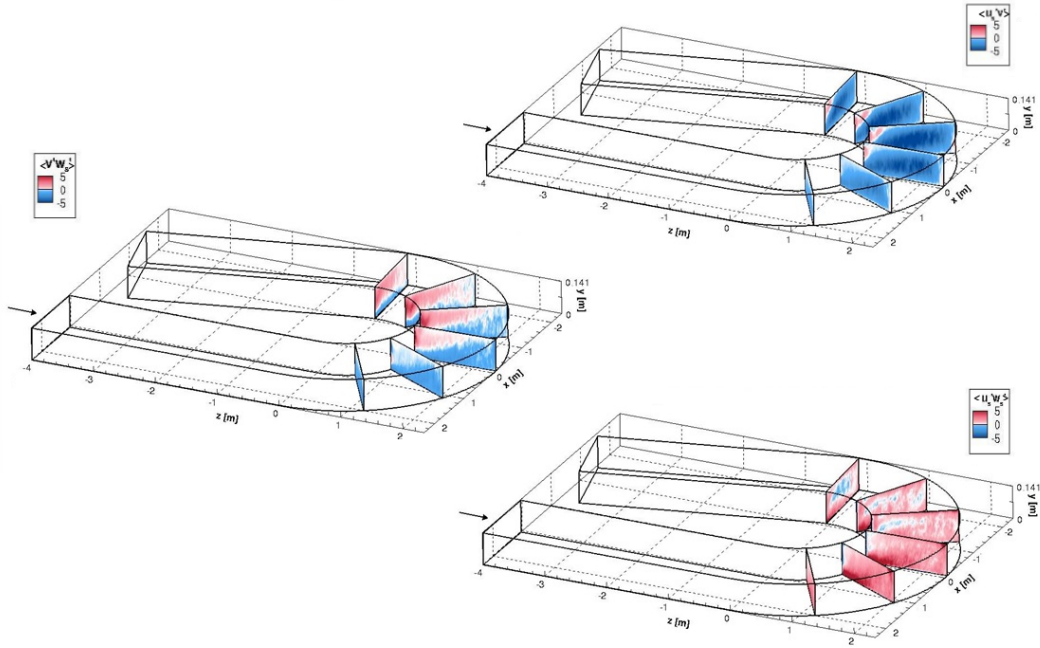
Figure 7.2: Reynolds stresses for run n°2 at 30°, 60°, 90°, 120°, 150° and 180° cross sections: (a) transverse-vertical stresses, (b) streamwise-vertical stresses and (c) streamwise-transverse stresses. The values ($\times 10^3$) are made non-dimensional by the bulk velocity squared W_{av}^2.

7.2. The results show a distribution nearly similar to that of run n°1; they differ only in the intensity of stresses, that is smaller. To summarize, the variation in Reynolds stresses along the channel length highlights the influence of channel geometry on the distribution and magnitude of these stresses. Also, the variation of the water depth in the range herein considered does not affect the Reynolds stress distribution along the channel.

7.1.1 Reliability of eddy-viscosity RANS-like modelling

RANS simulations of sharp meander bend were carried out in Zeng et al. [102] and van Balen et al. [92] using a k - ω and k - ε turbulence model, respectively. These works show the limitation of RANS isotropic models
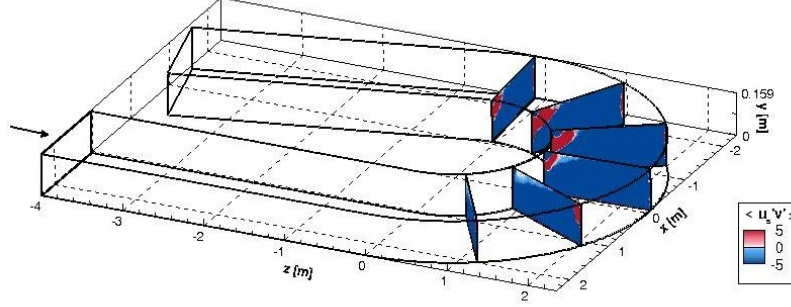
Figure 7.3: Reynolds transverse-vertical stresses for run n°1 at 30°, 60°, 90°, 120°, 150° and 180° cross sections using the RANS-like modelling. The values ($\times 10^3$) are made non-dimensional by the bulk velocity squared W_{av}^2.

to predict the correct hydrodynamics in this type of channel. It is thus important to asses why the assumptions that lie behind the RANS approach closed with eddy-viscosity turbulence models perform poorly for this type of flow fields [20]. Indeed, the eddy-viscosity hypothesis [73] implies the alignment between the elements of the deviatoric Reynolds stress tensor and the rate-of-strain tensor of the mean field:

$$\langle u_i^{'} u_j^{'} \rangle - \frac{2}{3} k \delta_{ij} = -\nu_T \left(\frac{\partial U_i}{\partial x_j} + \frac{\partial U_j}{\partial x_i} \right) \tag{7.1}$$

where δ_{ij} is the Kronecker Delta and ν_T is the eddy-viscosity.

The eddy-viscosity assumption is here verified for run n°1, by computing the off-diagonal Reynolds stress $\langle u_s^{'} v^{'} \rangle$ with Equation 7.1. In the previous section, it was shown that this stress component reflects the secondary flow trend and, therefore, its accurate estimation is very important. By comparing Figures 7.1(a) and 7.3, it is clear that an isotropic eddy viscosity approach correctly predicts the sign of the Reynolds stress, but over-predicts the actual numerical value by about an order of magnitude. This is an evident prove of the inadequacy of RANS models to study sharp meandering rivers. Similar conclusions were drawn by Bressan et al. [20], in the analysis of turbulence around an abutment.
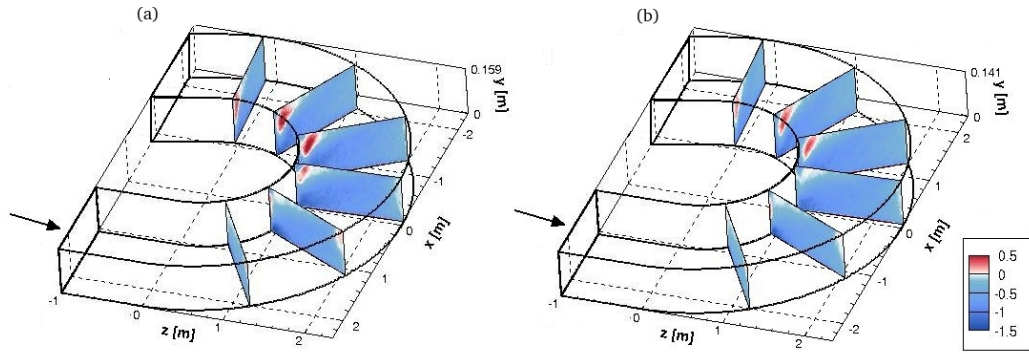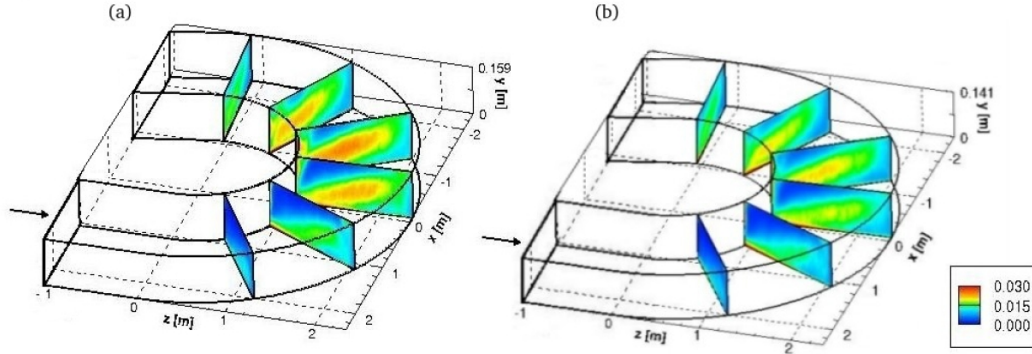
Figure 7.4: Tke at 30°, 60°, 90°, 120°, 150° and 180° cross sections: (a) run n°1 ($B/H = 8.2$) and (b) run n°2 ($B/H = 9.2$). The values are made non-dimensional by the bulk velocity squared W_{av}^2.

7.2   Turbulent kinetic energy

Figure 7.4 shows the spatial distribution of the turbulent kinetic energy (tke), defined as:

$$tke = \frac{1}{2}\langle u^{'}u^{'}\rangle + \frac{1}{2}\langle v^{'}v^{'}\rangle + \frac{1}{2}\langle w^{'}w^{'}\rangle \tag{7.2}$$

In the case of non-erodible bend, as treated here, the flow entering the bend is subject to a "free vortex effect", accelerating at the inner bank relative to the outer bank and producing large scale fluctuations in the flow field. As a result, an eruption of tke occurs in the upstream part of the bend. The production of tke is strongly related to the recirculation cell generated by the local curvature. The tke progressively increases moving towards the core of the center region cell, with maximum values just below the middle flow depth. In the downstream part of the bend, this core of high tke weakens and is reduced to about half of its maximum value at the bend exit. The plots also reflect an outward shift of high momentum fluid due to differential advection; in particular it can be seen that the location of the peak value of tke has shifted towards the outer bank at the 150° cross-section as compared to the 60° cross-section. The analysis clearly shows the increase of turbulent

activity when decreasing the width to depth ratio (see Figure 7.4(a)).

7.3   Turbulence anisotropy

For the investigation of the turbulence anisotropy and the efficiency in turbulence shear stress production, the principal stresses and the so-called structure parameter a_1 are examined.

The Reynolds shear stresses can be used for understanding the force field active in each cross-section of the bend and the forces that act on the solid walls. The difference between the principal stresses $\sigma_1 - \sigma_2$ is an indicator of anisotropy in the two-dimensional cross-sectional plane. Recalling the Mohr's circle [93, 92], it results:

$$\sigma_1 - \sigma_2 = 2 \cdot \sqrt{\left(\frac{\langle u'^2 \rangle - \langle v'^2 \rangle}{2}\right)^2 + \langle u'v' \rangle^2} \tag{7.3}$$

The vertical velocity fluctuations tend to zero at the free surface, as a consequence of the free slip condition, and this circumstance causes the transverse velocity fluctuations to be dominant there. Instead, at the outer bank, the vertical velocity fluctuations tend to prevail. Therefore, the anisotropy results most pronounced at the boundaries, as highlighted in Figure 7.5. The pattern of the principal stresses difference $\sigma_1 - \sigma_2$, in the 60° cross-section shows a strong increase of turbulence activity where the main cross-stream circulation cell and the outer bank cell encroach near the free surface, in particular for the run n°1 (Figure 7.5(a)). In the second half of the bend, the turbulence anisotropy is very high near the inner bank where is located the generation of the internal shear layer, whose influence is less marked in the case of run n°2 (Figure 7.5(b)).

The structure parameter a_1 is defined as the ratio of the magnitude of the turbulent shear stresses and twice the amount of the turbulent kinetic energy:

$$a_1 = \frac{\sqrt{\langle w'v' \rangle^2 + \langle u'v' \rangle^2}}{2k} \tag{7.4}$$
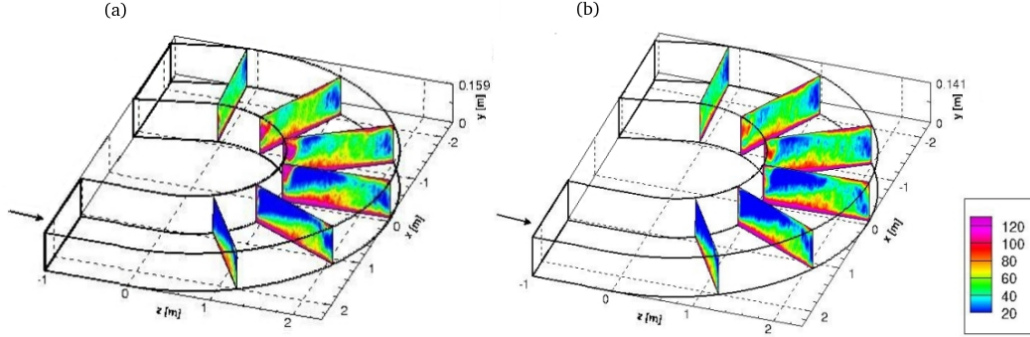
Figure 7.5: Principal stresses difference for run n°1 at 30°, 60°, 90°, 120°, 150° and 180° cross sections. The values ($\times 10^4$) are made non-dimensional by the bulk velocity squared W_{av}^2.

According to Schwarz and Bradshaw [76], it roughly indicates the efficiency of turbulent eddies in producing turbulence shear stresses. Blanckaert and de Vriend [12] report the trend of this non-dimensional parameter a_1 for the case of a straight open-channel flow. It has a value of 0.10 at the bed, a maximum of about 0.14 around the mid-depth and it is zero at the free surface. The structure parameter a_1 is shown in Figure 7.6 for the two test cases. In this figure, we observe relatively low values of the structure parameter a_1 along the interface of the two counter-rotating cells at the free surface (see 60° cross-section). Moreover, this decrease of a_1 is accompanied by a strong increase of the streamwise-transverse stresses $\langle u_s' w_s' \rangle$ and a relatively decrease of the transverse-vertical $\langle u_s' v' \rangle$ and streamwise-vertical $\langle v' w_s' \rangle$ stresses (see Figure 7.1). This dependency is the opposite in the core of the outer bank cell. Therefore, it is possible to deduce that the outer bank cell itself determines a local increase in the production of turbulent shear stress in the cross-sectional plane. In the central region of the bend, the a_1 values have a very similar trend as that of the straight open-channel flow. Instead, near the inner bank we can observe a local decrease of a_1 values along the region of flow separation due to the presence of the internal shear layer.
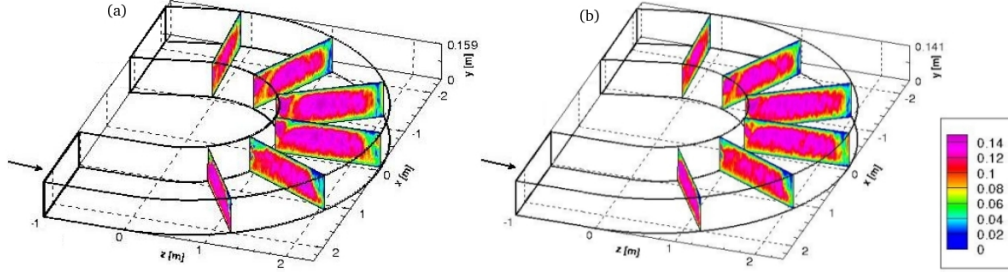
Figure 7.6: Structure parameter at 30°, 60°, 90°, 120°, 150° and 180° cross sections: (a) run n°1 and (b) run n°2. The values are made non-dimensional by the bulk velocity squared W_{av}^2.

7.4   Lumley triangle

The global anisotropy of the Reynolds stress tensor can be further examined using the Lumley triangle. The triangle can be drawn by considering the invariants of the normalized anisotropy tensor, which is computed by subtracting its trace from the Reynolds tensor:

$$b_{ij} = \frac{\langle u_i' u_j' \rangle}{\langle u_k' u_k' \rangle} - \frac{1}{3}\delta_{ij} \tag{7.5}$$

Since the trace of this tensor **b** is zero, it is characterized by only two invariants, II and III, which identify the state of turbulence [60]. It has been shown that any turbulent states must be contained inside a well-defined triangle in the plane, $\xi = (1/2III)^{1/3}$, $\eta = (-1/3II)^{1/2}$. The top curved line (Figure 7.7) corresponds to a two-component turbulent state; the straight line in the $\xi < 0$ half-plane represents a three-component turbulent state, in which one component is smaller than the others (disk-like turbulence); the straight line in the $\xi > 0$ half-plane represents a three-component turbulence, in which one component is larger than the others (rod-like turbulence) [83].

The values of the II and III invariants are evaluated for run n°1 at four different cross-sections: a cross-section at $2\,m$ upstream of the bend entrance, a

cross-section at 60° in the bend, a cross-section at 150° and a cross-section at $2\,m$ beyond the bend exit, where the flow is recovering from centripetal effects and returns to be a straight flow again. The Lumley triangles for these four cross-sections are shown in Figure 7.7. It is known for a straight boundary layer flow that the invariants values are found near the right straight side of the triangle, which represents axisymmetric turbulence with one large eigen-value. This type of behaviour is recognized in the picture of the cross-section $2\,m$ upstream of the bend (Figure 7.7(a)).
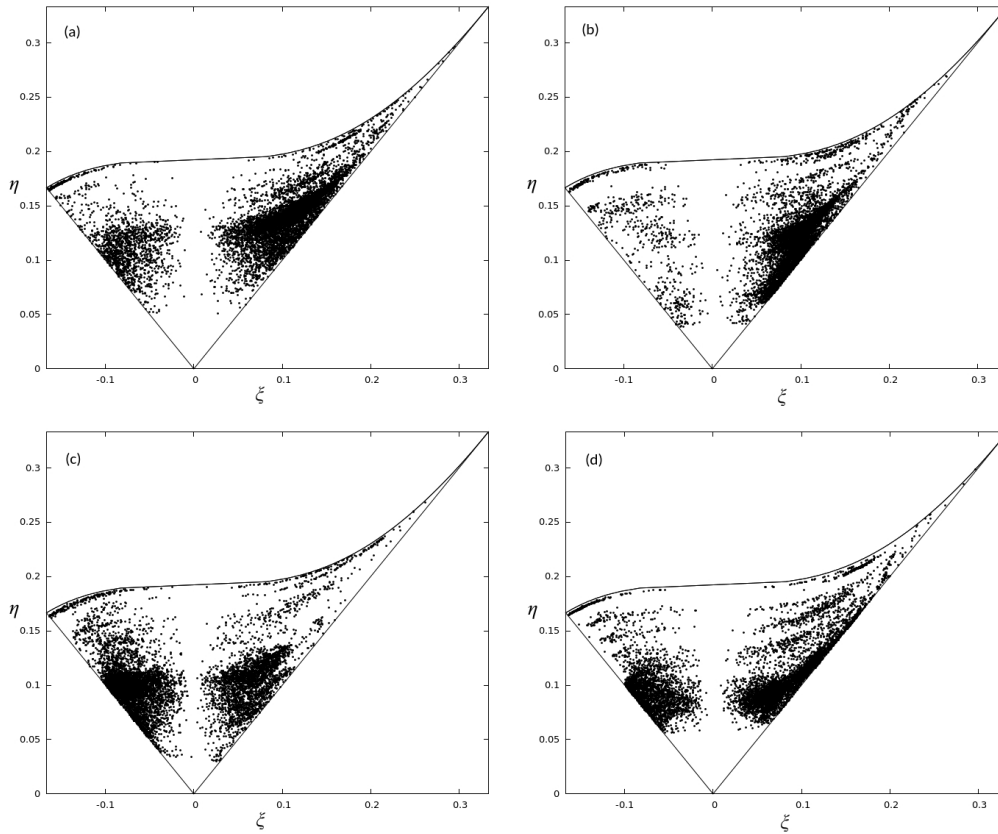
Figure 7.7: Lumley triangle for run n°1 at four cross section in the flow field: (a) $2\,m$ upstream the entrance of bend; (b) 60° in the bend; (c) 150° in the bend and (d) $2\,m$ downstream the exit of the bend. The values ($\times 10^3$) are made non-dimensional by the bulk velocity squared W_{av}^2.

For the 60° cross-section (Figure 7.7(b)), it is seen that most of the values is also located near the right straight side of the triangle. Moving from the inner bank to the outer bank, the ξ, η values move from the right side of the triangle to the left, and move towards the curved top side of the triangle, when approaching the free surface. At left straight side of the triangle, the state of the turbulence can be characterized as axisymmetric with one small eigenvalue. For this type of turbulence, the shape of the stress tensor is an oblate spheroid. The tendency of the invariants values toward the curved upper side of the triangle indicates a tendency toward two-dimensional turbulence. The presence of this tendency is explained by the high aspect ratio of the cross-section, $B/H = 8.2$.

The ξ, η values for the 150° cross-section (Figure 7.7(c)) show more or less the same behaviour as for the 60° cross-section, but with a more uniformly distribution of the values over the triangle. In the bend, there is a strong tendency of the points to move toward the origin of the triangle, which is associated with isotropic turbulence.

Beyond the bend (Figure 7.7(d)), in the straight outflow reach, the turbulence structure tends to move far away from the isotropic state, but rather slowly: at the cross-section located $2\,m$ downstream of the bend exit, the bend influences is still quite strong.

It can be concluded that in the core region of the flow (i.e., far from the walls), the turbulence is axisymmetric with one small eigenvalue of the anisotropy tensor **b**, thus displaying the typical behaviour of a plane boundary layer. This turbulence state is favoured far downstream of the inlet of the bend, with a weak tendency to isotropy in the outer half of the cross-section.

Chapter 8

Bed shear stresses

In the context of bed erosion and deposition, the bed shear stresses are relevant because they are a measure of the forces exerted on the channel bottom. When the bed shear stress exceeds a critical value, the grains situated at the bed start moving. The correct prediction of the bed shear stresses along the channel bend is also useful to estimate the distribution of the Chezy coefficient in depth-averaged 2D flow models.

The bed shear stress is related to the square of the friction velocity, denoted as w_*^2, by the water density ρ. The Equation 4.2 for the hydraulically rough bed, can directly be used to determine the friction velocity. It is applied to the total velocity vector, resulting from the two wall-parallel velocity components. In order to make the bed shear stress non dimensional, it is divided by ρ and it is scaled by the square of the bulk velocity W_{av}^2, thus obtaining the friction factor c_f. The distribution around the bend of the bed shear stress components for run n°1 and of the friction factor c_f for the two simulations are represented in Figures 8.1 and 8.2. The bed shear stresses are characterized by a very non uniform distribution, with the peak value of c_f around 10 in both runs (see Figure 8.2). The region of largest friction is located close to the inner side of the bend and covers the major part of the upstream half of the bend. On the contrary, the smallest friction is near the outer bank. Within the former region, the velocities are the highest as a
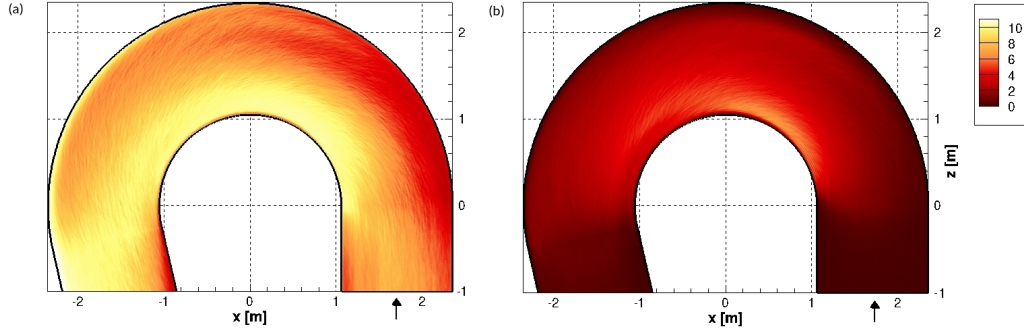
Figure 8.1: Bed shear stress components for run n°1: (a) streamwise component and (b) spanwise component. The values ($\times 10^3$) are made non-dimensional by the water density ρ and the bulk velocity squared W_{av}^2.

result of the strongly favouring pressure gradient due to the beginning of the bend and the transverse component of the bed shear stress (Figure 8.1(b)) becomes an important contributor to the total shear stress. This means that the cross flow play an important role in the scour processes in channels with high curvature. The maximum bed shear stress occurs at the inner bank just after the bend entry and it is about twice as high as the bed shear stress in the straight inflow channel. Proceeding in the downstream part of the bend, the core of maximum friction factor gradually shifts towards the outer bank (Figure 8.2). Note that the regions of high/low friction factor c_f do not correspond to scoured/deposited areas, in virtue of the strong nonlinear interaction between the complex three dimensional flow, the sediment transport and the plane configuration of the bathymetry considered in the simulation.

The curvature-induced increase of the friction factor c_f along the bend can mainly be attributed to the velocity redistribution and the gradual deformation of the vertical profiles of the velocity. The latter produces an increase of the near bed velocity gradients and, as a result, an amplification of friction factor c_f. This strong non uniform spatial distribution of c_f has important consequences for the depth-averaged 2D flow models, in which the use of a

constant value of c_f will conduct to an underestimation of flow friction near the inner bank and, hence, a less accurate prediction of the flow field and of the sediment transport processes.
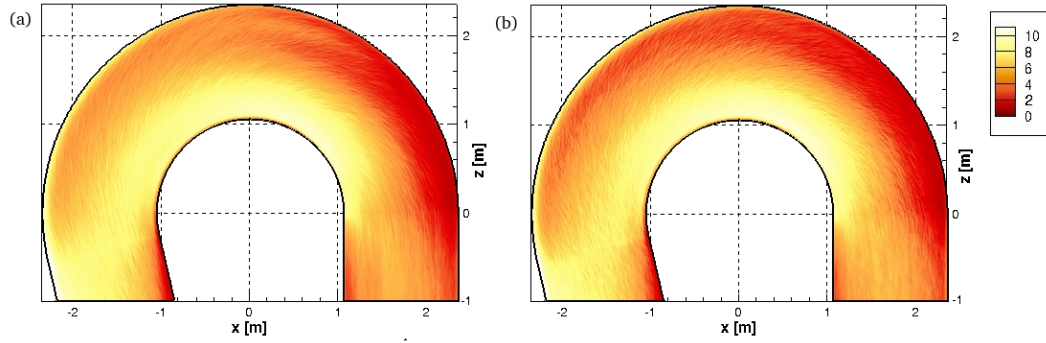
Figure 8.2: Friction factor c_f (multiplied by 10^3): (a) run n°1 ($B/H = 8.2$) and (b) run n°2 ($B/H = 9.2$).

Chapter 9

The free surface question

In meandering channels the flow undergoes centrifugal forces which make the flow field highly three-dimensional. Its main feature is the transverse inclination of the free surface which varies along the bend producing centrifugal secondary flow that deeply influences the flow behaviour. Currently, the numerical modelling of the free surface is addressed adopting one of the following methodologies:

- the Volume-of-Fluid technique;

- the Arbitrary Lagrangian Eulerian front tracking technique;

- the use of rigid-lid assumption.

From a numerical point of view, the latter is the simplest one: the free water surface is treated as a horizontal plane where the normal gradient of the variables parallel to it and the wall-normal velocity component are set to be zero (free slip condition) [92, 94, 27]. However, this simplification works rather well only for subcritical flows ($F_r < 1$), when the super-elevation of the free surface is less than 10% of the channel depth. In this context, the super-elevation effect on the flow properties can be assumed to be negligible, but this is not true in general. Hence, further efforts must be made to account for this effect.

In this chapter we consider the influence of the super-elevation of the free surface on the behaviour of turbulence in the flow field. For this purpose, it is employed the powerful software OpenFOAM and DES simulations are performed. Therefore, the test case run n°1 is again investigated by means a DES and a second test (n°1FS) is conducted considering the free-surface not horizontally, but reproducing the steady water surface detected by Blanckaert [9] in its experiment (see Figure 4.2).

9.1 Comparison results

9.1.1 Streamwise velocity in cross sections

Figure 9.1 shows the patterns of the streamwise velocity w_s in the cross sections at 60°, 90°, 120° and 150° within the bend. In the upstream part of the bend, the main flow detaches from the inner bank and the core of highest velocities progressively moves away from the convex bank. In the cross sections at 60° and 90° of the bend (Figure 9.1), a zone of convex bank flow separation is observable characterized by lower streamwise velocities between the inner bank and the core of highest velocities, with the formation of an internal shear layer. Proceeding downstream in the bend, the flow separation zone widens but the velocity difference at the edges of this zone is attenuated, as shown in Figure 9.1 for the cross sections at 120° and 150° into the bend. The low velocity region is not distributed homogeneously over the water column, indeed it tends to shrink from the free surface towards the bottom without reaching it. The principal differences between run n°1 and run n°1FS are observable in the second half of the cross sections and in particular near the outer bank where there is an increase in the water surface compared to the average value ($H = 0.159\,m$). Figure 9.1(b) shows a non-monotonic vertical distribution of the streamwise velocity in this region with the formation of a slow recirculation zone. The reduction of the streamwise velocity near the outer bank is located in the area where an outer bank cell of secondary flow occurs. Moreover in Figure 9.1(b) for the cross sections at

120° and 150°, we can note as the flow separation zone is wider than that resulting from run n°1 (Figure 9.1(a)).
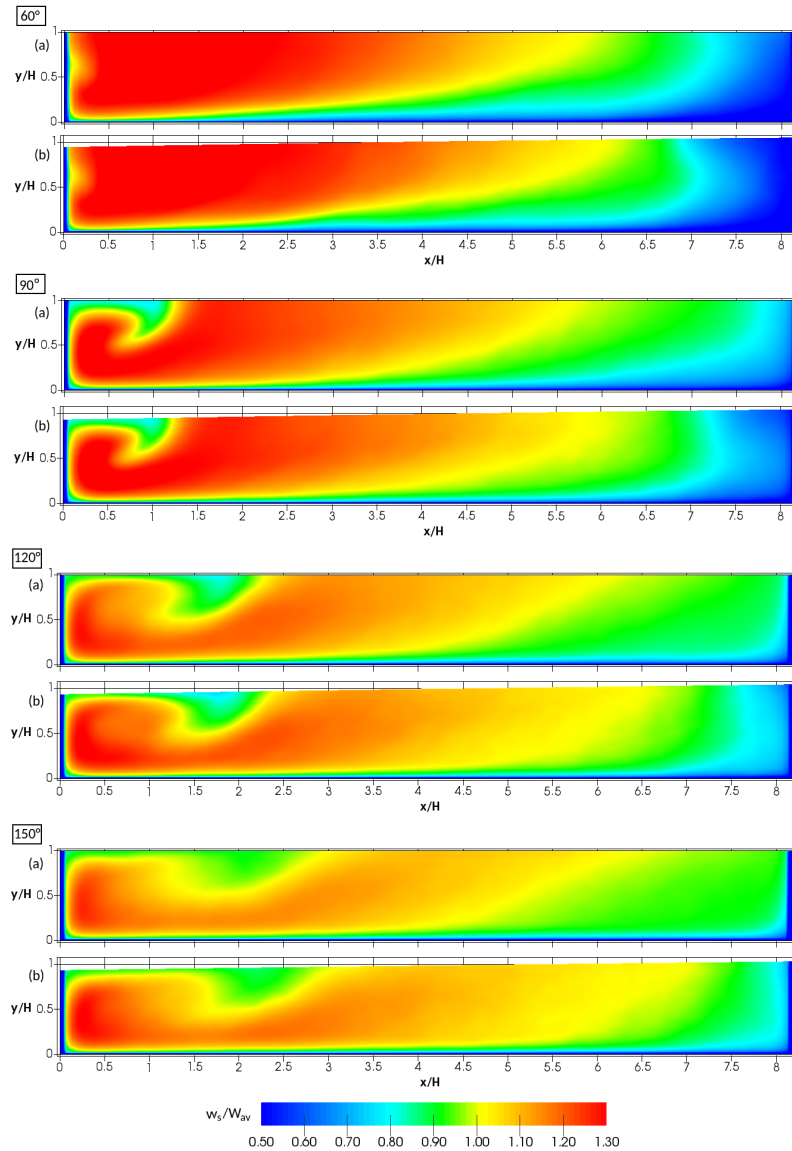
Figure 9.1: Streamwise velocity at 60°, 90°, 120° and 150° cross sections: (a) run n°1 with a horizontal water surface and (b) run n°1FS with a water surface configuration as detected experimentally by Blanckaert [9]. The values are made non-dimensional by the bulk velocity W_{av}.

9.1.2   Bed shear stress distribution

The total bed shear stresses, τ_{bs}, are made non-dimensional by the bulk velocity squared W_{av}^2 and the water density ρ, thus defining the friction factor c_f. The distributions of the bed shear stresses, expressed in terms of c_f, are shown in Figure 9.2. The comparison of the two simulations reveals the influence of the inclined water surface also on the bed shear stress distribution. In Figure 9.2(b) we can observe a pronounced increase of the friction factor c_f near the inner bank, not limited only to the first half of the bend, but which also extends towards the exit of the curve. This increase is located below the zone of the convex bank flow separation which, as shown in the Figure 9.1(b) of the velocity patterns, is more extended in the run n°1FS. Furthermore, we note a considerable transversal variation of the friction factor of over 50% which underlines the wrong choice to use a constant value of c_f in the depth-averaged flow models. A correct estimate of the forces that are exerted on the bottom is really important in the context of river engineering, indeed the shear stresses can be directly related to erosion and sedimentation processes.
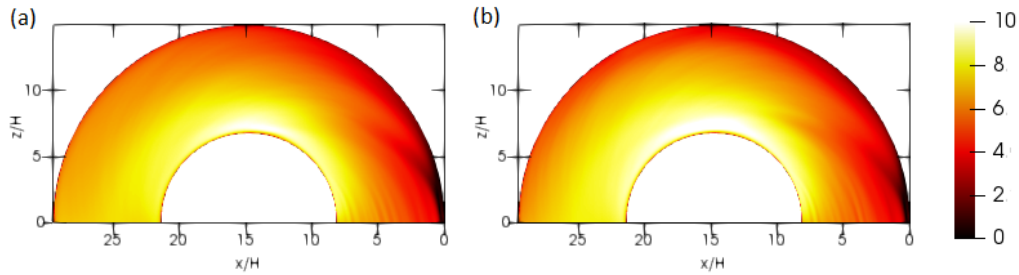
Figure 9.2: Friction factor c_f (multiplied by 10^3): (a) run n°1 with a horizontal water surface and (b) run n°1FS with a water surface configuration as detected experimentally by Blanckaert [9].

9.1.3   Patterns of flow and turbulence in the 90° cross section

The 90° cross section is analysed in detail below, as it presents the greatest variation of the water depth from the inner to the outer bank ($\Delta h = 0.018\, m$). Figure 9.3 reports the vertical profiles of the streamwise and spanwise velocities at five verticals within the 90° cross section located at $0.12\, B$, $0.3B$, $0.5\, B$, $0.7\, B$ and $0.9\, B$. The results are also compared with the experimental data of Blanckaert [9]. Within the separation zone, the streamwise velocity profiles are strongly deformed with the maximum values in the lower part of water column instead near to the water surface (Figure 9.3(a)). Close to the outer bank only the predicted profile of run n°1FS shows the measured decrease of the streamwise velocity toward the water surface (Figure 9.3(a)).
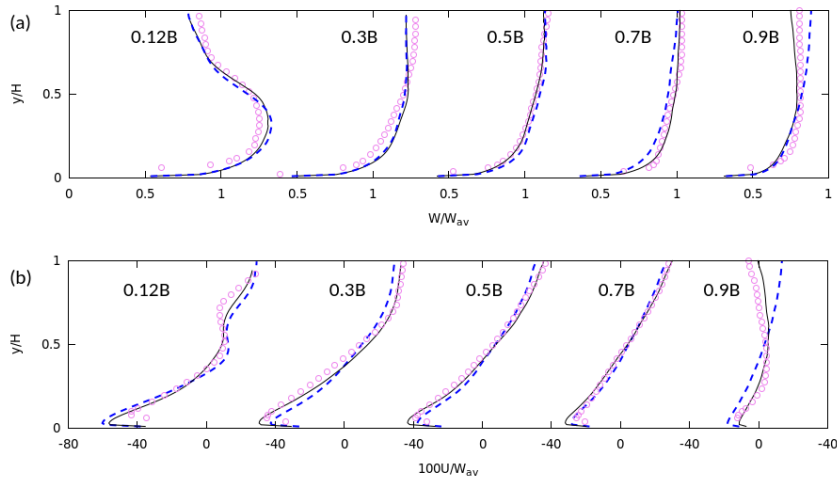
Figure 9.3: Vertical profiles at the 90° cross section: (a) streamwise velocities and (b) spanwise velocities. The circles represent the experimental results of Blanckaert [9], the dashed lines are the results of run n°1 while the solid lines refer to the results of run n°1FS. The values are made non-dimensional by the bulk velocity W_{av}.
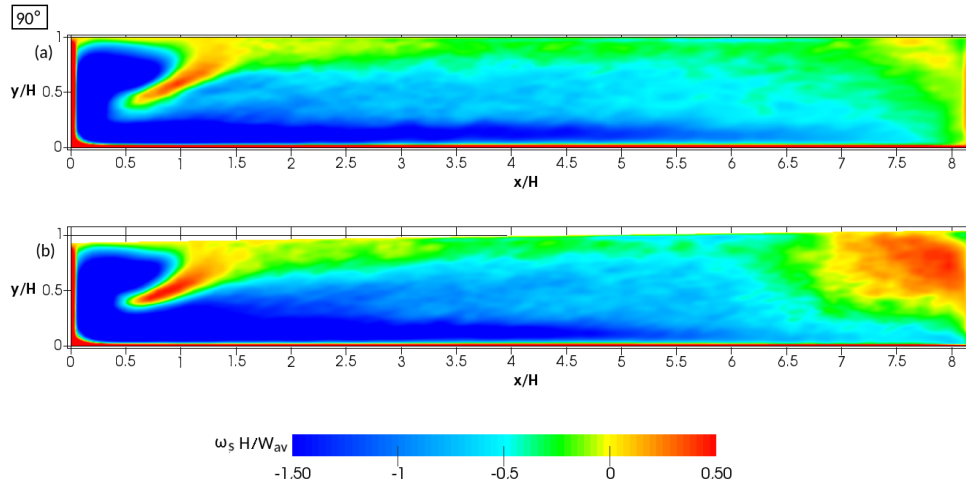
Figure 9.4: Streamwise vorticity at the 90° cross section: (a) run n°1 and (b) run n°1FS. The values are made non-dimensional by the bulk velocity W_{av} and the water depth H.

The predicted spanwise velocity profiles (Figure 9.3(b)) capture the typical helicoidal path of the curvature induced cross-stream circulation cell. In particular, run n°1FS reproduces an inflexion of the spanwise profile near the outer bank (Figure 9.3(b)) highlighting the presence of another recirculation zone. Overall, the comparison between measured and predicted velocity profiles show the best agreement for the results of run n°1FS that is able to reproduce the right behaviour near to the water surface.

Figure 9.4 shows the patterns of secondary flow in the 90° cross section, expressed in terms of the non-dimensional streamwise vorticity $\omega_s H/W_{av}$. It clearly appears the presence of an outer bank cell of secondary flow characterized by positive vorticity and a central region cell identified by an area with negative vorticity. Figure 9.4(b) reveals the important influence of the transverse inclination of the water surface into the production of centrifugal secondary flow. Indeed, in run n°1FS a more intense outer bank cell forms that can strongly affect the bank erosion processes. Along the edge of the flow separation zone at the convex bank, a zone with $\omega_s > 0$ clearly separates
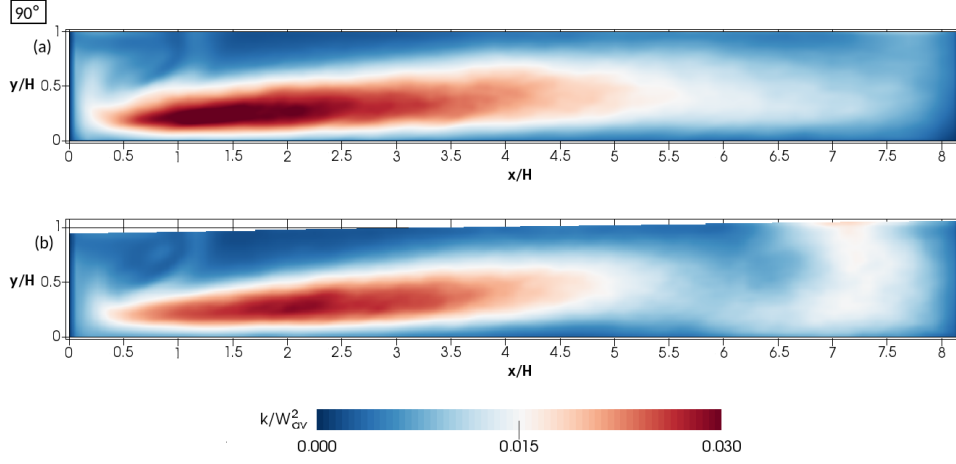
Figure 9.5: *tke* at the 90° cross section: (a) run n°1 and (b) run n°1FS. The values are made non-dimensional by the bulk velocity squared W_{av}^2.

an area of $\omega_s < 0$ within the separation zone from another area of negative vorticity induced by streamline curvature.

Figure 9.5 analyses the *tke* patterns in the cross section at 90°. We can note the dominant influence of the center circulation cell (Figure 9.4) in producing additional *tke* in the section. Figure 9.5(b) shows also an increase of the *tke* near the outer bank and close to the free surface as a consequence of the outer bank cell. The influence of the latter is clearly visible in the patterns of the turbulent normal stresses in Figure 9.6(b) with a local growth of the turbulent activity. The internal shear layer confines the streamwise flow and the cell in the central region (the core of maximum vorticity) below the zone of flow separation in the lower part of the water column. As a result, an enhancement of streamwise velocity (Figure 9.1), streamwise vorticity (Figure 9.4) and related *tke* (Figure 9.5) is obtained. The main contribution to this increase in *tke* under the flow separation zone and to the core of maximum *tke* in correspondence of the main secondary flow cell is attributed to the transverse turbulent normal stress $\langle u_s^{'} u_s^{'} \rangle$ (see Figure 9.6(II)). Instead, near to the edge of the flow separation zone is evident an increase of the *tke*

mainly related to the contribution of the streamwise turbulent normal stress $\langle w_s' w_s' \rangle$, as represented in Figure 9.6(I). Figure 9.6(III) shows that the vertical turbulent normal stress $\langle v' v' \rangle$ has a significantly lower weight in production of *tke* respect to the other two components but, nevertheless, it attains non negligible values. The turbulent shear stresses are represented in Figure 9.7
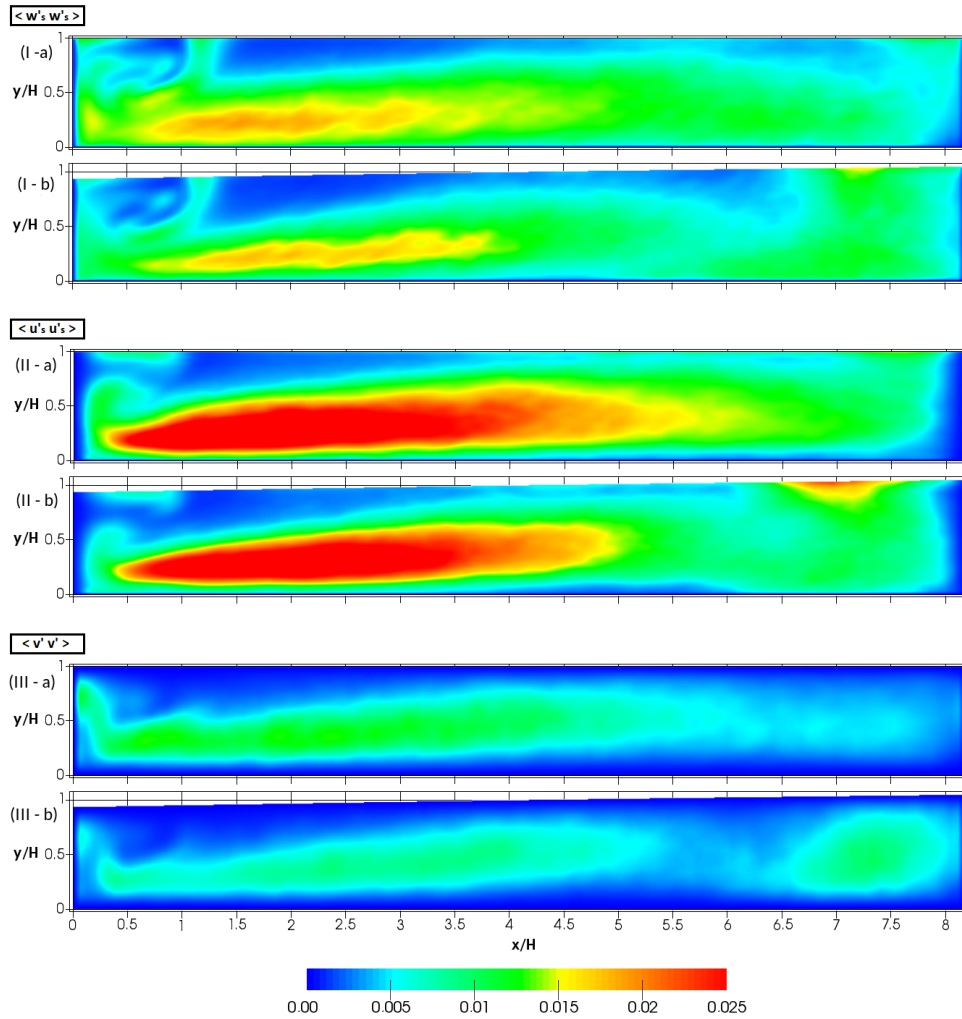
Figure 9.6: Turbulent normal stresses at 90° cross sections: (a) run n°1 and (b) run n°1FS. The values are made non-dimensional by the bulk velocity squared W_{av}^2.
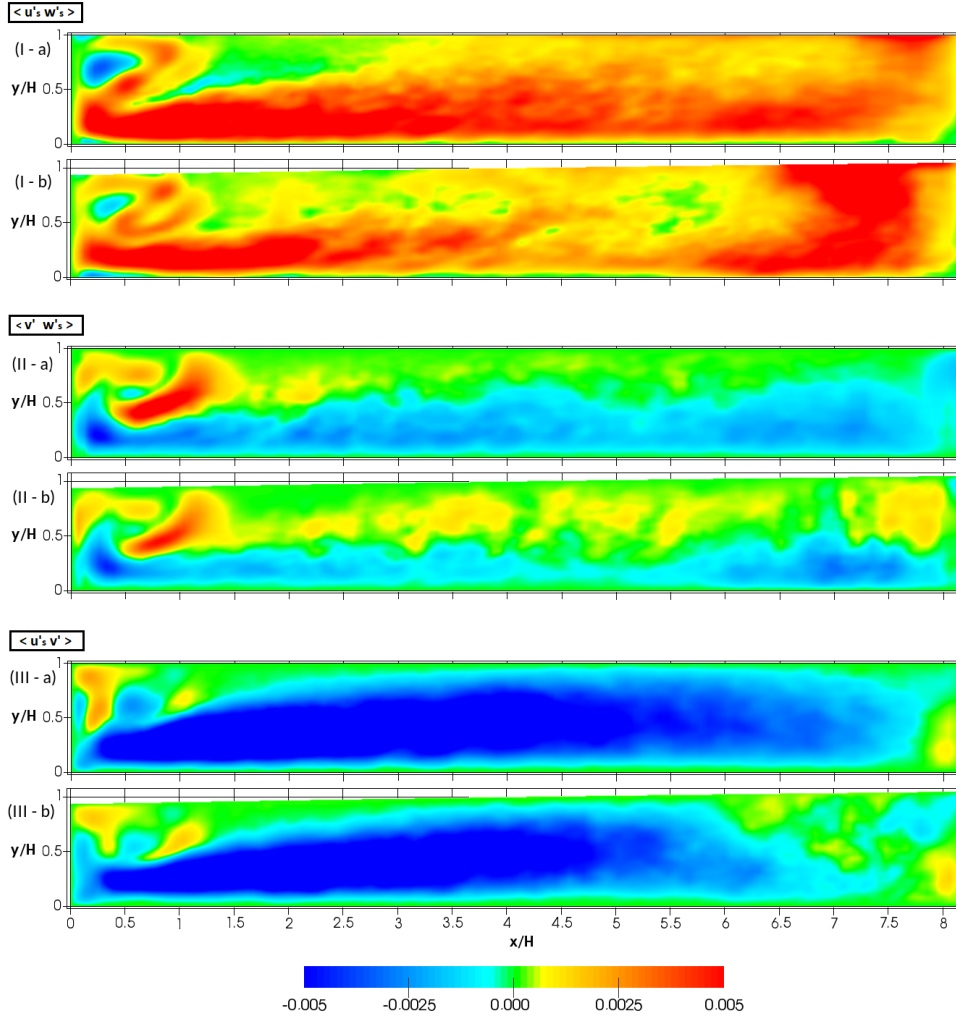
Figure 9.7: Turbulent shear stresses at the 90° cross section: (a) run n°1 and (b) run n°1FS. The values are made non-dimensional by the bulk velocity squared W_{av}^2.

for the 90° cross section of the bend. The shear stresses $\langle u_s' w_s' \rangle$ (Figure 9.7(I)) and $\langle v' w_s' \rangle$ (Figure 9.7(II)) related to streamwise velocity are characterized by high positive values in correspondence of the internal shear layer. Also the pattern of $\langle u_s' v' \rangle$ shows positive values near the edge of the flow separation region where an area of opposite vorticity occurs (Figure 9.4). Moreover,

in the $\langle u_s' v' \rangle$ pattern (Figure 9.7(III-b)) is possible to observe an area of positive values along the edge of separation between the main secondary flow cell and the outer bank cell. Figure 9.7(I) shows a pronounced variation of the pattern of $\langle u_s' w_s' \rangle$ near the inner bank in the zone of flow separation.

For a more detailed analysis on the influence of the outer bank cell in the production of turbulence shear stresses, the structure parameter a_1 (see Equation 7.4) is examined in the area near the concave bank of the 90° cross section. In Figure 9.8 is evident how the super elevation of the free surface influences the greatness of this outer circulation cell. In fact, the structure parameter a_1 is characterised by relatively low values along the interface of the two mutually counter-rotating cells where positive values of transverse-vertical stresses $\langle u_s' v' \rangle$ are observed (Figure 9.7(III-b)). In the pattern of the structure parameter a_1 is clear the footprint of the outer bank cell with a progressive increase of its values moving towards the free surface.
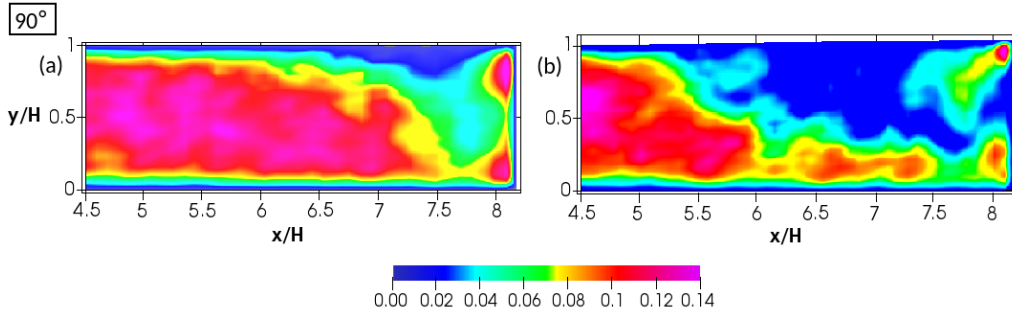
Figure 9.8: Structure parameter in the area near the outer bank of the 90° cross section: (a) run n°1 and (b) run n°1FS. The values are scaled with the bulk velocity squared W_{av}^2.

Chapter 10

Conclusion

The present work reproduces numerically the fluvial processes in sharp open-channel bends. The laboratory configuration designed by Blanckaert [6, 9] is considered in the simulations with a flat non-erodible bed to accentuate the curvature related processes.

The main characteristics of this type of complex 3D flow field are accurately simulated, such as the interaction between the deformation of the streamwise velocity profiles and the strength of the secondary flow cells, as well as the production of turbulent kinetic energy. The patterns of mean, secondary and turbulent flow quantities are examined in detail.

The region close to the inner bank is characterized by a zone of flow separation with the occurrence of high velocity gradients, a shear layer, the reversal of the vertical velocities ($v < 0$) and reversed vorticity ($\omega_s > 0$), high positive values of the turbulent shear stress $\langle u_s' v' \rangle$ and enhanced tke. The velocity profiles are strongly deformed in this zone, with low velocities near the water surface and maximum values near the bed. This leads to an increase of the bed friction coefficient and, hence, of the flow's capacity to pick up sediment. The LES simulation also predicts rather correctly the outer bank cell of cross-stream circulation measured in the corresponding flat bed experiment [102]. The secondary flow is strongly influenced by stream-line curvature, that drives the flow patterns of the flow variables and is the

dominant mechanism for the amplification of turbulent stresses and *tke* in sharp curved bends.

Two configurations of sharp bends are analyzed in the thesis: a first configuration characterized by $B/H = 8.2$ and a second configuration with a higher aspect ratio $B/H = 9.2$. The comparison of the two flow fields reveals the important influence of the water depth on the secondary flow distribution and the turbulence structure.

In the upstream part of the bend, the strength of the central cell becomes stronger when decreasing the aspect ratio. Whereas this difference is not particularly evident in the downstream part of the bend.

The outer bank cell gains strength with increasing water depth, conditioning the near-bank hydrodynamic. Indeed, the outer bank cell is known to play an important role with respect to the flow forcing on the outer bank.

The secondary flow and turbulence stresses have a similar behaviour. This increase in turbulence is a key aspect, it affects the spreading and mixing of pollutants and suspended matter, sediment transport and scour processes.

The section dedicated to "the free surface question" has emphasized the influence of the transverse inclination of the free surface on the secondary flow and the turbulent activity by means of DES simulations. The principal differences are observed close to the water surface and near the outer bank where the run n°1FS is able to capture a recirculation zone and to better reproduce the strength of the outer bank cell of secondary flow as measured by Blanckaert in its experiment [9]. Along the edge of this outer bank cell an increased *tke* occurs enhancing the sediment transport capacity and then the morphological development. The width of the separation zone is also conditioned by the transverse inclination of the free surface which influences the increase of the friction factor c_f beneath this area.

In conclusion, it is possible to state that the centripetal effects on the free-surface due to meandering need to be considered for a more complete and detailed analysis of the phenomenon. To this aim, the compatibility dynamic conditions for flows with free surface should be enforced and solved

in a Finite-Element fashion. Furthermore, an Arbitrary Lagrangian Eulerian (ALE) technique should be implemented in order to deform the grid according to the calculated super-elevations on the free-surface. A powerful implementation of the ALE framework [48] exists on the OpenFOAM library, while is not yet implemented in the LES-COAST model. That is why the OpenFOAM software has been adopted for investigating the free-surface sloping effects.

Part II

Mathematical model for meandering rivers with spatial width

Chapter 11

Introduction

Meandering rivers are the most common river pattern in the alluvial floodplains, where human settlements, industries and agriculture are most concentrated. For these reasons, meandering rivers have attracted the interest of river engineers and geoscientists since more than one century [49]. The planform geometry of meandering rivers can be described through their spatial curvature and width distributions. Brice [21] has proposed a classification of river meandering patterns based on the intensity of spatial width oscillations, which has lately refined by Lagasse et al. [53]. In Figure 11.1 the meandering configurations are ordered according to the absence or presence of spatial width variation in the channel and to the degree of width variability. This last classification is important in river meanders because the spatial width distribution plays a dynamic role similar to that of the channel curvature. The presence of more or less pronounced spatial variations in width is certainly related to the near-bank dynamics, as well as to the in-stream morphodynamic processes. Most of the mathematical models used to investigate meander morphodynamics are based on simplified analytical solutions of the equations governing the flow dynamic and the evolution of the bed topography, obtained through perturbation methods [40]. It is assumed that flow and bed topography deformation in curved channels are small with respect to the flow velocity and water depth of a corresponding straight channel with

Figure 11.1: Modified Brice [21] alluvial pattern classification of single-thread rivers reprinted from Lagasse et al. [53], (modified figure).

a flat bed characterized by the same discharge, slope, width and sediment size. This assumption for the applicability of perturbation methods is justified because in many meander bends the curvature and planform geometry are slowly varying. Therefore, most of the mathematical models employed to investigate bend stability and meander planform evolution are linear, namely the perturbation expansion are truncated at the first order of approximation (see, e.g., [29, 65]). They are based on the bend theory originally proposed by Ikeda et al. [43] and obtained by linearizing the equations of flow, sediment transport and of the planform evolution. The original bend theory and

its subsequent refinements have allowed to develop linear models of steady flow in meandering channel able to disclose a variety of characteristics of the meandering phenomenon [77]. These models have enabled to successfully predict the characteristic spatial scales of developing meanders, to understand the hydraulic and geometric conditions under which a meander can grow in loops [16, 67] and reproduce the typical meander loop migration rates [30] and shapes [80, 104]. More recently, deeper investigations about the bend theory have allowed to investigate the nature of meander instability [55] and the dominant direction of upstream/downstream 2D morphodynamic influence [88, 106, 103], distinguishing between stable or unstable bends through field observations [57]. Furthermore, linear models have played a dominant role in exploring the long-term (order of centuries) meander evolution [36, 42, 89] and they have opened new perspectives about the possible existence of a statistically universal behavior of meandering rivers [37]. A detailed summary of linear models for meandering channels with constant width and their performance can be found in Camporeale et al. [24] and in Frascati and Lanzoni [36].

In order to treat the effect of flow non-linearities, Seminara and Tubino [79] have extended the analysis at the third order of the perturbation expansion. Later on, Seminara and Solari [78] introduced a slightly different perturbation model that allowed a more complete treatment of nonlinear effects relaxing the assumption of small amplitude flow and bed perturbations. This approach was subsequently extended by Bolla Pittaluga et al. [18].

Most of the models mentioned so far assume the river width constant in time and space, imposing that, as the channel migrates laterally, the rate of bank advance is equal to the bank retreat rate. This assumption of constant width has been justified as a long-term requirement for meandering rivers and it has been supported by field observation of natural rivers characterized by fairly uniform cohesive banks [72]. However, similarly to curvature forcing induced by bends, the presence of spatial width oscillations along the channel may have significant effects on the hydrodynamic and morphody-

namic of meandering rivers [74, 105]. In this regard, Repetto et al. [74] have elaborated a linear analysis on the steady flow-bed topography that occurs in straight channels with regular width oscillations. Recently, the theory developed by Repetto et al. [74] has been extended by Frascati and Lanzoni [38] to meandering channels with arbitrarily width. On the other hand, in the case of sine-generated meanders, Luchi et al. [59] have analyzed the dynamic effects of periodic width oscillations on the process of bend stability, accounting for the planimetric forcing generated by the nonlinear interaction between curvature and width variations. Finally, the nonlinear model of flow and bed topography in meandering rivers elaborated by Bolla Pittaluga et al. [18] has been extended by Luchi et al. [58] to account for spatial width oscillations in a sequence of sine-generated meander bends.

The analytical models so far described, try to put within a rational theoretical framework the key physical processes pointed out by field observations. They, thus, provide indications on the necessary ingredients for developing a robust mathematical model that describes correctly the morphodynamic evolution of alluvial rivers: a reliable estimate of the flow field resulting from spatial distributions of channel axis curvature and width and a physically based model simulating the inner bank advance and the outer bank erosion [69].

In this Part II of the thesis, a morphodynamic model able to predict the flow field distribution and the equilibrium bed configuration of alluvial rivers characterized by arbitrary distributions of both channel width and channel axis curvature is developed. We extend the linear model proposed by Frascati and Lanzoni [38] in order to account for also the nonlinear effects arised by curvature and width oscillations. The model has an analytical character that makes it a robust and computationally sustainable tool to study the morphodynamic regime and the long-term evolution of alluvial meandering rivers. Furthermore, it can be easily incorporated in long-term models of river planform evolution or used to rapidly evaluate the morphological behaviour of alluvial rivers as a result of hydrodynamic forcing or planform geometry

variations.

This Part II is organized as follows. In Chapter 12, we derive a two-dimensional, depth-averaged model for flow and bed topography in alluvial meandering channels with both arbitrarily varying curvature and width. The linearized solution of the morphodynamic problem by means of a two-parameters perturbation approach is presented in Chapter 13. Results of a a direct application of the model to a test case (a reach of the Po River, Italy) are illustrated in Chapter 14. Finally, in Chapter 15 draws some conclusions.

Chapter 12

Mathematical formulation

This Chapter describes the mathematical model formulated for a steady, nonuniform flow in channels with arbitrarily varying curvature and width and the relative sediment transport processes. The three-dimensional governing conservation equations are depth-averaged in order to obtain a set of two-dimensional equations that takes into account the dynamic effects of secondary flows produced by curvature and width variation forcing. Afterwards, the governing equations are linearized by means of a two-parameter perturbation expansion technique based on perturbations induced by curvature and width variations.

12.1   The three dimensional model

Consider the permanent flow of a constant discharge Q^* in a meandering cohesionless channel characterized by varying distribution of both channel axis curvature $\mathcal{C}^*$ and width $2B^*$. Flow and bed topography are here referred to an orthogonal intrinsic reference system (s^*,n^*,z^*), where s^* is the longitudinal coordinate, n^* is the lateral coordinate orthogonal to s^*, and z^* is the vertical coordinate pointing upwards (see Figure 12.1). Notice that a superscript asterisk indicates dimensional variables.

The starting point of the modelling is represented by the Reynolds equa-
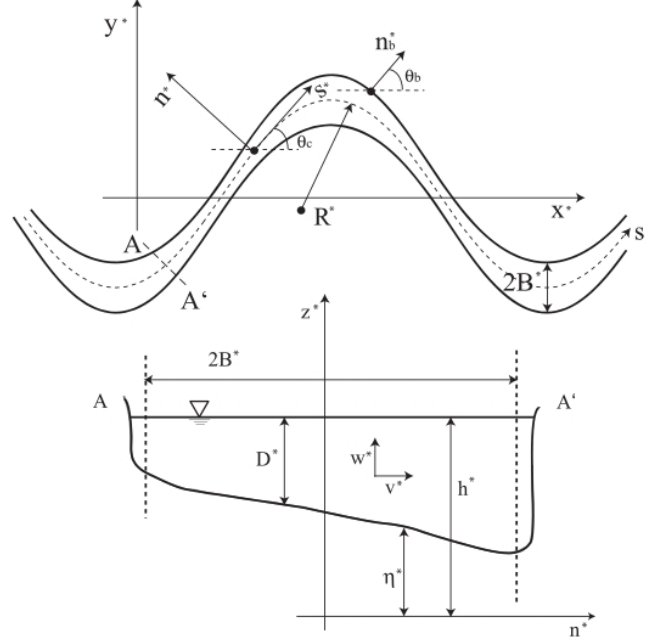
Figure 12.1: Sketch of a meandering channel with spatial varying width and notations (image from Frascati and Lanzoni [38]).

tions governing the steady turbulent flow of an incompressible fluid subject to gravity along with the continuity equations for the fluid and solid phases. Observing that for the investigated problem the horizontal scales are much larger than the flow depth, the shallow-water approximation can be applied. This assumption implies a hydrostatic distribution of pressure and we can replace the pressure gradient with the slope of the free surface. Moreover, we assume the slowly varying character of the flow field, restricting the analysis to the central part of the channel ignoring the bank region, that implies the possibility to neglect the horizontal derivatives of the stress tensor. The governing equations are then replaced in according to the orthogonal curvilinear system depicted in Figure 12.1, (more information on the derivation of the dimensional equations can be found in Frascati and Lanzoni [38]). They

read:

$$\frac{u^{*2}{}_{,s^*}}{1+n^*\mathcal{C}^*} + (u^*v^*)_{,n^*} + (u^*w^*)_{,z^*} + \frac{2\mathcal{C}^*(u^*v^*)}{1+n^*\mathcal{C}^*} = -g\frac{h^*{}_{,s^*} - C_{fu}F_{ru}^2}{1+n^*\mathcal{C}^*}$$
$$+ (\nu_T^* u^*{}_{,z^*})_{,z^*} \quad (12.1)$$

$$\frac{(u^*v^*)_{,s^*}}{1+n^*\mathcal{C}^*} + v^{*2}{}_{,n^*} + (v^*w^*)_{,z^*} + \frac{\mathcal{C}^*(v^{*2}-u^{*2})}{1+n^*\mathcal{C}^*} = -gh^*{}_{,n^*} + (\nu_T^* v^*{}_{,z^*})_{,z^*}$$
$$(12.2)$$

$$\frac{u^*{}_{,s^*}}{1+n^*\mathcal{C}^*} + \left(\frac{\mathcal{C}^*}{1+n^*\mathcal{C}^*} + \frac{\partial}{\partial n^*}\right) v^* + w^*{}_{,z^*} = 0 \qquad (12.3)$$

$$\frac{q_s{}^*{}_{,s^*}}{1+n^*\mathcal{C}^*} + \left(\frac{\mathcal{C}^*}{1+n^*\mathcal{C}^*} + \frac{\partial}{\partial n^*}\right) q_n{}^* = 0 \qquad (12.4)$$

where the comma indicates the partial derivative, $\mathbf{u}^* = (u^*, v^*, w^*)$ is the mean velocity vector (averaged over turbulence), h^* is the free surface elevation, ν_T^* the eddy viscosity, $\mathbf{q}^* = (q_s^*, q_n^*)$ is the sediment flux per unit width and g is the acceleration due to gravity. Furthermore, C_{fu} and F_{ru} are the friction coefficient and the Froude number of the reference flow, respectively. Therefore, the subscript "u" refers to properties of a uniform flow in a straight channel having the same flow discharge and grain size of the meandering river considered here, while the width and the slope of this channel are equal to their average values in the meandering reach. In the case of channels with nonuniform width it is convenient to define the following dimensionless variables:

$$
\begin{aligned}
(B^*, s^*, n^*) &= B_{avg}^*(B, s, B\,n) \\
(u^*, v^*, w^*) &= U_u^*(u, v, \frac{w}{\beta_u}) \\
(D^*, h^*, z^*) &= D_u^*(D, F_{ru}^2 h, z) \\
\mathcal{C}^* &= \frac{1}{R_0^*}\mathcal{C} \\
\nu_T^* &= \nu_T(\sqrt{C_{fu}}U_u^* D_u^*) \\
(q_s^*, q_n^*) &= \sqrt{g\frac{\rho_s - \rho}{\rho}d_s^*} \cdot d_s^*
\end{aligned}
\qquad (12.5)
$$

where B_{avg}^* is the reach averaged half width, D^* is the flow depth, ρ and ρ_s are water and particle density, respectively, d_s^* is the sediment grain size (taken

to be uniform) and R_0^* is some characteristic value of the radius of curvature of the channel axis (e.g., its minimum value in the meandering reach). By substituting the expressions (12.5) into Equations (12.1-12.4) and applying the following derivation chain rule:

$$\frac{\partial}{\partial s^*} \longrightarrow \frac{1}{B_{avg}^*}\left[\frac{\partial}{\partial s} - \frac{n}{B}B,s\frac{\partial}{\partial n}\right]$$
$$\frac{\partial}{\partial n^*} \longrightarrow \frac{1}{B_{avg}^*}\frac{1}{B}\frac{\partial}{\partial n} \tag{12.6}$$
$$\frac{\partial}{\partial z^*} \longrightarrow \frac{1}{D_u^*}\frac{\partial}{\partial z}$$

the rescaled and dimensionless governing equations are found to take the form:

$$Nu\mathcal{L}u + B^{-1}vu,_n + wu,_z + 2N\nu\mathcal{C}(uv) = -N(\mathcal{L}h - \beta_u C_{fu})$$
$$+ \beta_u\sqrt{C_{fu}}(\nu_T u,_z),_z \tag{12.7}$$

$$Nu\mathcal{L}v + B^{-1}vv,_n + wv,_z - N\nu\mathcal{C}u^2 = -B^{-1}h,_n + \beta_u\sqrt{C_{fu}}(\nu_T v,_z),_z \tag{12.8}$$

$$N\mathcal{L}u + \left(N\nu\mathcal{C} + B^{-1}\frac{\partial}{\partial n}\right)v + w,_z = 0 \tag{12.9}$$

$$N\mathcal{L}q_s + \left(N\nu\mathcal{C} + B^{-1}\frac{\partial}{\partial n}\right)q_n = 0 \tag{12.10}$$

Here, $\beta_u = B_{avg}^*/D_u^*$ is the aspect ratio of the channel, ν is the curvature ratio and $\mathcal{C}$ is the dimensionless channel axis curvature, such that:

$$\nu = \frac{B_{avg}^*}{R_0^*} \qquad\qquad \frac{\partial\theta}{\partial s} = -\nu\mathcal{C} \tag{12.11}$$

where θ is the angle that the local tangent to the channel axis forms with the direction of a Cartesian axis x^* (see Figure 12.1). Furthermore, the longitudinal metric coefficient N of the coordinate system and the differential operator $\mathcal{L}$ are defined as follows:

$$N = \frac{1}{1 + \nu n B\mathcal{C}} \qquad \mathcal{L} = \frac{\partial}{\partial s} - \frac{n}{B}B,_s\frac{\partial}{\partial n} \tag{12.12}$$

Finally, the boundary and integral conditions associated with the differential system (Equations 12.7-12.10) are:

$$u = v = w = 0, \quad z = z_0 \quad (12.13)$$

$$u_{,z} = v_{,z} = w - N\mathcal{L}(F_{ru}^2 h)u - B^{-1}F_{ru}^2 h_{,n}\, v = 0, \quad z = F_{ru}^2 h \,(12.14)$$

$$\int_{z_0}^{F_{ru}^2 h} \mathbf{u} \cdot \mathbf{n}_b \, dz = \mathbf{q} \cdot \mathbf{n}_b = 0, \quad n = \pm 1 \quad (12.15)$$

where $\mathbf{n}_b$ is the unit vector normal to the banks. They express the no-slip condition at the bed, with z_0 the reference level at which the condition is imposed under uniform conditions (12.13); the conditions of no stress at the free surface and the requirement that the latter must be a material surface (12.14); finally, the physical requirement that the channel walls be impermeable both to the flow and to the sediment (12.15). At last, three further integral conditions are required in order to close the problem. They express the requirement that flow discharge per unit width, sediment supply, and averaged reach slope are not affected by the development of perturbations either of the flow field or of the boundary configuration. These conditions will be made explicit in the following.

12.2   The structure of the secondary flow

In order to derive a depth-averaged form of the governing equations (12.7-12.10) that preserves the memory of the centrifugally induced secondary flow with zero average, the following velocity structure is assumed [51, 84]:

$$u = U(s,n)\mathcal{F}(\xi) \quad (12.16)$$

$$v = \nu\,\tilde{v}(s,n,\xi) + V(s,n)\mathcal{F}(\xi) \quad (12.17)$$

$$h = \nu\,\tilde{h}(s,n) + H(s,n) \quad (12.18)$$

Here U and V denote the depth-averaged values of u and v and H is the free surface elevation. Furthermore, $\tilde{v}$ denotes the local distribution of the transverse helical (secondary) flow and $\tilde{h}$ is the related free surface perturbation, $\mathcal{F}(\xi)$ is a dimensionless velocity shape function, while ξ is a normalized

vertical coordinate which reads:

$$\xi = \frac{z - \eta}{D} = \frac{z - (F_{ru}^2 h - D)}{D} \quad (12.19)$$

with η the dimensionless bed elevation. The flow decomposition (12.16-12.18) is equivalent to the formulation used by Johannesson and Parker [50] and Zolezzi and Seminara [106]. Since the depth averages of u and v must be equal to U and V by definition, it follows from 12.16 and 12.17 that:

$$\int_{\xi_0}^{1} \mathcal{F}(\xi)d\xi = 1 \qquad \int_{\xi_0}^{1} \tilde{v}(s,n,\xi)d\xi = 0 \quad (12.20)$$

with $\xi_0 = \xi(s,n,z_0)$ the normalized reference level for no slip. Closure relationships for the terms $\tilde{v}$ and $\tilde{h}$ are then needed. Here we refer to the method of Zolezzi and Seminara [106], who extended the analysis of Seminara and Solari [78] referring to constant-curvature channels. The method relies on the solution of equation (12.8), rewritten in terms of the coordinate system (s,n,ξ), by means of an iterative procedure adopting a slowly varying structure of the eddy viscosity profile of the form $\nu_T = UD\mathcal{N}(\xi)$. The vertical distribution of the eddy viscosity $\mathcal{N}(\xi)$ is taken to coincide with that characteristic of the uniform flow, corrected through the Dean's wake function [31]:

$$\mathcal{N}(\xi) = \frac{k\xi(1-\xi)}{1 + 2A\xi^2 + 3B\xi^3} \quad (12.21)$$

where $k = 0.41$ is the Von Karman's constant, $A = 1.84$ and $B = -1.56$. On the basis of this formulation, at the leading order of approximation $\mathcal{O}(\nu^0)$, the function $\mathcal{F}(\xi)$ is found to follow the classical logarithmic distribution, corrected by the wake function:

$$\mathcal{F}(\xi) = \frac{\sqrt{C_{fu}}}{k} \left[\ln \frac{\xi}{\xi_0} + A(\xi^2 - \xi_0^2) + B(\xi^3 - \xi_0^3) \right] \quad (12.22)$$

and from the first integral condition of (12.20) results:

$$\xi_0 \cong e^{-\frac{k}{\sqrt{C_{fu}}} - 0.777} \quad (12.23)$$

Thus we obtain that $\tilde{v}$ and $\tilde{h}$, in the present case of channel with varying width, take the form:

$$\tilde{v} = \frac{DU\mathcal{C}_s}{\beta_u \sqrt{C_{fu}}} \mathcal{G}_0(\xi) + \frac{D}{\beta_u^2 C_{fu}} \mathcal{L}(DU\mathcal{C}_s)\,\mathcal{G}_1(\xi) \qquad (12.24)$$

$$\tilde{h}_{,n} = \frac{UFr_u^2}{\beta_u \sqrt{C_{fu}}} \left[U\mathcal{C}_s\mathrm{a}_0 + U\mathcal{L}(DU\mathcal{C}_s)\mathrm{a}_1 \right] \qquad (12.25)$$

where the functions $\mathcal{G}_i(\xi)$, with $i = 0, 1$ describe the vertical structure of the secondary flow: $\mathcal{G}_0(\xi)$ accounts for the secondary flow effects associated with channel axis curvature in a fully developed flow and $\mathcal{G}_1(\xi)$ accounts for the effects associated with longitudinal convection implying a phase lag between the secondary flow and the curvature. Instead, the coefficients a_0 and a_1 depend on the vertical profiles $\mathcal{F}(\xi)$ and $\mathcal{N}(\xi)$ through the solutions of the following ordinary differential problems [106]:

$$(I) \qquad\qquad [\mathcal{N}(\xi)\mathcal{G}_{0,\xi}]_{,\xi} = \mathrm{a}_0 - \mathcal{F}(\xi)^2 \qquad (12.26)$$

$$\mathcal{G}_{0,\xi}\,|_{\xi=1} = 0 \qquad \mathcal{G}_{0,\xi}\,|_{\xi=\xi_0} = 0 \qquad \int_{\xi_0}^{1} \mathcal{G}_0 d\xi = 0$$

$$(II) \qquad\qquad [\mathcal{N}(\xi)\mathcal{G}_{1,\xi}]_{,\xi} = \mathcal{F}(\xi)\mathcal{G}_0(\xi) + \mathrm{a}_1 \qquad (12.27)$$

$$\mathcal{G}_{1,\xi}\,|_{\xi=1} = 0 \qquad \mathcal{G}_{1,\xi}\,|_{\xi=\xi_0} = 0 \qquad \int_{\xi_0}^{1} \mathcal{G}_1 d\xi = 0$$

where (I) and (II) are two boundary value problems that are numerically solved through the shooting method. Note that the structure of secondary flow, as given by (12.24-12.25), is slightly different from that proposed by Zolezzi and Seminara [106]. Indeed, the function $\mathcal{G}_2(\xi)$ which appears in Equation (3.13) of Zolezzi and Seminara [106] turns out to be redundant if the depth-averaged form of the continuity (12.9) is used to further simplify the lateral momentum equation (12.8). Furthermore, in Equations (12.24) and (12.25), $\mathcal{C}_s$ represents the curvature of the streamlines to account the deviation of the main flow from the channel axis. The relationship between streamlines and channel axis curvature can be expressed through the following dimensionless equation [63]:

$$\mathcal{C}_s(s) = \mathcal{C}(s) - \frac{1}{\nu}\frac{V_{,s}}{U} \qquad (12.28)$$

where the second term on the right side accounts for the deviation of the streamline curvature, coinciding with the channel axis in the present case, from that of the streamwise coordinate line. An appropriate assessment of this term involves a reasonable amount of algebra, therefore, following Repetto et al. [74], we can include the streamline curvature in the term accounting for centrifugal effects on transverse bottom shear stress.

12.3   A two-dimensional depth-averaged model

The problem can be tackled within the context of a two-dimensional depth-averaged model by substituting from the decomposition (12.16-12.18) and the relations (12.24-12.25) into the governing differential problem (12.7-12.10), written in terms of the normalized variable ξ, and performing a depth integration. The latter leads to the following modified system of governing equations for the morphodynamics of meandering channels:

$$\alpha\left(UU_{,s}+VU_{,n}\right)+H_{,s}+\beta_u\frac{\tau_s}{D}=\nu f_{10}+\delta f_{01}+\nu\delta f_{11}+\nu^2 f_{20} \qquad (12.29)$$

$$\alpha\left(UV_{,s}+VV_{,n}\right)+H_{,n}+\beta_u\frac{\tau_n}{D}=\nu g_{10}+\delta g_{01}+\nu\delta g_{11}+\nu^2 g_{20} \qquad (12.30)$$

$$(DU)_{,s}+(DV)_{,n}=\nu m_{10}+\delta m_{01}+\nu\delta m_{11}+\nu^2 m_{20} \qquad (12.31)$$

$$q_{s,s}+q_{n,n}=\nu n_{10}+\delta n_{01}+\nu\delta n_{11}+\nu^2 n_{20} \qquad (12.32)$$

where $\alpha=\int_{\xi_0}^1\Gamma^2(\xi)d\xi\cong 1$ is the momentum correction factor accounting for vertical velocity gradients and $H=h-\beta_u C_{fu}s$ represents the free-surface elevation with h given by (12.18). Furthermore, δ is a parameter quantifying the intensity of the width variability along the streamwise direction, such that:

$$\delta=\frac{B_0^*-B_{avg}^*}{B_{avg}^*} \qquad\qquad B=1+\delta\mathcal{B}(s) \qquad (12.33)$$

with B_0^* some characteristic value of the half width of the channel (e.g., its maximum value in the meandering reach) and $\mathcal{B}=(B^*-B_{avg}^*)/(B_0^*-B_{avg}^*)$ a quantity measuring the longitudinal variability of the width disturbances. The boundary conditions, associated to Equations (12.29-12.32), impose the

physical requirement of channel walls impermeable to flow and to sediment transport:

$$
\begin{aligned}
\mathbf{U} \cdot \mathbf{n}_b &= -UB_{,s} \pm V = 0 & (n = \pm 1) \\
\mathbf{q} \cdot \mathbf{n}_b &= -q_s B_{,s} \pm q_n = 0 & (12.34)
\end{aligned}
$$

In order to fully close the problem, additional relations are needed for determining the bed shear stress $\boldsymbol{\tau} = (\tau_s, \tau_n)$ and the sediment flux per unit width $\mathbf{q} = (q_s, q_n)$. Using the decomposition (12.16-12.17) and the solutions for $\mathcal{G}_0(\xi)$ and $\mathcal{G}_1(\xi)$, we determine an improvement in the bed shear stress expression compared to that used by Frascati and Lanzoni [38]:

$$
\begin{aligned}
|\boldsymbol{\tau}| &= \sqrt{\tau_s^2 + \tau_n^2} & (12.35) \\
\tau_s &= C_{fu}\sqrt{U^2 + V^2}\, U & (12.36) \\
\tau_n &= C_{fu}\sqrt{U^2 + V^2}\left[V + \nu\left(\frac{DUC_s}{\beta_u\sqrt{C_{fu}}}k_2 + \frac{D\mathcal{L}(DU\mathcal{C})}{\beta_u^2 C_{fu}}k_3\right)\right] & (12.37)
\end{aligned}
$$

where the coefficients k_2 and k_3, that account for centrifugal and convective secondary flows effects, are defined as follows:

$$
k_2 = \left[\frac{\mathcal{G}_{0,\xi}}{\mathcal{F}_{,\xi}}\right]_{\xi_0} \qquad\qquad k_3 = \left[\frac{\mathcal{G}_{1,\xi}}{\mathcal{F}_{,\xi}}\right]_{\xi_0} \qquad (12.38)
$$

The local value of the friction coefficient C_{fu} is related to bed configuration: in the case of plane bed we used the usual logarithmic formula [33], while in case of a dune-covered bed the formula by Engelund and Hansen [34] is employed. Finally, sediment transport is assumed to be determined by local flow conditions and its direction to deviate from that of the average bottom stress owing to the gravity action. In order to account for the gravitational effect on the direction and intensity of bedload motion, we consider the following well established approach of semi empirical nature [78, 68]:

$$
\mathbf{q} = \Phi(\tau_*; D; R_p)\left(\frac{\boldsymbol{\tau}}{|\boldsymbol{\tau}|} - \mathbf{G} \cdot \nabla_h \eta\right) \qquad (12.39)
$$

where $\mathbf{G}$ is a dimensionless second order 2-D tensor describing the gravity effects on the direction and intensity of bedload motion, $\nabla_h = (\partial/\partial s, \partial/\partial n)$

and Φ is the local bed load intensity for which several semi-empirical or empirical formulas are available in the literature. The latter is a monotonically increasing function of the Shields stress $\tau_* = |\boldsymbol{\tau}^*|/[(\rho_s - \rho)gd_s^*]$ for a given particle Reynolds number $R_p = \sqrt{(\rho_s/\rho - 1)gd_s^{*3}}/\nu_T$ and in the following it is computed with the Meyer-Peter and Müller formula as modified by Wong and Parker [98]. Note that assuming a small streamwise slope, the streamwise gravitational forces affecting particles motion can be reasonably neglected. As a consequence, Equation (12.39) reduces to:

$$(q_s, q_n) = \Phi \left(1, \frac{\tau_n}{|\boldsymbol{\tau}|} - \frac{B^{-1}}{\beta_u} \frac{r}{\sqrt{\tau_*}} \eta_{,n} \right) \qquad (12.40)$$

with r an empirical constant ranging about $0.5 - 0.6$ [90]. Furthermore, we must guarantee that in any cross section the flow and sediment discharge are constant and that the averaged reach slope is not altered by the development of perturbations. We thus impose the following integral constraints:

$$\int_{-1}^{1} UDBdn = 2 \qquad\qquad \int_{-1}^{1} \Phi Bdn = 2\Phi_u \qquad (12.41)$$

$$\int_{0}^{L} \int_{-1}^{1} (F_{ru}^2 H - D)Bdnds = const. \qquad (12.42)$$

where L is the overall streamwise length of the investigated reach.

The quantities f_{ij}, g_{ij}, m_{ij}, and n_{ij} which appear in the right-hand sides of Equations (12.29-12.32) express the forcing effect arising from the presence of curvature and width variations at different $(ij - th)$ orders of approximations, where the subfixes i and j refer to the $\mathcal{O}(\nu^i)$ and $\mathcal{O}(\delta^j)$ contributions, respectively. Note that, the model previously developed by Frascati and Lanzoni [38] is limited to the first approximation order. The curvature forcing effects are due to first $\mathcal{O}(\nu)$ and second $\mathcal{O}(\nu^2)$ order terms, while the channel width variations force the system in the form of a first-order contribution $\mathcal{O}(\delta)$. Moreover, the $\mathcal{O}(\nu\delta)$ term represents the mixed forcing due to width and curvature variations characteristic of meandering channels with longitudinal width variations. The $\mathcal{O}(\delta^2)$ component is not considered, since its contribution is supposed to play a minor role [105]. The expressions of these

functions are given in Appendix B.1. They involve the coefficients k_0, k_1 and k_4, k_5, k_6 defined as:

$$k_i = \int_{\xi_0}^1 \mathcal{F}\mathcal{G}_i d\xi \qquad (i = 0, 1) \tag{12.43}$$

$$k_4 = \int_{\xi_0}^1 \mathcal{G}_0 \mathcal{G}_0 d\xi \qquad k_5 = \int_{\xi_0}^1 \mathcal{G}_0 \mathcal{G}_1 d\xi \qquad k_6 = \int_{\xi_0}^1 \mathcal{G}_1 \mathcal{G}_1 d\xi \tag{12.44}$$

which account for the dispersive effects due to the nonlinear interactions between the secondary flow components and the longitudinal flow.

Chapter 13

The linearized form of the problem

The curvature and channel width distributions are assumed to be slowly varying in the streamwise direction. As a consequence, flow and bed topography "weakly" deviate from the base solution. This hypothesis of small-amplitude curvature and width variations, mathematically expressed by (12.11) and (12.33), allows us to linearize the problem (12.29-12.32, 12.34). We note that this is a fairly restrictive assumption. However, Seminara and Solari [78] suggested that linearity is likely to be a reasonable approximation if the following relationship is satisfied:

$$\epsilon = \nu \frac{\sqrt{\tau_*}}{r\, C_{fu}} < 10 \tag{13.1}$$

where ϵ is a parameter controlling the intensity of bottom variation.

Given the typically wide character of river bends and the usually limited character of width variations, the solution can be expanded in powers of the small perturbation parameters ν and δ:

$$(U, V, D, H) = (1, 0, 1, H_0) + \nu(u_c, v_c, d_c, h_c) + \delta(u_b, v_b, d_b, h_b) +$$
$$\nu\delta(u_{cb}, v_{cb}, d_{cb}, h_{cb}) + \nu^2(u_{cc}, v_{cc}, d_{cc}, h_{cc}) + ... \tag{13.2}$$

where $H_0 = H_r - \beta C_{fu}s$, having denoted with H_r a reference water surface elevation ($H_r = 1$), while (u_c, v_c, d_c, h_c), (u_b, v_b, d_b, h_b), $(u_{cb}, v_{cb}, d_{cb}, h_{cb})$ and

$(u_{cc}, v_{cc}, d_{cc}, h_{cc})$ are the perturbations associated with channel width and channel axis curvature variations up to the second order of approximation. Note that terms of order higher than the second are supposed to play a minor role. In order to derive the final differential problems, it is necessary to expand also the terms C_{fu}, τ_* and Φ:

$$
\begin{aligned}
C_f &= C_{fu}\left(1 + \nu C_{f1} + \delta C_{f2} + \nu\delta C_{f3} + \nu^2 C_{f4}\right) \\
\tau_* &= \tau_{*u}\left(1 + \nu\tau_{*1} + \delta\tau_{*2} + \nu\delta\tau_{*3} + \nu^2\tau_{*4}\right) \\
\Phi &= \Phi_u\left(1 + \nu\Phi_1 + \delta\Phi_2 + \nu\delta\Phi_3 + \nu^2\Phi_4\right)
\end{aligned}
\tag{13.3}
$$

This method assumes that the friction coefficient, the Shields parameter and the intensity of sediment transport are in a quasi-equilibrium condition and, therefore, are evaluated in terms of local values of the relevant flow and sediment transport parameters. The latter assumption can be used because the flow field and the sediment dynamics are characterized by slow variations. The expressions of coefficients C_{fi}, τ_{*i} and Φ_i with $i = 1, 2, 3, 4$ are reported in Appendix B.2.

On substituting (13.2 and 13.3) into Equations (12.29-12.32) and into the boundary conditions (12.34), a system of partial differential equations (PDE) is obtained at each order of approximation, corresponding to a different physical mechanism:

- $\mathcal{O}(\nu)$: flow and bed topography components linearly forced by curvature in meanders with constant width;

- $\mathcal{O}(\nu^2)$: second-order non linear components of flow and bed topography forced by curvature in meanders with constant width;

- $\mathcal{O}(\delta)$: flow and bed topography components linearly forced by width variations in a straight channels with variable width;

- $\mathcal{O}(\nu\delta)$: first nonlinear interaction which expresses the mixed response of flow and bed topography in meanders with variable width.

13.1 The linear response forced by width variations $\mathcal{O}(\delta)$

The linear differential problem describing the $\mathcal{O}(\delta)$ response of the flow field and the bed configuration to the forcing induced by channel width variations reads as:

$$
\begin{cases}
\left(\frac{\partial}{\partial s} + a_1\right) u_b + a_2 d_b + \frac{\partial h_b}{\partial s} = 0 \\
\left(a_7 \frac{\partial}{\partial s} + a_3\right) v_b + \frac{\partial h_b}{\partial n} = 0 \\
\frac{\partial u_b}{\partial s} + \frac{\partial v_b}{\partial n} + \frac{\partial d_b}{\partial s} = 0 \\
a_4 \frac{\partial u_b}{\partial s} + \left(\frac{\partial}{\partial n} + a_8 \frac{\partial^2}{\partial s \partial n}\right) v_b + \left(a_5 \frac{\partial}{\partial s} + a_6 \frac{\partial^2}{\partial n^2}\right) d_b - a_6 F_{ru}^2 \frac{\partial^2 h_b}{\partial n^2} = 0
\end{cases}
\tag{13.4}
$$

with the associated nonhomogeneous boundary conditions ($n = \pm 1$):

$$
v_b = \pm \mathcal{B}'; \qquad\qquad \left(F_{ru}^2 h_b - d_b\right)_{,n} = -b_5 \frac{\partial v_b}{\partial s}
\tag{13.5}
$$

where $\mathcal{B}'$ denotes the first derivative of dimensionless width variations, while the a_i $(i = 1, 8)$ and b_5 coefficients are reported in Appendix B.3. Furthermore we can schematically indicate with $\mathbb{L}$ the corresponding linear differential operator:

$$
\mathbb{L} =
\begin{pmatrix}
\left(\frac{\partial}{\partial s} + a_1\right) & 0 & a_2 & \frac{\partial}{\partial s} \\
0 & \left(a_7 \frac{\partial}{\partial s} + a_3\right) & 0 & \frac{\partial}{\partial n} \\
\frac{\partial}{\partial s} & \frac{\partial}{\partial n} & \frac{\partial}{\partial s} & 0 \\
a_4 \frac{\partial}{\partial s} & \left(\frac{\partial}{\partial n} + a_8 \frac{\partial^2}{\partial s \partial n}\right) & \left(a_5 \frac{\partial}{\partial s} + a_6 \frac{\partial^2}{\partial n^2}\right) & -a_6 F_{ru}^2 \frac{\partial^2}{\partial n^2}
\end{pmatrix}
\tag{13.6}
$$

The perturbations of the flow field induced by channel width variations are expanded as:

$$u_b = u_{b_0} + \sum_{m=1}^{\infty} u_{b_m} \cos(M_b n)$$

$$v_b = \overline{v}_b\, n + \sum_{m=1}^{\infty} v_{b_m} \sin(M_b n)$$

$$h_b = \overline{h}_b\, n^2 + h_{b_0} + \sum_{m=1}^{\infty} h_{b_m} \cos(M_b n) \qquad (13.7)$$

$$d_b = \overline{d}_b\, n^2 + d_{b_0} + \sum_{m=1}^{\infty} d_{b_m} \cos(M_b n)$$

where $M_b = m\pi$ and:

$$\overline{v}_b = \mathcal{B}'$$

$$\overline{h}_b = -\frac{1}{2}(a_3 \mathcal{B}' + a_7 \mathcal{B}'') \qquad (13.8)$$

$$\overline{d}_b = F_{ru}^2 \overline{h}_b - \frac{a_8}{2a_6}\mathcal{B}''$$

Note that the Fourier expansions (13.7) along with conditions (13.8) are selected in order to satisfy the boundary conditions (13.5) and to respect the antisymmetric character of v_b and the symmetric character of u_b, h_b and d_b due to width variations. The $\mathcal{O}(\delta)$ solution for the first Fourier mode ($m = 0$) can be obtained using the integral conditions (12.42), it becomes:

$$u_{b0} = c_1 \mathcal{B}$$

$$h_{b0} = -c_1 \mathcal{B} - A_{b0}\overline{h}_b - (a_1 c_1 + a_2 c_2) \int_0^s \mathcal{B}\, d\tilde{s} \qquad (13.9)$$

$$d_{b0} = c_2 \mathcal{B} - A_{b0}\overline{d}_b$$

where:

$$c_1 = \frac{a_5 - 1}{a_4 - a_5}; \qquad\qquad c_2 = \frac{1 - a_4}{a_4 - a_5}; \qquad\qquad A_{b0} = \frac{1}{3} \qquad (13.10)$$

The solution for the higher lateral Fourier modes ($m > 0$), instead, is found introducing the relations (13.7) and (13.8) into Equations (13.4) and (13.5).

The following system of four ordinary differential Equations with constant coefficients is obtained:

$$\left(\frac{d^4}{ds^4} + \sigma_{b3}\frac{d^3}{ds^3} + \sigma_{b2}\frac{d^2}{ds^2} + \sigma_{b1}\frac{d}{ds} + \sigma_{b0} \right) u_{bm} = A_{bm} \sum_{i=1}^{4} \rho_{bi}\mathcal{B}^i \qquad (13.11)$$

$$\begin{cases} v_{bm} = \sum_{i=1}^{4} v_{bm_i}u_{bm}{}^{i-1} + A_{bm}\sum_{i=1}^{5} v_{bm_i}^b \mathcal{B}^{i-1} \\ h_{bm} = \sum_{i=1}^{4} h_{bm_i}u_{bm}{}^{i-1} + A_{bm}\sum_{i=1}^{5} h_{bm_i}^b \mathcal{B}^{i-1} \\ d_{bm} = \sum_{i=1}^{4} d_{bm_i}u_{bm}{}^{i-1} + A_{bm}\sum_{i=1}^{5} d_{bm_i}^b \mathcal{B}^{i-1} \end{cases} \qquad (13.12)$$

where $A_{bm} = (-1)^m 4/M_b^2$ quantifies the decaying contribution of the higher lateral Fourier modes, while σ_{bi}, ρ_{bi}, v_{bm_i}, h_{bm_i}, d_{bm_i}, $v_{bm_i}^b$, $h_{bm_i}^b$ and $d_{bm_i}^b$ are coefficients depending on the relevant physical parameters $(\beta_u, d_s, \tau_{*u})$ and their expression is provided in Appendix C.1. By means of the method of variation of parameters, the nonhomogeneous constant coefficient ordinary differential Equation (13.11) is solved in closed form. Once the solution for u_{bm} is known, the remaining dependent variables can be solved in cascade for the mth Fourier mode by employing Equation (13.12). The general solution for longitudinal velocity perturbation is found to be:

$$\begin{aligned} u_{bm} = &\sum_{j=1}^{4} c_{bm_j}e^{\lambda_{bm_j}s} \\ &+ A_{bm}\sum_{j=1}^{4}\left[g_{bj0}\int_0^s e^{\lambda_{bm_j}(s-\xi)}\mathcal{B}(\xi)d\xi + g_{bj1}\mathcal{B} \right] \end{aligned} \qquad (13.13)$$

where c_{bm_j} ($m = 1, \infty$ and $j = 1, 4$) are integration constants to be determined on the basis of the upstream and downstream boundary conditions of the channels and g_{bjk} ($j = 1, 4$ and $k = 0, 1$) are constant coefficients depending on β_u, d_s, τ_{*u}, reported in Appendix C.1. Moreover, the characteristics coefficients λ_{bm_j} are the solution of the corresponding ordinary differential Equation, whose solution is described in Appendix C.1. Analyzing the solution (13.13), we can note that the flow and the bed topography of a meander channel, at each given section, are influenced by the local value of the width, through the term $\mathcal{B}$, and by the hydrodynamics and morphodynamics of the

reaches located upstream (downstream influence) or downstream (upstream influence), through the four convolution integrals.

The spatial width variations cause laterally symmetrical flow-bed topography patterns. They tend to induce the formation of central bar pattern in the widest sections of the channel [105], as shown in Figure 13.1.
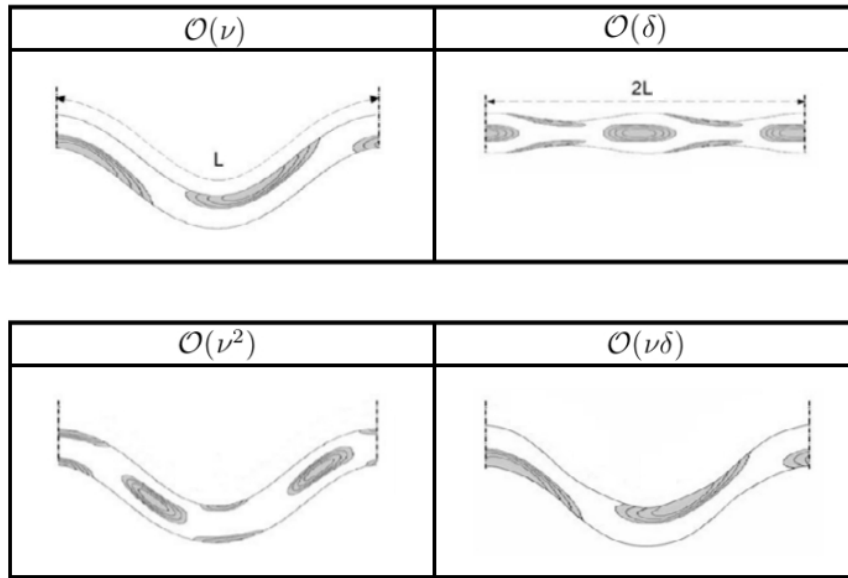
Figure 13.1: Sketch of the bedform pattern corresponding to each perturbation order. Modified from Zolezzi et al. [105].

13.2 The linear response forced by channel curvature $\mathcal{O}(\nu)$

The nonhomogeneous linear differential problem describing the response of flow field and bed configuration to the forcing induced by channel curvature

variations $\mathcal{O}(\nu)$ reads as:

$$
\mathbb{L}
\begin{pmatrix}
u_c \\
v_c \\
d_c \\
h_c
\end{pmatrix}
=
\begin{pmatrix}
nb_1\mathcal{C} \\
b_2\mathcal{C} + b_3\mathcal{C}' + b_4\mathcal{C}'' \\
0 \\
0
\end{pmatrix}
\tag{13.14}
$$

with the associated boundary conditions $(n = \pm 1)$:

$$
v_c = 0; \qquad \left(F_{ru}^2 h_c - d_c\right)_{,n} = -b_5\frac{\partial v_c}{\partial s} + b_5\mathcal{C} + b_6\mathcal{C}' \tag{13.15}
$$

where the b_i $(i = 1, 6)$ coefficients are reported in Appendix B.3, while $\mathcal{C}'$ and $\mathcal{C}''$ represent the first and second derivatives of the channel axis. The problem described in (13.14) and (13.15) is similar to that presented by Zolezzi and Seminara [106], where they do not consider the curvature variation. It can be transformed into a linear system of ordinary differential equations by adopting the method of separation of variables and introducing the following Fourier expansions in order to satisfy the boundary conditions (13.15) and to respect the symmetric character of v_c and the antisymmetric character of u_c, h_c and d_c, typically associated with alternate channel bending:

$$
\begin{aligned}
u_c &= \sum_{m=0}^{\infty} u_{cm} \sin\left(M_c n\right) \\
v_c &= \sum_{m=0}^{\infty} v_{cm} \cos\left(M_c n\right) \\
h_c &= \overline{h}_c\, n + \sum_{m=0}^{\infty} h_{cm} \sin\left(M_c n\right) \\
d_c &= \overline{d}_c\, n + \sum_{m=0}^{\infty} d_{cm} \sin\left(M_c n\right)
\end{aligned}
\tag{13.16}
$$

where $M_c = (2m + 1)\pi/2$ and:

$$
\begin{aligned}
\overline{h}_c &= \overline{h}_{c1}\mathcal{C} + \overline{h}_{c2}\mathcal{C}' + \overline{h}_{c3}\mathcal{C}'' \\
\overline{d}_c &= \overline{d}_{c1}\mathcal{C} + \overline{d}_{c2}\mathcal{C}' + \overline{d}_{c3}\mathcal{C}'')
\end{aligned}
\tag{13.17}
$$

with:

$$\overline{h}_{c1} = b_2 \qquad \overline{h}_{c2} = b_3 \qquad \overline{h}_{c3} = b_4 \qquad (13.18)$$
$$\overline{d}_{c1} = F_{ru}^2\overline{h}_{c1} - b_5 \qquad \overline{d}_{c2} = F_{ru}^2\overline{h}_{c2} - b_6 \qquad \overline{d}_{c3} = F_{ru}^2\overline{h}_{c3}$$

The $\mathcal{O}(\nu)$ solution for all the Fourier modes is found substituting the expansions (13.16) into Equations (13.14) and (13.15). Eventually, the following system of four ordinary differential equations with constant coefficients is obtained:

$$\left(\frac{d^4}{ds^4} + \sigma_{c3}\frac{d^3}{ds^3} + \sigma_{c2}\frac{d^2}{ds^2} + \sigma_{c1}\frac{d}{ds} + \sigma_{c0}\right)u_{cm} = A_{cm}\sum_{i=0}^{4}\rho_{ci}\mathcal{C}^i \qquad (13.19)$$

$$\begin{cases} v_{cm} = \sum_{i=1}^{4} v_{cm_i}u_{cm}{}^{i-1} + A_{cm}\sum_{i=1}^{5} v_{cm_i}^c \mathcal{C}^{\,i-1} \\ h_{cm} = \sum_{i=1}^{4} h_{cm_i}u_{cm}{}^{i-1} + A_{cm}\sum_{i=1}^{5} h_{cm_i}^c \mathcal{C}^{\,i-1} \\ d_{cm} = \sum_{i=1}^{4} d_{cm_i}u_{cm}{}^{i-1} + A_{cm}\sum_{i=1}^{5} d_{cm_i}^c \mathcal{C}^{\,i-1} \end{cases} \qquad (13.20)$$

where $A_{cm} = (-1)^m 2/M_c^2$ and the coefficients σ_{ci}, ρ_{ci}, v_{cm_i}, h_{cm_i}, d_{cm_i}, $v_{cm_i}^c$, $h_{cm_i}^c$ and $d_{cm_i}^c$ (reported in Appendix C.2) are functions of the physical parameters β_u, d_s, τ_{*u}. The general solution for longitudinal velocity perturbation is found to be:

$$u_{cm} = \sum_{j=1}^{4} c_{cm_j}e^{\lambda_{cm_j}s}$$
$$+ A_{cm}\sum_{j=1}^{4}\left[g_{cj0}\int_0^s e^{\lambda_{cm_j}(s-\xi)}\mathcal{C}(\xi)d\xi + g_{cj1}\mathcal{C}\right] \qquad (13.21)$$

where c_{cm_j} ($m = 1, \infty$ and $j = 1, 4$) are integration constants depending on the channel boundary conditions, while g_{cjk} ($j = 1, 4$ and $k = 0, 1$) are constant coefficients depending on β_u, d_s, τ_{*u} and their expression is reported in Appendix C.2. Once the solution for u_{cm} is known, the remaining dependent variables can be solved in cascade for the mth Fourier mode by employing Equation (13.20). Note that the characteristics coefficients λ_{cm_j} are the solution of the corresponding ordinary differential equation and the whole procedure on how to solve the problem (13.19, 13.20) is described in

Appendix C.2. A comment on the integration constants c_{cmj} and c_{bmj} can be here worthwhile. The influence of the integration constants on the flow field is local, owing to the rapid decay of the exponential functions they multiply. Therefore, they can be set to zero when evaluating the equilibrium bed topography in a river reach for a given flow discharge, although it is known that they have a certain importance in the long-term simulations of the river planform evolution [55].

The channel curvature, differently from width variation, is usually responsible of laterally antisymmetric bed patterns. It reproduces the classical point bar morphology with a sequences of scour/deposition zones (see Figure 13.1).

13.3   The non-linear response forced by channel curvature $\mathcal{O}(\nu^2)$

The nonhomogeneous differential problem describing the second order $\mathcal{O}(\nu^2)$ response of the flow field and the bed configuration to the forcing induced by channel curvature variations is obtained not considering the deviation of the main flow from the channel axis direction ($C_s = C$) in order to reduce the complexity of the long algebraic work. It results:

$$\mathbb{L} \begin{pmatrix} u_{cc} \\ v_{cc} \\ d_{cc} \\ h_{cc} \end{pmatrix} = \begin{pmatrix} K_1^{cc}(s,n) \\ K_2^{cc}(s,n) \\ K_3^{cc}(s,n) \\ K_4^{cc}(s,n) \end{pmatrix} \tag{13.22}$$

with the associated boundary conditions ($n = \pm 1$):

$$v_{cc} = 0;$$
$$\left(F_{ru}^2 h_{cc} - d_{cc} \right)_{,n} = [b_6(u_{c,s} + d_{c,s}) + b_7 u_c + b_8 d_c]\mathcal{C} + (b_9 u_c + b_{10} d_c)\mathcal{C}' \tag{13.23}$$

where the b_i ($i = 6, 10$) coefficients are reported in Appendix B.4. Note that the operator $\mathbb{L}$ in the system (13.22) differs from (13.6) through the

coefficients a_7 and a_8, which in this case read as:

$$a_7 = 1; \qquad\qquad a_8 = 0 \qquad\qquad (13.24)$$

The forcing terms $K_i^{cc}(s, n)$ $(i = 1, 4)$ are the products between two $\mathcal{O}(\nu)$ terms and $\mathcal{O}(\nu)$ terms related to channel curvature $\mathcal{C}$ and its derivatives. They are reported in Appendix B.4 and can be divided into four types of contributions:

$$K_1^{cc} = \mathbb{B}_{10}^{cc}(s) + \mathbb{B}_{11}^{cc}(s) \sum_{m=0}^{\infty} \kappa_m^{11} \cos(M_c n) +$$

$$\mathbb{B}_{12}^{cc}(s) \sum_{m=0}^{\infty} \sum_{i=0}^{m} \kappa_{i,m-i}^{12} \cos(M_{cc}^I n) + \mathbb{B}_{13}^{cc}(s) \sum_{m=0}^{\infty} \sum_{i=0}^{m} \kappa_{i,m-i}^{13} \cos(M_{cc}^{II} n)$$

$$K_2^{cc} = \mathbb{B}_{20}^{cc}(s) + \mathbb{B}_{21}^{cc}(s) \sum_{m=0}^{\infty} \kappa_m^{21} \sin(M_c n) +$$

$$\mathbb{B}_{22}^{cc}(s) \sum_{m=0}^{\infty} \sum_{i=0}^{m} \kappa_{i,m-i}^{22} \sin(M_{cc}^I n) + \mathbb{B}_{23}^{cc}(s) \sum_{m=0}^{\infty} \sum_{i=0}^{m} \kappa_{i,m-i}^{23} \sin(M_{cc}^{II} n)$$

$$K_3^{cc} = \mathbb{B}_{30}^{cc}(s) + \mathbb{B}_{31}^{cc}(s) \sum_{m=0}^{\infty} \kappa_m^{31} \cos(M_c n) +$$

$$\mathbb{B}_{32}^{cc}(s) \sum_{m=0}^{\infty} \sum_{i=0}^{m} \kappa_{i,m-i}^{32} \cos(M_{cc}^I n) + \mathbb{B}_{33}^{cc}(s) \sum_{m=0}^{\infty} \sum_{i=0}^{m} \kappa_{i,m-i}^{33} \cos(M_{cc}^{II} n)$$

$$K_4^{cc} = \mathbb{B}_{40}^{cc}(s) + \mathbb{B}_{41}^{cc}(s) \sum_{m=0}^{\infty} \kappa_m^{41} \cos(M_c n) +$$

$$\mathbb{B}_{42}^{cc}(s) \sum_{m=0}^{\infty} \sum_{i=0}^{m} \kappa_{i,m-i}^{42} \cos(M_{cc}^I n) + \mathbb{B}_{43}^{cc}(s) \sum_{m=0}^{\infty} \sum_{i=0}^{m} \kappa_{i,m-i}^{43} \cos(M_{cc}^{II} n)$$

$$(13.25)$$

where:

$$M_{cc}^I = (2i - m)\pi; \qquad\qquad M_{cc}^{II} = (m + 1)\pi \qquad (13.26)$$

We can observe a symmetric structure for the forcing terms of longitudinal momentum, flow and sediment continuity equations, instead an antisymmetric structure for those of the lateral momentum equation. Given the linear nature of system (13.22), it can be solved by separating it into four subsystems and proceeding in a similar way to that adopted for $\mathcal{O}(\delta)$ and $\mathcal{O}(\nu)$

problems. In this work we consider only the forcing contributions that do not lead to any distortion of the basic flow. The first system reads as:

$$
\mathbb{L}
\begin{pmatrix}
u_{cc}^I \\
v_{cc}^I \\
d_{cc}^I \\
h_{cc}^I
\end{pmatrix}
=
\begin{pmatrix}
\mathbb{B}_{12}^{cc}(s) \sum_{m=0}^{\infty} \sum_{i=0}^{m} \kappa_{i,m-i}^{12} \cos(M_{cc}^I n) \\
\mathbb{B}_{22}^{cc}(s) \sum_{m=0}^{\infty} \sum_{i=0}^{m} \kappa_{i,m-i}^{22} \sin(M_{cc}^I n) \\
\mathbb{B}_{32}^{cc}(s) \sum_{m=0}^{\infty} \sum_{i=0}^{m} \kappa_{i,m-i}^{32} \cos(M_{cc}^I n) \\
\mathbb{B}_{42}^{cc}(s) \sum_{m=0}^{\infty} \sum_{i=0}^{m} \kappa_{i,m-i}^{42} \cos(M_{cc}^I n)
\end{pmatrix}
\tag{13.27}
$$

The perturbations of the flow field, that satisfy the boundary conditions and the corresponding structure, are expanded as:

$$
u_{cc}^I = \sum_{m=0}^{\infty} \sum_{i=0}^{m} u_{ccm}^I \cos\left(M_{cc}^I n\right)
$$

$$
v_{cc}^I = \sum_{m=0}^{\infty} \sum_{i=0}^{m} v_{ccm}^I \sin\left(M_{cc}^I n\right)
\tag{13.28}
$$

$$
h_{cc}^I = \sum_{m=0}^{\infty} \sum_{i=0}^{m} h_{ccm}^I \cos\left(M_{cc}^I n\right)
$$

$$
d_{cc}^I = \sum_{m=0}^{\infty} \sum_{i=0}^{m} d_{ccm}^I \cos\left(M_{cc}^I n\right)
$$

Substituting the expansions (13.28) into (13.27), we obtain the following system of four ordinary differential equations with constant coefficients:

$$
\left(\frac{d^4}{ds^4} + \sigma_{cc3}^I \frac{d^3}{ds^3} + \sigma_{cc2}^I \frac{d^2}{ds^2} + \sigma_{cc1}^I \frac{d}{ds} + \sigma_{cc0}^I \right) u_{ccm}^I = \overline{\rho}_{ccm}^I + \sum_{i=0}^{6} \overline{\rho}_{ccm_i}^I \mathcal{C}^i
\tag{13.29}
$$

$$
\begin{cases}
v_{ccm}^I = \sum_{i=1}^{4} v_{ccm_i}^I u_{ccm}^{I\ i-1} + \sum_{i=1}^{6} \overline{v}_{ccm_i}^{Ic} \mathcal{C}^{\ i-1} + \overline{v}_{ccm}^I \\
h_{ccm}^I = \sum_{i=1}^{4} h_{ccm_i}^I u_{ccm}^{I\ i-1} + \sum_{i=1}^{6} \overline{h}_{ccm_i}^{Ic} \mathcal{C}^{\ i-1} + \overline{h}_{ccm}^I \\
d_{ccm}^I = \sum_{i=1}^{4} d_{ccm_i}^I u_{ccm}^{I\ i-1} + \sum_{i=1}^{6} \overline{d}_{ccm_i}^{Ic} \mathcal{C}^{\ i-1} + \overline{d}_{ccm}^I
\end{cases}
\tag{13.30}
$$

where the coefficients $(\sigma_{cci}^I, v_{ccm_i}^I, h_{ccm_i}^I, d_{ccm_i}^I)$ are functions of the physical parameters β_u, d_s, τ_{*u}, while the terms $(\overline{\rho}_{ccm_i}^I, \overline{v}_{ccm_i}^{Ic}, \overline{h}_{ccm_i}^{Ic}, \overline{d}_{ccm_i}^{Ic})$, $(\overline{\rho}_{ccm}^I, \overline{v}_{ccm}^I, \overline{h}_{ccm}^I, \overline{d}_{ccm}^I)$ depend also on the longitudinal coordinate s. The general solution

for longitudinal velocity perturbation is found to be:

$$
\begin{aligned}
u_{ccm}^{I} &= \sum_{j=1}^{4} c_{ccm_j}^{I} e^{\lambda_{ccm_j}^{I} s} \\
&+ \sum_{j=1}^{4} g_{cc_j}^{I} \int_{0}^{s} e^{\lambda_{ccm_j}^{I}(s-\xi)} \left[\overline{\rho}_{ccm}^{I}(\xi) + \sum_{i=0}^{6} \overline{\rho}_{ccm_i}^{I}(\xi) \mathcal{C}^{i}(\xi) \right] d\xi
\end{aligned}
\tag{13.31}
$$

where $c_{ccm_j}^{I}$ $(m = 1, \infty)$ are integration constants depending on the channel boundary conditions, while $g_{cc_j}^{I}$ $(j = 1, 4)$ are constant coefficients depending on β_u, d_s, τ_{*u}. Once the solution for u_{ccm}^{I} is known, the remaining dependent variables can be solved in cascade for the mth Fourier mode by employing Equation (13.30).

The second system reads as:

$$
\mathbb{L}
\begin{pmatrix}
u_{cc}^{II} \\
v_{cc}^{II} \\
d_{cc}^{II} \\
h_{cc}^{II}
\end{pmatrix}
=
\begin{pmatrix}
\mathbb{B}_{13}(s) \sum_{m=0}^{\infty} \sum_{i=0}^{m} \kappa_{i,m-i}^{13} \cos(M_{cc}^{II} n) \\
\mathbb{B}_{23}(s) \sum_{m=0}^{\infty} \sum_{i=0}^{m} \kappa_{i,m-i}^{23} \sin(M_{cc}^{II} n) \\
\mathbb{B}_{33}(s) \sum_{m=0}^{\infty} \sum_{i=0}^{m} \kappa_{i,m-i}^{33} \cos(M_{cc}^{II} n) \\
\mathbb{B}_{43}(s) \sum_{m=0}^{\infty} \sum_{i=0}^{m} \kappa_{i,m-i}^{43} \cos(M_{cc}^{II} n)
\end{pmatrix}
\tag{13.32}
$$

where the perturbations of the flow field are expanded as:

$$
\begin{aligned}
u_{cc}^{II} &= \sum_{m=0}^{\infty} \sum_{i=0}^{m} u_{ccm}^{II} \cos\left(M_{cc}^{II} n\right) \\
v_{cc}^{II} &= \sum_{m=0}^{\infty} \sum_{i=0}^{m} v_{ccm}^{II} \sin\left(M_{cc}^{II} n\right) \\
h_{cc}^{II} &= \sum_{m=0}^{\infty} \sum_{i=0}^{m} h_{ccm}^{II} \cos\left(M_{cc}^{II} n\right) \\
d_{cc}^{II} &= \sum_{m=0}^{\infty} \sum_{i=0}^{m} d_{ccm}^{II} \cos\left(M_{cc}^{II} n\right)
\end{aligned}
\tag{13.33}
$$

We can again obtain a system of four ordinary differential equations with constant coefficients similar to (13.29-13.30), with the following general solution

for longitudinal velocity perturbation:

$$
\begin{aligned}
u_{ccm}^{II} = {} & \sum_{j=1}^{4} c_{ccm_j}^{II} e^{\lambda_{ccm_j}^{II} s} \\
& + \sum_{j=1}^{4} g_{cc_j}^{II} \int_0^s e^{\lambda_{ccm_j}^{II}(s-\xi)} \left[\bar{\rho}_{ccm}^{II}(\xi) + \sum_{i=0}^{6} \bar{\rho}_{ccm_i}^{II}(\xi) \mathcal{C}^i(\xi) \right] d\xi
\end{aligned}
\tag{13.34}
$$

In conclusion the solution of the differential problem describing the $\mathcal{O}(\nu^2)$ response of the flow field and the bed configuration due to the forcing induced by channel curvature variations at the second-order, without the distortion effects of the basic flow, reads as:

$$
\begin{cases}
u_{cc} = u_{cc}^{I} + u_{cc}^{II} \\
v_{cc} = v_{cc}^{I} + v_{cc}^{II} \\
h_{cc} = h_{cc}^{I} + h_{cc}^{II} \\
d_{cc} = d_{cc}^{I} + d_{cc}^{II}
\end{cases}
\tag{13.35}
$$

The symmetric structure of the $\mathcal{O}(\nu^2)$ solution for h_{cc} and d_{cc} suggests that mid-channel bars can also develop in nearly equiwidth meanders and, hence, they are not only related to spatial width variations, as observed by Hooke and Yorke [41]. Furthermore, as in the case of periodic meander channels studied by Zolezzi et al. [105], it results that curvature variations can promote laterally symmetrical channel width variations (see Figure 13.1).

13.4 The non-linear response forced by the interaction of channel curvature and width variation $\mathcal{O}(\nu\delta)$

The nonhomogeneous differential problem describing the $\mathcal{O}(\nu\delta)$ response of the flow field and the bed configuration to the forcing induced by the interaction between the channel curvature variations and the channel width variations is obtained, as for the $\mathcal{O}(\nu^2)$ problem, not considering the deviation of the main flow from the channel axis ($C_s = C$). It becomes:

$$\mathbb{L} \begin{pmatrix} u_{cb} \\ v_{cb} \\ d_{cb} \\ h_{cb} \end{pmatrix} = \begin{pmatrix} K_1^{cb}(s,n) \\ K_2^{cb}(s,n) \\ K_3^{cb}(s,n) \\ K_4^{cb}(s,n) \end{pmatrix} \tag{13.36}$$

and the boundary conditions ($n = \pm 1$) read as:

$$v_{cb} = \pm\, \mathcal{B}' u_c;$$
$$\left(F_{ru}^2 h_{cb} - d_{cb}\right)_{,n} = [b_5\mathcal{B} + b_6(u_{b,s} + d_{b,s}) + b_7 u_b + b_8 d_b]\mathcal{C} + \tag{13.37}$$
$$(b_6\mathcal{B} + b_9 u_b + b_{10}d_b)\mathcal{C}'$$

where the b_i ($i = 5, 10$) coefficients are reported in Appendix B.4.

The forcing terms $K_i^{cb}(s,n)$ ($i = 1, 4$) can be expressed as products between $\mathcal{O}(\delta)$ and $\mathcal{O}(\nu)$ terms, $\mathcal{O}(\delta)$ terms related to channel curvature $\mathcal{C}$ and its derivatives and $\mathcal{O}(\nu)$ terms related to width oscillations $\mathcal{B}$ and its derivatives. They are reported in Appendix B.5 and can be divided into five types

of contributions:

$$
\begin{aligned}
K_1^{cb} =& \mathbb{B}_{10}^{cb}(s) + \mathbb{B}_{11}^{cb}(s) \sum_{m=0}^{\infty} \mathbf{k}_m^{11} \sin(M_c n) + \mathbb{B}_{14}^{cb}(s) \sum_{m=1}^{\infty} \mathbf{k}_m^{14} \sin(M_b n) + \\
& \mathbb{B}_{12}^{cb}(s) \sum_{m=1}^{\infty} \sum_{i=1}^{m} \mathbf{k}_{i,m-i+1}^{12} \sin(M_{cb}^{I} n) + \mathbb{B}_{13}^{cb}(s) \sum_{m=1}^{\infty} \sum_{i=1}^{m} \mathbf{k}_{i,m-i+1}^{13} \sin(M_{cb}^{II} n) \\
K_2^{cb} =& \mathbb{B}_{20}^{cb}(s) + \mathbb{B}_{21}^{cb}(s) \sum_{m=0}^{\infty} \mathbf{k}_m^{21} \cos(M_c n) + \mathbb{B}_{24}^{cb}(s) \sum_{m=1}^{\infty} \mathbf{k}_m^{24} \cos(M_b n) + \\
& \mathbb{B}_{22}^{cb}(s) \sum_{m=1}^{\infty} \sum_{i=1}^{m} \mathbf{k}_{i,m-i+1}^{22} \cos(M_{cb}^{I} n) + \mathbb{B}_{23}^{cb}(s) \sum_{m=1}^{\infty} \sum_{i=1}^{m} \mathbf{k}_{i,m-i+1}^{23} \cos(M_{cb}^{II} n) \\
K_3^{cb} =& \mathbb{B}_{30}^{cb}(s) + \mathbb{B}_{31}^{cb}(s) \sum_{m=0}^{\infty} \mathbf{k}_m^{31} \sin(M_c n) + \mathbb{B}_{34}^{cb}(s) \sum_{m=1}^{\infty} \mathbf{k}_m^{34} \sin(M_b n) + \\
& \mathbb{B}_{32}^{cb}(s) \sum_{m=1}^{\infty} \sum_{i=1}^{m} \mathbf{k}_{i,m-i+1}^{32} \sin(M_{cb}^{I} n) + \mathbb{B}_{33}^{cb}(s) \sum_{m=1}^{\infty} \sum_{i=1}^{m} \mathbf{k}_{i,m-i+1}^{33} \sin(M_{cb}^{II} n) \\
K_4^{cb} =& \mathbb{B}_{40}^{cb}(s) + \mathbb{B}_{41}^{cb}(s) \sum_{m=0}^{\infty} \mathbf{k}_m^{41} \sin(M_c n) + \mathbb{B}_{44}^{cb}(s) \sum_{m=1}^{\infty} \mathbf{k}_m^{44} \sin(M_b n) + \\
& \mathbb{B}_{42}^{cb}(s) \sum_{m=1}^{\infty} \sum_{i=1}^{m} \mathbf{k}_{i,m-i+1}^{42} \sin(M_{cb}^{I} n) + \mathbb{B}_{43}^{cb}(s) \sum_{m=1}^{\infty} \sum_{i=1}^{m} \mathbf{k}_{i,m-i+1}^{43} \sin(M_{cb}^{II} n)
\end{aligned}
$$
$$\tag{13.38}$$

where:

$$
M_{cb}^{I} = (4i - 2m - 1)\frac{\pi}{2}; \qquad\qquad M_{cb}^{II} = (2m + 3)\frac{\pi}{2} \tag{13.39}
$$

These terms are characterized by a laterally antisymmetric structure for the longitudinal momentum, the water depth and free surface elevation, while a symmetrical distribution for the lateral momentum [59]. As proceeded for the $\mathcal{O}(\nu^2)$ problem, we consider only the forcing contributions that do not lead to any distortion of the basic flow. The first system reads as:

$$
\mathbb{L}
\begin{pmatrix}
u_{cb}^{I} \\
v_{cb}^{I} \\
d_{cb}^{I} \\
h_{cb}^{I}
\end{pmatrix}
=
\begin{pmatrix}
\mathbb{B}_{12}^{cb}(s) \sum_{m=1}^{\infty} \sum_{i=1}^{m} \mathbf{k}_{i,m-i+1}^{12} \sin(M_{cb}^{I} n) \\
\mathbb{B}_{22}^{cb}(s) \sum_{m=1}^{\infty} \sum_{i=1}^{m} \mathbf{k}_{i,m-i+1}^{22} \cos(M_{cb}^{I} n) \\
\mathbb{B}_{32}^{cb}(s) \sum_{m=1}^{\infty} \sum_{i=1}^{m} \mathbf{k}_{i,m-i+1}^{32} \sin(M_{cb}^{I} n) \\
\mathbb{B}_{42}^{cb}(s) \sum_{m=1}^{\infty} \sum_{i=1}^{m} \mathbf{k}_{i,m-i+1}^{42} \sin(M_{cb}^{I} n)
\end{pmatrix}
\tag{13.40}
$$

The perturbations of the flow field, that satisfy the boundary conditions and the corresponding structure, are expanded as:

$$u_{cb}^I = \sum_{m=1}^{\infty} \sum_{i=1}^{m} u_{cbm}^I \sin\left(M_{cb}^I n\right)$$

$$v_{cb}^I = \sum_{m=1}^{\infty} \sum_{i=1}^{m} v_{cbm}^I \cos\left(M_{cb}^I n\right) \quad\quad (13.41)$$

$$h_{cb}^I = \sum_{m=1}^{\infty} \sum_{i=1}^{m} h_{cbm}^I \sin\left(M_{cb}^I n\right)$$

$$d_{cb}^I = \sum_{m=1}^{\infty} \sum_{i=1}^{m} d_{cbm}^I \sin\left(M_{cb}^I n\right)$$

Introducing the expansions (13.41) into the system (13.40), the following four ordinary differential equations system with constant coefficients is obtained:

$$\left(\frac{d^4}{ds^4} + \sigma_{cb3}^I \frac{d^3}{ds^3} + \sigma_{cb2}^I \frac{d^2}{ds^2} + \sigma_{cb1}^I \frac{d}{ds} + \sigma_{cb0}^I\right) u_{cbm}^I =$$

$$\overline{\rho}_{cbm}^I + \sum_{i=0}^{6} \overline{\rho}_{cbm_i}^{Ic} \mathcal{C}^i + \sum_{i=0}^{6} \overline{\rho}_{cbm_i}^{Ib} \mathcal{B}^i \quad\quad (13.42)$$

$$\begin{cases} v_{cbm}^I = \sum_{i=1}^{4} v_{cbm_i}^I u_{cbm}^I{}^{i-1} + \sum_{i=1}^{6} \overline{v}_{cbm_i}^{Ic} \mathcal{C}^{\,i-1} + \sum_{i=1}^{6} \overline{v}_{cbm_i}^{Ib} \mathcal{B}^{\,i-1} + \overline{v}_{cbm}^I \\ h_{cbm}^I = \sum_{i=1}^{4} h_{cbm_i}^I u_{cbm}^I{}^{i-1} + \sum_{i=1}^{6} \overline{h}_{cbm_i}^{Ic} \mathcal{C}^{\,i-1} + \sum_{i=1}^{6} \overline{h}_{cbm_i}^{Ib} \mathcal{B}^{\,i-1} + \overline{h}_{cbm}^I \\ d_{cbm}^I = \sum_{i=1}^{4} d_{cbm_i}^I u_{cbm}^I{}^{i-1} + \sum_{i=1}^{6} \overline{d}_{cbm_i}^{Ic} \mathcal{C}^{\,i-1} + \sum_{i=1}^{6} \overline{d}_{cbm_i}^{Ib} \mathcal{B}^{\,i-1} + \overline{d}_{cbm}^I \end{cases}$$

$$(13.43)$$

where the coefficients $(\sigma_{cbi}^I, v_{cbm_i}^I, h_{cbm_i}^I, d_{cbm_i}^I)$ and the terms $(\overline{\rho}_{cbm_i}^{Ic}, \overline{v}_{cbm_i}^{Ic}, \overline{h}_{cbm_i}^{Ic}, \overline{d}_{cbm_i}^{Ic})$, $(\overline{\rho}_{cbm_i}^{Ib}, \overline{v}_{cbm_i}^{Ib}, \overline{h}_{cbm_i}^{Ib}, \overline{d}_{cbm_i}^{Ic})$, $(\overline{\rho}_{cbm}^I, \overline{v}_{cbm}^I, \overline{h}_{cbm}^I, \overline{d}_{cbm}^I)$ are functions of the physical parameters β_u, d_s, τ_{*u}. The general solution for longitudinal velocity perturbation is found to be:

$$u_{cbm}^I = \sum_{j=1}^{4} c_{cbm_j}^I e^{\lambda_{cbm_j}^I s} + \sum_{j=1}^{4} g_{cb_j}^I \int_0^s e^{\lambda_{cbm_j}^I (s-\xi)} \left[\overline{\rho}_{cbm}^I(\xi)\right.$$

$$\left. + \sum_{i=0}^{6} \overline{\rho}_{cbm_i}^{Ic}(\xi) \mathcal{C}^i(\xi) + \sum_{i=0}^{6} \overline{\rho}_{cbm_i}^{Ib}(\xi) \mathcal{B}^i(\xi)\right] d\xi \quad\quad (13.44)$$

where $c^I_{cbm_j}$ $(m = 1, \infty)$ are integration constants depending on the channel boundary conditions, instead $g^I_{cb_j}$ $(j = 1, 4)$ are constant coefficients depending on β_u, d_s, τ_{*u}. Once the solution for u^I_{cbm} is known, the remaining dependent variables can be solved in cascade for the mth Fourier mode by employing the expressions in (13.43).

The second system reads as:

$$\mathbb{L}\begin{pmatrix} u^{II}_{cb} \\ v^{II}_{cb} \\ d^{II}_{cb} \\ h^{II}_{cb} \end{pmatrix} = \begin{pmatrix} \mathbb{B}^{cb}_{13}(s) \sum_{m=1}^{\infty} \sum_{i=1}^{m} \mathbf{k}^{13}_{i,m-i+1} \sin(M^{II}_{cb} n) \\ \mathbb{B}^{cb}_{23}(s) \sum_{m=1}^{\infty} \sum_{i=1}^{m} \mathbf{k}^{23}_{i,m-i+1} \cos(M^{II}_{cb} n) \\ \mathbb{B}^{cb}_{33}(s) \sum_{m=1}^{\infty} \sum_{i=1}^{m} \mathbf{k}^{33}_{i,m-i+1} \sin(M^{II}_{cb} n) \\ \mathbb{B}^{cb}_{43}(s) \sum_{m=1}^{\infty} \sum_{i=1}^{m} \mathbf{k}^{43}_{i,m-i+1} \sin(M^{II}_{cb} n) \end{pmatrix} \tag{13.45}$$

where the perturbations of the flow field are expanded as:

$$u^{II}_{cb} = \sum_{m=1}^{\infty} \sum_{i=1}^{m} u^{II}_{cbm} \sin\left(M^{II}_{cb} n\right)$$

$$v^{II}_{cb} = \sum_{m=1}^{\infty} \sum_{i=1}^{m} v^{II}_{cbm} \cos\left(M^{II}_{cb} n\right) \tag{13.46}$$

$$h^{II}_{cb} = \sum_{m=1}^{\infty} \sum_{i=1}^{m} h^{II}_{cbm} \sin\left(M^{II}_{cb} n\right)$$

$$d^{II}_{cb} = \sum_{m=1}^{\infty} \sum_{i=1}^{m} d^{II}_{cbm} \sin\left(M^{II}_{cb} n\right)$$

A system of four ordinary differential equations with constant coefficients similar to (13.42-13.43) can be obtained with the following general solution for longitudinal velocity perturbation:

$$u^{II}_{cbm} = \sum_{j=1}^{4} c^{II}_{cbm_j} e^{\lambda^{II}_{cbm_j} s} + \sum_{j=1}^{4} g^{II}_{cb_j} \int_0^s e^{\lambda^{II}_{cbm_j}(s-\xi)} \left[\overline{\rho}^{II}_{cbm}(\xi) \right.$$

$$\left. + \sum_{i=0}^{6} \overline{\rho}^{IIc}_{cbm_i}(\xi) \mathcal{C}^i(\xi) + \sum_{i=0}^{6} \overline{\rho}^{IIb}_{cbm_i}(\xi) \mathcal{B}^i(\xi) \right] d\xi \tag{13.47}$$

In conclusion the solution of the differential problem describing the $\mathcal{O}(\nu\delta)$ response of the flow field and the bed configuration to the forcing induced

by the interaction between the channel curvature variations and the channel
width variations, without the distortion effects of the basic flow, reads as:

$$\begin{cases} u_{cb} = u_{cb}^{I} + u_{cb}^{II} \\ v_{cc} = v_{cb}^{I} + v_{cb}^{II} \\ h_{cc} = h_{cb}^{I} + h_{cb}^{II} \\ d_{cc} = d_{cb}^{I} + d_{cb}^{II} \end{cases} \tag{13.48}$$

The mixed $\mathcal{O}(\nu\delta)$ solution takes into account the reciprocal effects due
to the presence of channel curvature and width variations. It shows how the
width variations may influence the meander growth and its curvature (see
Figure 13.1).

Chapter 14

Input data and applicability conditions

The mathematical model for the orders $\mathcal{O}(\nu)$ and $\mathcal{O}(\delta)$ was implemented in a MATLAB code by Frascati and Lanzoni [38] and, in this work, it has been improved as described in Chapters 2 and 3. The analytical character of the solution ensures a relatively moderate computational effort. This Chapter illustrates the input data necessary for running the model and discusses the applicability conditions of the model. The input data are:

- the aspect ratio of the channel computed for the reference uniform flow, $\beta_u = B^*_{avg}/D^*_u$;

- the dimensionless sediment grain size, $d_s = d^*_s/D^*_u$;

- the Shields parameter for the reference uniform flow, τ_{*u};

- the particle Reynolds number, R_p.

For the univocally determination of these parameters, it is necessary to know the characteristic sediment grain size (d^*_s); the water discharge conveyed by the river (Q^*); the average longitudinal bed slope of the investigated river reach and the spatial distributions of the channel axis and the river width.

The latters are used to obtain the curvature and width distributions expressed in terms of the longitudinal curvilinear coordinate s. The resulting distributions are smoothed by means of a Savitzky-Golay filter, to avoid any numerical problem in the derivatives evaluation, and remeshed. At this point, the river width and curvature are calculated at every grid point and another low-pass band filter is applied to avoid spurious, high frequency fluctuations in the velocity field. The above described procedures are preliminary to the flow field computation. Eventually, the velocity, the water elevation, the flow depth and the bed elevation are calculated on a two-dimensional curvilinear grid (s_k, n_k). It is worthwhile to underline that the channel width has to be determined with reference to the portion of the cross section where the sediment transport occurs under the formative flow conditions, i.e., controlling the river morphology equilibrium [58].

The condition for the model applicability are:

1. small free vortex effect: this requirement implies wide bends (small $\nu \longrightarrow N^{-1} \simeq 1$) and weakly width variations (small δ);

2. small topographic steering effects: this is ensured when the bends are long enough to not create rapid longitudinal variations of the flow field;

3. small values of the secondary flow intensity due to centrifugally forces: this condition is guaranteed by small values of the dimensionless group $\nu/(\beta_u \sqrt{C_{fu}})$;

4. small amplitude of bed perturbations with respect to the flow depth, in order to ensure the linearization of the problem (see condition 13.1).

14.1 Comparison with field observations: Po river

The model developed in the second part of this thesis has been tested by simulating a reach of the middle Po River (Figure 14.1). The Po River is lo-

Figure 14.1: Planform configuration of the investigated Po river reach; the sections indicated in the picture are those surveyed by the "Agenzia Interregionale per il Fiume Po" (2005). The arrow denotes the flow direction. The image has been taken from Frascati and Lanzoni [38] (source Google maps).

cated in northern Italy. Its length, $652\,km$, makes it the longest river entirely included in the Italian territory. The Po River originates in Monviso mountain and, for the most part, flows in the Pianura Padana floodplain before debouching into the Adriatic Sea through a vast delta with six branches. The Po River morphology presents both single thread meandering/sinuous reaches and multi channel braided reaches. The investigated reach is located between the confluence with the Parma stream and that with the Enza stream. It is about $21\,km$ long, has an average width of $267\,m$ and an average bed slope of 0.02%, estimated from the data of bottom elevations collected in 15 cross sections surveyed by the "Agenzia Interregionale per il Fiume Po" (AIFP) in 2005. The bed river sediments are composed by a mixture of sand and gravel characterized by a geometric mean grain size of $d_{sg}^* = 1.6\,mm$. Since the model does not account for graded sediment and for variations in the flow discharge observed during the flood events, the input values for d_s^* and

Q^*	D_u^*	U_u^*	d_s^*	β_u	d_s	τ_{*u}	R_p
(m^3/s)	(m)	(m/s)	(m)	(-)	(-)	(-)	(-)
1550	4.5	1.3	0.003	29.8	0.0007	0.18	661

Table 14.1: Uniform flow conditions and dimensionless input parameters of the investigated Po river reach.

Q^* have been estimated as described in section 4 of Frascati and Lanzoni [38]. The chosen reach consist of a sinuous point bar river with the width variation intensity $\delta = 0.761$ and the curvature ratio $\nu = 0.125$. The dimensionless group $\nu/(\beta\sqrt{C_{fu}})$ takes the value 0.057 and thus indicates that the investigated river reach is characterized by a wide mildly curved bends. Furthermore, the parameter ϵ is less than 10 ensuring the applicability of a linearized model. Note that the river reach is assumed to be in morphodynamic equilibrium and no external sediments sinks or sources are considered. Table 14.1 summarizes the uniform flow conditions and the dimensionless input parameters necessary for running the numerical code. In the following, the investigated reach is divided into three parts indicated as 1st, 2nd and 3rd sub-reaches.

Figures 14.2, 14.3 and 14.4 show the patterns of the dimensionless value of the vertically averaged longitudinal velocity predicted in these three sub-reaches. It clearly appears that the high-velocity core shifts from one side to the other side of the river at each variation in planform curvature, as a result of the centripetal forces.

The patterns of the corresponding bed topographies results are represented in Figures 14.5, 14.7 and 14.9. They correctly predict the typical meandering bathymetry evolution, with alternating accretion of the sediment deposition ("point bars") and erosion ("pools") at the river banks. Figures 14.6, 14.8 and 14.10 show the comparison between the computed bed elevations and the data surveyed by the "Agenzia Interregionale per il Fiume Po" in 2005, for the aforementioned cross sections (see Figure 14.1). Note

that the bed elevation values shown in the plots are obtained by removing
the perturbations due to the average bed slope. The Figures 14.6, 14.8 and
14.10 reveal an overall good agreement between computed and observed bed
elevations. The model appears to reasonably reproduce the maximum and
minimum bed elevation within the analyzed cross sections and also the alter-
nating transverse bending of the river bed, as observed in Figures 14.5, 14.7
and 14.9 reporting the color maps of the computed bed topography.
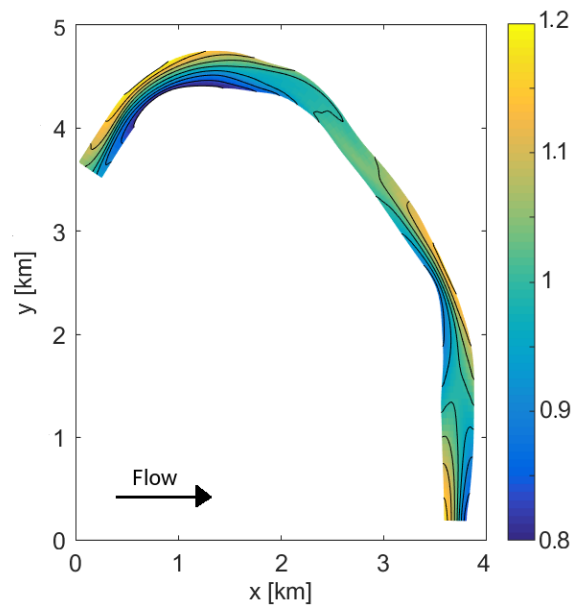
Figure 14.2: Dimensionless value of the vertically averaged longitudinal ve-
locity of the 1st sub-reach. The arrow shows the flow direction.
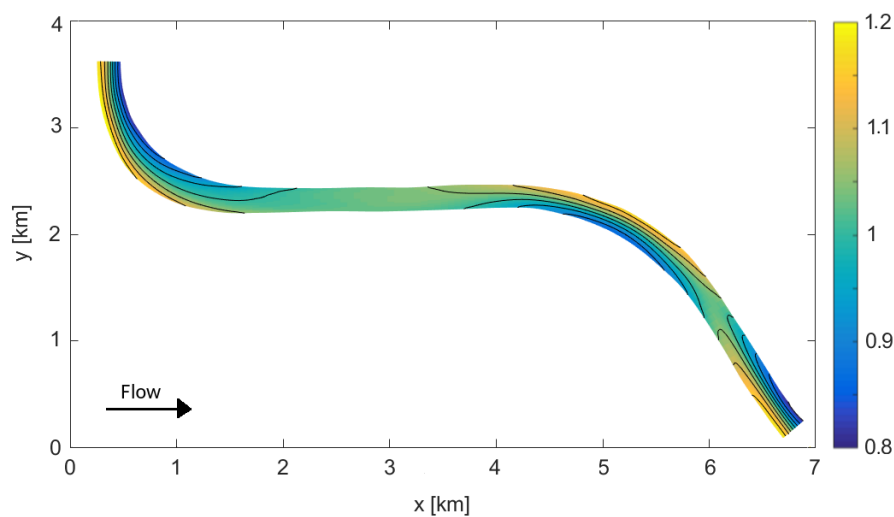
Figure 14.3: Dimensionless value of the vertically averaged longitudinal velocity of the 2nd sub-reach. The arrow shows the flow direction.
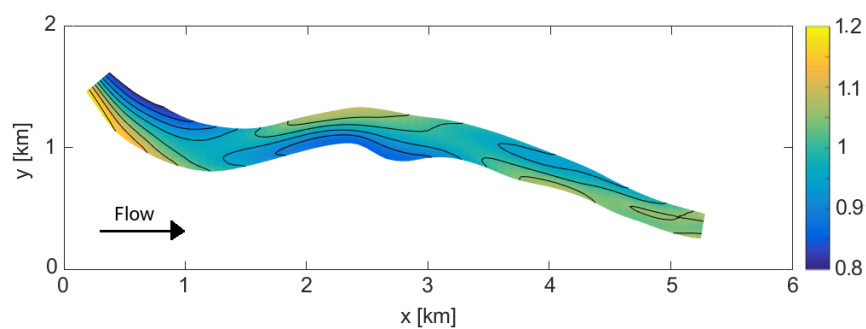
Figure 14.4: Dimensionless value of the vertically averaged longitudinal velocity of the 3rd sub-reach. The arrow shows the flow direction.
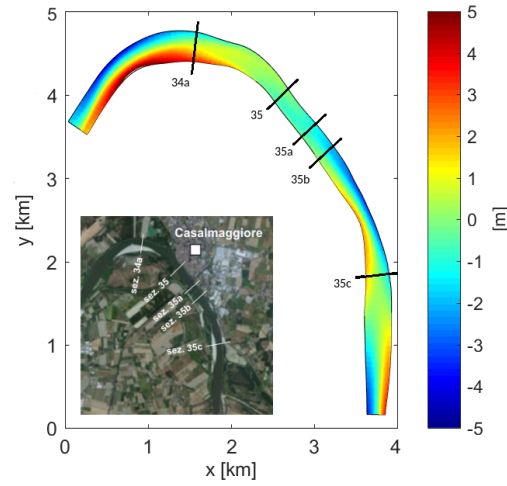
Figure 14.5: Bed topography of the 1st sub-reach and the corresponding aerial photo.
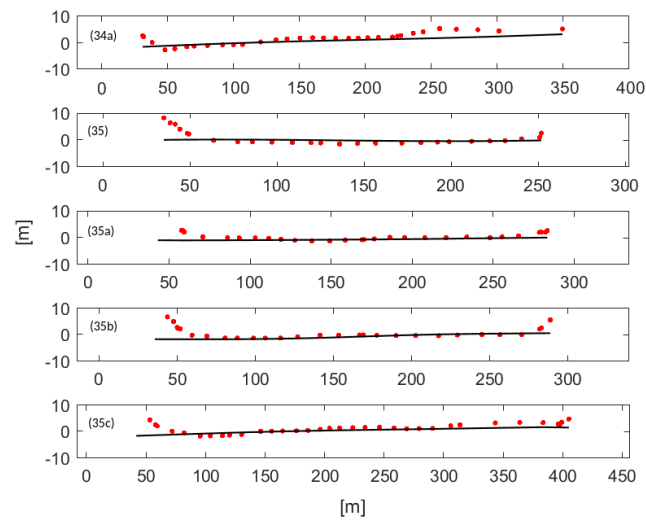
Figure 14.6: Bed elevations of the 1st sub-reach at five cross sections (see Figure 14.5). The continuous line represent the computed values and the red dots are the measures surveyed by the "AIFP". The flow enters into the plot plane.
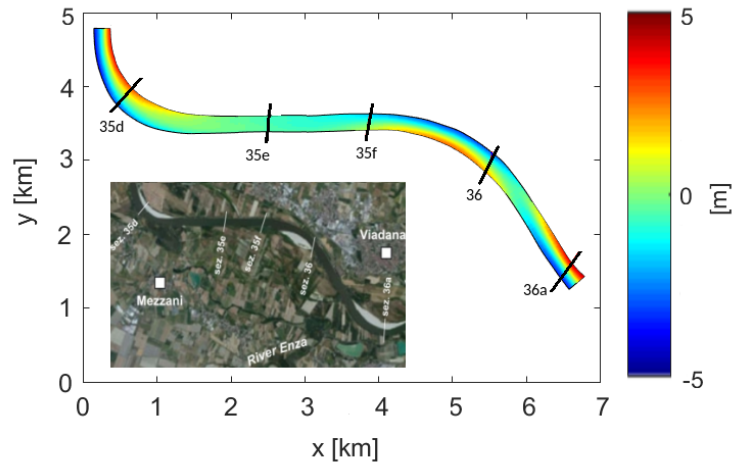
Figure 14.7: Bed topography of the 2nd sub-reach and the corresponding aerial photo.
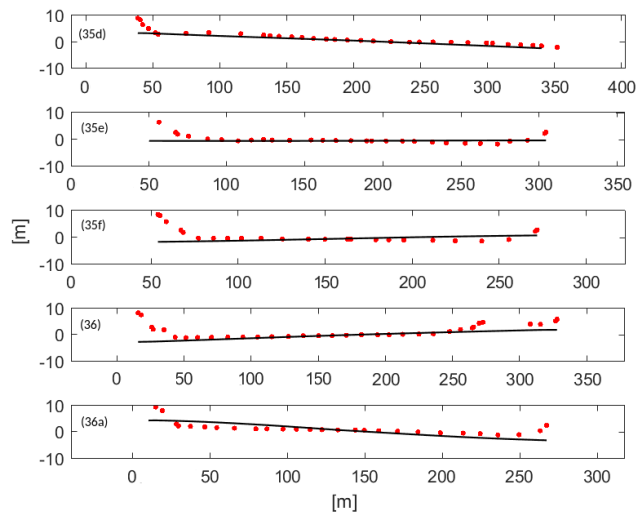
Figure 14.8: Bed elevations of the 2nd sub-reach at five cross sections (see Figure 14.7). The continuous line represent the computed values and the red dots are the measures surveyed by the "AIFP". The flow enters into the plot plane.
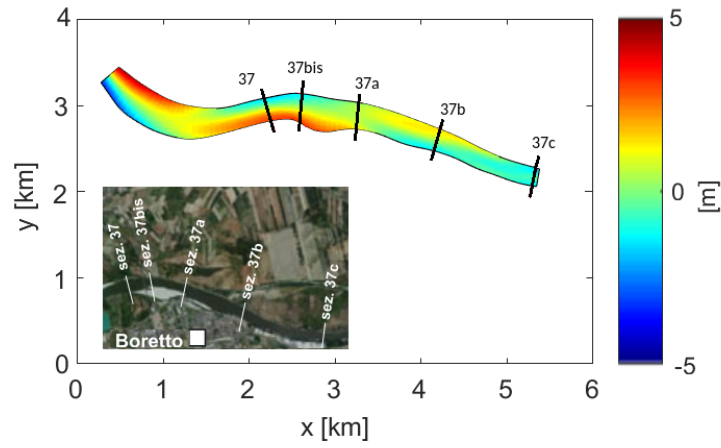
Figure 14.9: Bed topography of the 3rd sub-reach and the corresponding aerial photo.
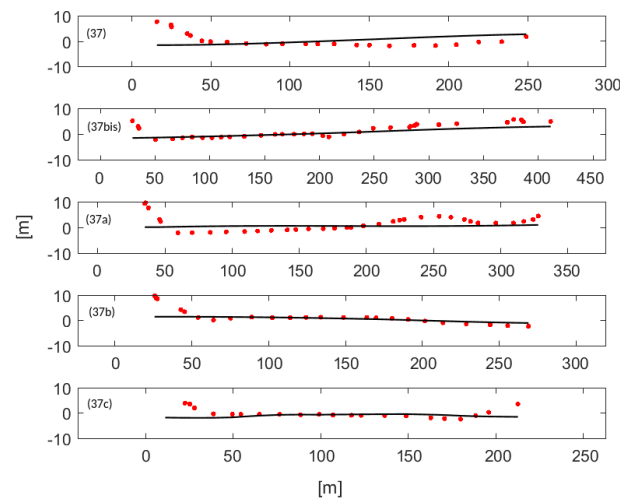
Figure 14.10: Bed elevations of the 3rd sub-reach at five cross sections (see Figure 14.9). The continuous line represent the computed values and the red dots are the measures surveyed by the "AIFP". The flow enters into the plot plane.

Chapter 15

Conclusion

An analytical model based on the complete response of a meandering river to spatially varying distributions of cross-section channel width and channel axis curvature has been developed. The model has been elaborated taking advantage of some morphological features observed in the field. Although alluvial rivers in nature usually exhibit quite complex planforms, they maintain small values of the intensity of width oscillations (δ) and of the dimensionless channel axis curvature (ν). These characteristics allow for linearization of the governing equations (12.29-12.32). Clearly, this approach is unable to describe the behaviour of sharp bends. Another limitation of the model is its incapacity into account for variable hydraulic regime and different grain sizes, that can significantly influence the river morphology. When the aforementioned conditions are not satisfied, the model can only qualitatively predict the morphological tendencies of an alluvial river. It describes the combination of the laterally antisymmetric flow field and bed topography patterns of the $\mathcal{O}(\nu)$ and $\mathcal{O}(\nu\delta)$ solutions and the laterally symmetrical patterns resulting from the $\mathcal{O}(\delta)$ and $\mathcal{O}(\nu^2)$ solutions (see Table 15.1).

The $\mathcal{O}(\nu)$ and $\mathcal{O}(\delta)$ contributions to the flow field are used to assess the morphological behaviour of a reach of the Po River (Italy). The overall comparison between the computed and measured bed elevations is reasonable. A preliminary calibration of the flow discharge Q^* and the characteristic sed-

Order	u,d,h	v
$\mathcal{O}(\delta)$	symmetric	antisymmetric
$\mathcal{O}(\nu)$	antisymmetric	symmetric
$\mathcal{O}(\nu\delta)$	antisymmetric	symmetric
$\mathcal{O}(\nu^2)$	symmetric	antisymmetric

Table 15.1: Character of the flow field variables at different order of approximation.

iment bed size d_s^* parameters is necessary given the intrinsic limitations of the model to find out the formative discharge and to account for the average sedimentologic properties of the investigated reach (see Frascati and Lanzoni [38]). The part two of the present thesis set the mathematical basis needed in order to incorporate in the model also the effects due to the $\mathcal{O}(\nu^2)$ and $\mathcal{O}(\nu\delta)$ corrections. These are hopefully deemed to improve the robustness of the model and, hence, its predictive capacity.

In general, despite the intrinsic limitations due to linearization, the model can be used to investigate the response of the river bed topography as a results of hydrological regime variations or modification of the river planform geometry due to restoration activities or engineering works. Indeed, its analytical character ensures a fast application in the research of the river equilibrium configuration, unlike the complete 2D movable bed models that are extremely time consuming. Moreover, it can be also easily integrated into long-term planimetric evolution models of meandering rivers becoming a powerful tool for controlling floodplain changes over time.

Appendices

Appendix A

Validation of wall layer model
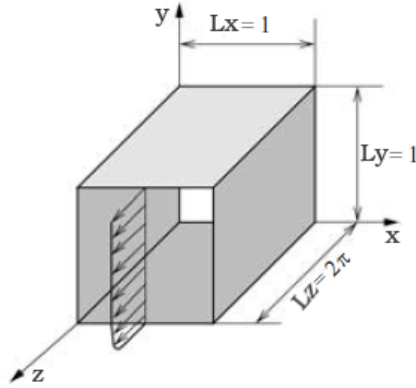
Figure A.1: Sketch of the problem. Figure modified from Broglia et al. [22]

A wall layer model is applied to mimic the solid walls of the meander channel. It supply wall stress as a boundary condition and it is obtained from an instantaneous matching of velocity at the first off-wall centroid with the log law to the computed velocity profile. The work of Broglia et al. [22] has been taken as reference to test the model. They perform LES of a incompressible fully developed turbulent flow in a square duct (see Figure A.1) bounded above by a free-slip wall. The Reynolds number is based on the mean friction velocity u_τ and the duct width D and it is equal to 1000.
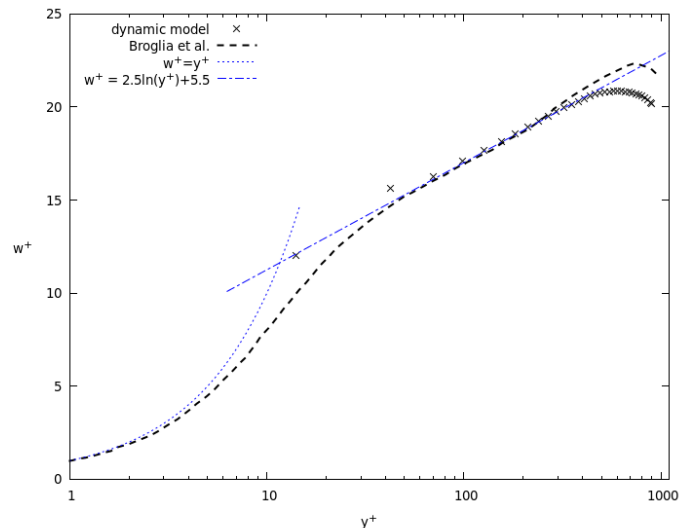
Figure A.2: Mean streamwise-velocity profile in wall units along the bottom-wall bisector ($x = 0.5$).

The flow is driven by a constant body force per unit mass. Periodic boundary conditions are used in the streamwise directions and a wall function approach is employed at the solid walls. The SGS stresses τ_{ij} are parameterized by an eddy viscosity model, where a dynamic procedure is used to determine the eddy viscosity coefficient. The grid dimensions are $32 \times 32 \times 64$ points in spanwise, vertical and streamwise directions (note that we used a grid coarser than that employed by Broglia et al.[22] because of the use of the wall-layer model). In the following, the data for the statistics are collected for a sampling interval of $\Delta t = 5\,s$, corresponding to a non-dimensional time $\Delta t\,u_\tau/D = 5$.

The mean streamwise-velocity profiles in logarithmic scale along the bottom-wall bisector and for a distance of $y = 0.6$ from the free surface are presented in Figures A.2 and A.3, respectively. The velocity profiles and the distances from the wall are normalized using the friction velocity value ($u_\tau = 1$). The logarithmic law is satisfied very well and compared with the Broglia et al.
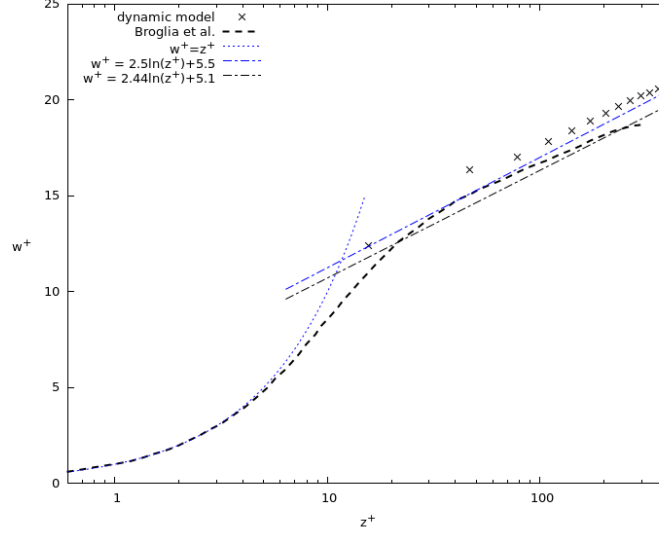
Figure A.3: Mean streamwise-velocity profile in wall units for a distance of $y = 0.6$ from the free surface.

results we do not observe the overshoot of the logarithmic layer intercept in the upper part of the profile. It is worthwhile to observe that the test reference was conducted employing a not uniform grid discretization in the spanwise and normal directions and that a different log law was used for the profile in Figure A.3.

The Figures A.4 and A.5 show mean streamwise-velocity contours and secondary velocity vectors in the cross-stream (y, z)-plane, respectively. The free surface is at the top and only half of the domain is shown. In the lower corner of Figure A.4, a secondary flow, consisting of a streamwise counter-rotating vortex pair, is driven from the central region of the duct towards the corner region along the corner bisector. The flow behavior near the sidewall in the region around $z = 0.5$ shows a transition between the corner and the free-surface behavior, characterized by a weaker counter-clockwise vortical motion. In the upper corner, the effects of the free-shear surface become important with the formation of an "inner" and an "outer" mean secondary

flow.

Contours of the resolved mean streamwise-vorticity (see Figure A.5) show positive and negative extrema at the vertical and horizontal walls. In the center of the larger flow-cells the vorticity attains extreme values locally. We can observe that the contours of mean streamwise vorticity show a direct correspondence with the secondary flow.

In conclusion, the results of this test case are satisfying and they strongly support the wall layer model implemented in the LES-COAST model.
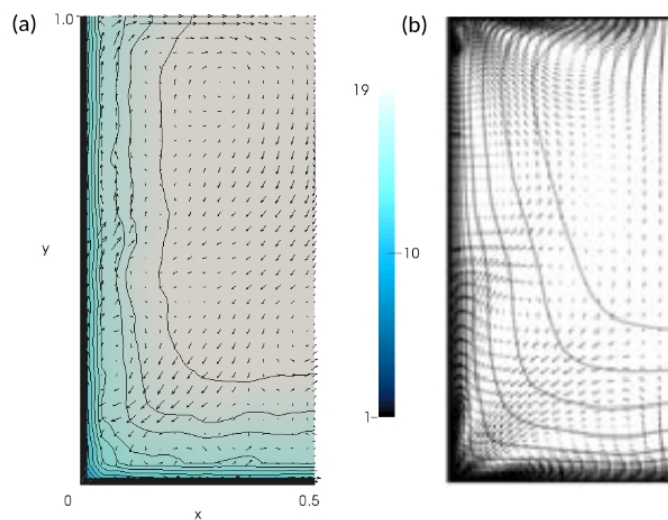
Figure A.4: Mean streamwise-velocity contours and cross-stream velocity vectors in the cross-stream (x,y)-plane: (a) results from the present simulation and (b) Broglia et al. [22] results.
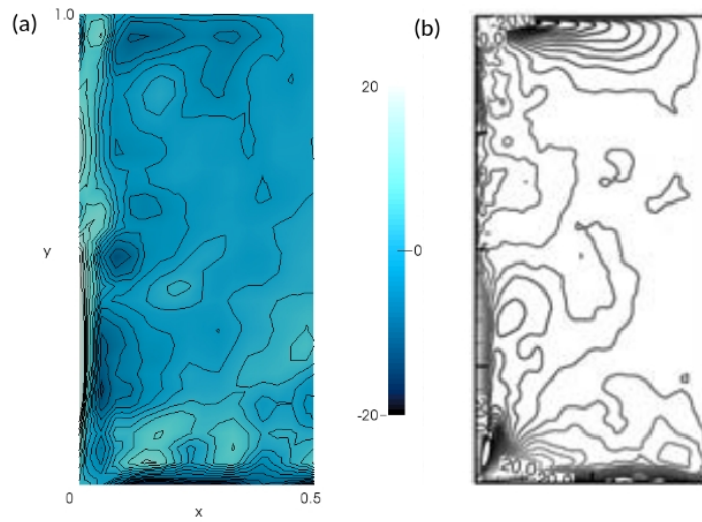
Figure A.5: Mean streamwise-vorticity contours in the cross-stream (x,y)-plane: (a) results from the present simulation and (b) Broglia et al. [22] results.

Appendix B

Mathematical model coefficients

B.1   Coefficients of Equations (12.29-12.32)

$$f_{10} = -n\mathcal{C}\left(\alpha VU_{,n} + \beta_u \frac{\tau_s}{D}\right) - \alpha \mathcal{C} UV - (k_0 \Gamma_{n0} + k_1 \Gamma_{n1})$$

$$f_{01} = n\mathcal{B}_{,s}\left(\alpha UU_{,n} + H_{,n}\right) - \alpha \mathcal{B} VU_{,n}$$

$$f_{11} = \mathcal{B}k_0 \Gamma_{n0} + k_1\left(\mathcal{B}\Gamma_{n1} + \mathcal{B}_{,s}\Gamma_n\right) - n\mathcal{B}\mathcal{C}\beta_u \frac{\tau_s}{D}$$

$$f_{20} = -n\mathcal{C}\left(k_0 \Gamma_{n0} + k_1 \Gamma_{n1}\right) - (k_0 \Gamma_{\nu 0} + k_1 \Gamma_{\nu 1})$$

$$g_{10} = -n\mathcal{C}\left(\alpha VV_{,n} + H_{,n} + \beta_u \frac{\tau_n}{D}\right) + \alpha \mathcal{C} U^2 - k_0\left(\Gamma_0 + \Gamma_{s0}\right) - k_1\left(\Gamma_1 + \Gamma_{s1}\right)$$

$$g_{01} = \alpha n\mathcal{B}_{,s} UV_{,n} + \mathcal{B}\left(\alpha VV_{,n} + H_{,n}\right)$$

$$g_{11} = k_0\left(n\mathcal{B}_{,s}\Gamma_{n0} + \mathcal{B}\Gamma_0\right) + k_1\left(n\mathcal{B}_{,s}\Gamma_{n1} + \mathcal{B}\Gamma_1 + n\Gamma_s + \mathcal{B}_{,s}\Gamma_{01}\right) - n\mathcal{B}\mathcal{C}\beta_u \frac{\tau_n}{D}$$

$$g_{20} = -n\mathcal{C}\left(k_0 \Gamma_0 + k_1 \Gamma_1\right) - \mathcal{C}\left(k_0 \Gamma_2 + k_1 \Gamma_3\right) - (k_4 \Gamma_4 + k_5 \Gamma_5 + k_6 \Gamma_6)$$

$$m_{10} = -\mathcal{C}[n(DV)_{,n} + DV]$$

$$m_{01} = n\mathcal{B}_{,s}(DU)_{,n} - \mathcal{B}(DV),n$$

$$m_{11} = 0$$

$$m_{20} = 0$$

$$n_{10} = -\mathcal{C}(nq_{n,n} + q_n)$$

$$n_{01} = n\mathcal{B}_{,s} q_{s,n} + \mathcal{B}q_{n,n}$$

$$n_{11} = 0$$

$$n_{20} = 0$$

where:

$$\Gamma_{n0} = \frac{[D^2 U^2 \mathcal{C}]_{,n}}{\beta_u \sqrt{C_{fu}} D} \qquad \Gamma_{n1} = \frac{[D^2 U (DU\mathcal{C})_{,s}]_{,n}}{\beta_u^2 C_{fu} D} \qquad \Gamma_n = \frac{[n D^2 U (DU\mathcal{C})_{,n}]_{,n}}{\beta_u^2 C_{fu} D}$$

$$\Gamma_0 = 2 \frac{[D^2 UV\mathcal{C}]_{,n}}{\beta_u \sqrt{C_{fu}} D} \qquad \Gamma_1 = 2 \frac{[D^2 V (DU\mathcal{C})_{,s}]_{,n}}{\beta_u^2 C_{fu} D} \qquad \Gamma_{01} = 2 \frac{[n D^2 V (DU\mathcal{C})_{,n}]_{,n}}{\beta_u^2 C_{fu} D}$$

$$\Gamma_{s0} = \frac{[D^2 U^2 \mathcal{C}]_{,s}}{\beta_u \sqrt{C_{fu}} D} \qquad \Gamma_{s1} = \frac{[D^2 U (DU\mathcal{C})_{,s}]_{,s}}{\beta_u^2 C_{fu} D} \qquad \Gamma_s = \frac{[\mathcal{B}_{,s} D^2 U (DU\mathcal{C})_{,n}]_{,s}}{\beta_u^2 C_{fu} D}$$

$$\Gamma_{\nu0} = 2 \frac{DU^2 \mathcal{C}^2}{\beta_u \sqrt{C_{fu}}} \qquad \Gamma_{\nu1} = 2 \frac{DU\mathcal{C} [DU\mathcal{C}]_{,s}}{\beta_u^2 C_{fu}}$$

$$\Gamma_2 = 2 \frac{DUV\mathcal{C}}{\beta_u \sqrt{C_{fu}}} \qquad \Gamma_3 = 2 \frac{DV [DU\mathcal{C}]_{,s}}{\beta_u^2 C_{fu}}$$

$$\Gamma_4 = \frac{[D^3 U^2 \mathcal{C}^2]_{,n}}{\beta_u^2 C_{fu} D} \qquad \Gamma_5 = 2 \frac{[D^3 U\mathcal{C} (DU\mathcal{C})_{,s}]_{,n}}{\beta_u^3 C_{fu} \sqrt{C_{fu}} D} \qquad \Gamma_6 = \frac{[D^3 (DU\mathcal{C})_{,s}^2]_{,n}}{\beta_u^4 C_{fu}^2 D}$$

B.2 Coefficients of Equations (13.3)

$$C_{f1} = C_{fT} s_1 u_c + (C_{fD} + C_{fT} s_2) d_c$$

$$C_{f2} = C_{fT} s_1 u_b + (C_{fD} + C_{fT} s_2) d_b$$

$$C_{f3} = C_{fT} s_1 u_{cb} + (C_{fD} + C_{fT} s_2) d_{cb} + C_{fT} j_1 u_c u_b + C_{fT} 2 j_2 v_c v_b + C_{fT} j_3 (u_b d_c + u_c d_b)$$

$$C_{f4} = C_{fT} s_1 u_{cc} + (C_{fD} + C_{fT} s_2) d_{cc} + C_{fT} j_4 u_c u_c + C_{fT} j_2 v_c v_c + C_{fT} j_3 u_c d_c$$

$$\tau_{*1} = s_1 u_c + s_2 d_c$$

$$\tau_{*2} = s_1 u_b + s_2 d_b$$

$$\tau_{*3} = s_1 u_{cb} + s_2 d_{cb} + j_1 u_c u_b + 2 j_2 v_c v_b + j_3 (u_b d_c + u_c d_b)$$

$$\tau_{*4} = s_1 u_{cc} + s_2 d_{cc} + j_4 u_c u_c + j_2 v_c v_c + j_3 u_c d_c$$

$$\Phi_1 = s_1 \Phi_T u_c + (\Phi_D + \Phi_T s_2) d_c$$

$$\Phi_2 = s_1 \Phi_T u_b + (\Phi_D + \Phi_T s_2) d_b$$

$$\Phi_3 = s_1 \Phi_T u_{cb} + (\Phi_D + \Phi_T s_2) d_{cb} + \Phi_T j_1 u_c u_b + \Phi_T 2 j_2 v_c v_b + \Phi_T j_3 (u_b d_c + u_c d_b)$$

$$\Phi_4 = s_1 \Phi_T u_{cc} + (\Phi_D + \Phi_T s_2) d_{cc} + \Phi_T j_4 u_c u_c + \Phi_T j_2 v_c v_c + \Phi_T j_3 u_c d_c$$

where:

$$s_1 = \frac{2}{1 - C_{fT}} \qquad\qquad s_2 = \frac{C_{fD}}{1 - C_{fT}} \qquad\qquad s_3 = \frac{C_{fT}}{1 - C_{fT}}$$

$$j_1 = 3 + s_1 + 3s_3 + 4s_1 s_3 \qquad j_2 = (\frac{s_3}{2} + \frac{s_1}{4} + \frac{1}{2}) \qquad j_3 = 2s_2(s_3 + 1)$$

$$j_4 = (4s_3 + \frac{s_1}{2})$$

$$C_{fT} = \tau_{*u} \frac{C_{f,T}|_u}{C_{fu}} \qquad\qquad C_{fD} = \frac{C_{f,D}|_u}{C_{fu}}$$

$$\Phi_T = \tau_{*u} \frac{\Phi_{,T}|_u}{\Phi_u} \qquad\qquad \Phi_D = \frac{\Phi_{,D}|_u}{\Phi_u}$$

B.3 Coefficients of $\mathcal{O}(\delta)$ problem (13.4-13.5) and $\mathcal{O}(\nu)$ problem (13.14-13.15)

$$a_1 = \frac{2\beta_u C_{fu}}{1 - C_{fT}} \qquad a_2 = \beta_u C_{fu}\left(\frac{C_{fD}}{1 - C_{fT}} - 1\right) \qquad a_3 = \beta_u C_{fu}$$

$$a_4 = \frac{2\Phi_T}{1 - C_{fT}} \qquad a_5 = \Phi_D + \frac{C_{fD}\Phi_T}{1 - C_{fT}} \qquad a_6 = \frac{r}{\beta_u\sqrt{\tau_{*u}}}$$

$$a_7 = 1 - k_2\sqrt{C_{fu}} \qquad a_8 = -\frac{k_2}{\beta_u\sqrt{C_{fu}}}$$

$$b_1 = -\beta_u C_{fu} \qquad b_2 = 1 - k_2\sqrt{C_{fu}} \qquad b_3 = -\frac{k_0}{\beta_u\sqrt{C_{fu}}} - \frac{k_3}{\beta_u}$$

$$b_4 = -\frac{k_1}{\beta_u^2 C_{fu}} \qquad b_5 = \frac{k_2\sqrt{\tau_{*u}}}{r\sqrt{C_{fu}}} \qquad b_6 = \frac{k_3\sqrt{\tau_{*u}}}{r\beta_u C_{fu}}$$

B.4   Forcing terms of System (13.22-13.23)

$$
\begin{aligned}
K_1^{cc}(s,n) = & + b_{11}\mathcal{C}\mathcal{C} + 2b_4\mathcal{C}\mathcal{C}' + nb_{12}\mathcal{C}u_c - \mathcal{C}v_c + nb_{13}\mathcal{C}d_c + (b_{11}\mathcal{C} \\
& + 2b_4\mathcal{C}')u_{c,n} + (b_{11}\mathcal{C} + 3b_4\mathcal{C}')d_{c,n} + b_4\mathcal{C}\frac{\partial^2 u_c}{\partial s \partial n} + b_4\mathcal{C}\frac{\partial^2 d_c}{\partial s \partial n} \\
& + b_{14}u_c u_c + b_{15}v_c v_c - b_{13}d_c d_c + b_{16}u_c d_c - u_c u_{c,s} - u_{c,n}v_c \\
K_2^{cc}(s,n) = & + b_{17}\mathcal{C} - nb_{17}\mathcal{C} - nb_{20}\mathcal{C}\mathcal{C}' + [(2b_2 + b_{19})\mathcal{C} + (2b_3 + b_{20})\mathcal{C}' \\
& + 2b_4\mathcal{C}'']u_c + nb_1\mathcal{C}v_c + [b_{21}\mathcal{C} + (b_3 + b_{22})\mathcal{C}' + 2b_4\mathcal{C}'']d_c \\
& + [(b_{11} + b_{20})\mathcal{C} + 3b_4\mathcal{C}']u_{c,s} + [(b_{11} + b_{20})\mathcal{C} + 4b_4\mathcal{C}']d_{c,s} \\
& + (b_{11}\mathcal{C} + 2b_4\mathcal{C}')v_{c,n} - n\mathcal{C}h_{c,n} + b_4\mathcal{C}\frac{\partial^2 u_c}{\partial s^2} + b_4\mathcal{C}\frac{\partial^2 d_c}{\partial s^2} \\
& + b_{23}u_c v_c + b_{24}v_c d_c - u_c v_{c,s} - v_c v_{c,n} \\
K_3^{cc}(s,n) = & - \mathcal{C}v_c - n\mathcal{C}v_{c,n} - u_c d_{c,s} - u_{c,s}d_c - v_c d_{c,n} - v_{c,n}d_c \\
K_4^{cc}(s,n) = & + b_{25}\mathcal{C}\mathcal{C} + b_{26}\mathcal{C}\mathcal{C}' - \mathcal{C}v_c + (b_{27}\mathcal{C} + b_{28}\mathcal{C}')u_{c,n} - n\mathcal{C}v_{c,n} \\
& + [(b_{29} + b_{30})\mathcal{C} + b_{31}\mathcal{C}']d_{c,n} - b_{30}\mathcal{C}F_{ru}^2 h_{c,n} + nb_{30}\mathcal{C}\frac{\partial^2 d_c}{\partial n^2} \\
& - nb_{30}\mathcal{C}F_{ru}^2\frac{\partial^2 h_c}{\partial n^2} + b_{26}\mathcal{C}\frac{\partial^2 u_c}{\partial s \partial n} + b_{26}\mathcal{C}\frac{\partial^2 d_c}{\partial s \partial n} + b_{32}u_c u_{c,s} \\
& + b_{33}v_c v_{c,s} + b_{33}u_{c,n}v_c + b_{33}u_c v_{c,n} + b_{34}u_{c,s}d_c + b_{34}u_c d_{c,s} \\
& + b_{35}v_{c,n}d_c + b_{35}v_c d_{c,n} - b_{36}F_{ru}^2 u_{c,n}h_{c,n} + b_{36}u_{c,n}d_{c,n} \\
& + b_{36}u_c\frac{\partial^2 d_c}{\partial n^2} - b_{36}F_{ru}^2 u_c\frac{\partial^2 h_c}{\partial n^2} + (b_{37} + b_{38})F_{ru}^2 d_{c,n}h_{c,n} \\
& - (b_{37} + b_{38})d_{c,n}d_{c,n} + b_{37}d_c\frac{\partial^2 d_c}{\partial n^2} - b_{37}F_{ru}^2 d_c\frac{\partial^2 h_c}{\partial n^2}
\end{aligned}
$$

where the b_i $(i = 1, 6)$ coefficients are reported in the previous section B.3,

whereas the b_i $(i = 7, 38)$ coefficients read as:

$$b_7 = \frac{k_2\sqrt{\tau_{*u}}}{r\sqrt{C_{fu}}}\left(\frac{1}{1 - C_{fT}}\right)$$

$$b_8 = \frac{k_2\sqrt{\tau_{*u}}}{r\sqrt{C_{fu}}}\left[1 + \frac{C_{fD}}{2(1 - C_{fT})}\right]$$

$$b_9 = \frac{k_3\sqrt{\tau_{*u}}}{r\beta_u C_{fu}}\left(\frac{1}{1 - C_{fT}}\right)$$

$$b_{10} = \frac{k_3\sqrt{\tau_{*u}}}{r\beta_u C_{fu}}\left[2 + \frac{C_{fD}}{2(1 - C_{fT})}\right]$$

$$b_{11} = -\frac{2k_0}{\beta_u\sqrt{C_{fu}}}$$

$$b_{12} = -\beta_u C_{fu}\left(\frac{2}{1 - C_{fT}}\right)$$

$$b_{13} = -\beta_u C_{fu}\left(-1 + \frac{C_{fD}}{1 - C_{fT}}\right)$$

$$b_{14} = -\beta_u C_{fu}\left[\frac{(1 + 2C_{fT})^2}{1 - C_{fT}}\right]$$

$$b_{15} = -\beta_u C_{fu}\left[\frac{1}{2} + \frac{2C_{fT}C_{fD}}{(1 - C_{fT})^2}\right]$$

$$b_{16} = -\beta_u C_{fu}\left(\frac{C_{fT} + 2C_{fD} - 2}{1 - C_{fT}}\right)$$

$$b_{17} = k_2\sqrt{C_{fu}}$$

$$b_{18} = \frac{k_3}{\beta_u}$$

$$b_{19} = -k_2\sqrt{C_{fu}}\left(\frac{2C_{fT}}{1 - C_{fT}}\right)$$

$$b_{20} = -\frac{k_3}{\beta_u}\left(\frac{2C_{fT}}{1 - C_{fT}}\right)$$

$$b_{21} = -k_2\sqrt{C_{fu}}\left(1 + \frac{C_{fD}}{1 - C_{fT}}\right)$$

$$b_{22} = -\frac{k_3}{\beta_u}\left(\frac{C_{fD}}{1 - C_{fT}}\right)$$

$$b_{23} = -\beta_u C_{fu}\left(\frac{1 + C_{fT}}{1 - C_{fT}}\right)$$

$$b_{24} = -\beta_u C_{fu}\left(\frac{C_{fD}}{1 - C_{fT}}\right)$$

$$b_{25} = -\frac{k_2}{\beta_u\sqrt{C_{fu}}}$$

$$b_{26} = -\frac{k_3}{\beta_u^2 C_{fu}}$$

$$b_{27} = -\frac{k_2}{\beta_u\sqrt{C_{fu}}}\left(\frac{2\Phi_T}{1 - C_{fT}}\right)$$

$$b_{28} = -\frac{k_3}{\beta_u^2 C_{fu}}\left(\frac{2\Phi_T}{1 - C_{fT}}\right)$$

$$b_{29} = -\frac{k_2}{\beta_u\sqrt{C_{fu}}}\left(1 + \Phi_D + \frac{\Phi_T C_{fD}}{1 - C_{fT}}\right)$$

$$b_{30} = -\frac{r}{\beta_u\sqrt{\tau_{*u}}}$$

$$b_{31} = \frac{k_3}{\beta_u^2 C_{fu}}\left(2 + \Phi_D + \frac{\Phi_T C_{fD}}{1 - C_{fT}}\right)$$

$$b_{32} = -\frac{2\Phi_T(1 + 4C_{fT})}{1 - C_{fT}}$$

$$b_{33} = -\frac{2\Phi_T + C_{fT} - 1}{1 - C_{fT}}$$

$$b_{34} = -\frac{2\Phi_T C_{fD}}{(1 - C_{fT})^2}$$

$$b_{35} = -\Phi_D - \frac{\Phi_T C_{fD}}{1 - C_{fT}}$$

$$b_{36} = -\frac{r}{\beta_u\sqrt{\tau_{*u}}}\left(\frac{2\Phi_T - 1}{1 - C_{fT}}\right)$$

$$b_{37} = -\frac{r}{\beta_u\sqrt{\tau_{*u}}}\left(\Phi_D - \frac{\Phi_T C_{fD}}{1 - C_{fT}}\right)$$

$$b_{38} = \frac{r}{\beta_u\sqrt{\tau_{*u}}}\left[\frac{C_{fD}}{2(1 - C_{fT})}\right]$$

B.5 Forcing terms of System ([13.36](#)-[13.37](#))

$$
\begin{aligned}
K_1^{cb}(s,n) = & + nb_1\mathcal{B}\mathcal{C} + nb_{12}\mathcal{C}u_b - \mathcal{C}v_b + nb_{13}\mathcal{C}d_b + (b_{11}\mathcal{C} + 2b_4\mathcal{C}')u_{b,n} \\
& + (b_{11}\mathcal{C} + 3b_4\mathcal{C}')d_{b,n} + n\mathcal{B}'u_{c,n} + n\mathcal{B}'h_{c,n} + b_4\mathcal{C}\frac{\partial^2 u_b}{\partial s\partial n} + b_4\mathcal{C}\frac{\partial^2 d_b}{\partial s\partial n} \\
& + b_{39}u_c u_b + b_{23}v_c v_b - 2b_{13}d_c d_b + b_{40}u_c d_b + b_{40}u_b d_c - u_c u_{b,s} \\
& - u_{c,s}u_b - u_{c,n}v_b - u_{b,n}v_c
\end{aligned}
$$

$$
\begin{aligned}
K_2^{cb}(s,n) = & + [(2b_2 + b_{19})\mathcal{C} + (2b_3 + b_{20})\mathcal{C}' + 2b_4\mathcal{C}'']u_b + nb_1\mathcal{C}v_b + [b_{41}\mathcal{C} \\
& + (b_3 + b_{22})\mathcal{C}' + 2b_4\mathcal{C}'']d_b + [(b_{11} - b_{18})\mathcal{C} + 3b_4\mathcal{C}']u_{b,s} + [(b_{11} \\
& - b_{18})\mathcal{C} + 4b_4\mathcal{C}']d_{b,s} + n\mathcal{B}'v_{c,n} + (b_{11}\mathcal{C} + 2b_4\mathcal{C}')v_{b,n} + \mathcal{B}h_{c,n} \\
& - n\mathcal{C}h_{b,n} + b_4\mathcal{C}\frac{\partial^2 u_b}{\partial s^2} + b_4\mathcal{C}\frac{\partial^2 d_b}{\partial s^2} + b_{23}u_c v_b + b_{23}u_b v_c + b_{13}v_c d_b \\
& + b_{13}v_b d_c - u_c v_{b,s} - u_b v_{c,s} - v_c v_{b,n} - v_b v_{c,n}
\end{aligned}
$$

$$
\begin{aligned}
K_3^{cb}(s,n) = & - \mathcal{C}v_b + n\mathcal{B}'u_{c,n} + \mathcal{B}v_{c,n} - n\mathcal{C}v_{b,n} + n\mathcal{B}'d_{c,n} - u_c d_{b,s} - u_{c,s}d_b \\
& - u_b d_{c,s} - u_{b,s}d_c - v_c d_{b,n} - v_{c,n}d_b - v_b d_{c,n} - v_{b,n}d_c
\end{aligned}
$$

$$
\begin{aligned}
K_4^{cb}(s,n) = & - \mathcal{C}v_b + nb_{42}\mathcal{B}'u_{c,n} + (b_{27}\mathcal{C} + b_{28}\mathcal{C}')u_{b,n} + \mathcal{B}v_{c,n} - n\mathcal{C}v_{b,n} \\
& - nb_{35}\mathcal{B}'d_{c,n} + [(b_{29} + b_{30})\mathcal{C} - b_{31}\mathcal{C}']d_{b,n} - b_{30}\mathcal{C}F_{ru}^2 h_{b,n} \\
& - 2b_{30}\mathcal{B}\frac{\partial^2 d_c}{\partial n^2} + nb_{30}\mathcal{C}\frac{\partial^2 d_b}{\partial n^2} + 2b_{30}\mathcal{B}F_{ru}^2\frac{\partial^2 h_c}{\partial n^2} - nb_{30}\mathcal{C}F_{ru}^2\frac{\partial^2 h_b}{\partial n^2} \\
& + b_{26}\mathcal{C}\frac{\partial^2 u_b}{\partial s\partial n} + b_{26}\mathcal{C}\frac{\partial^2 d_b}{\partial s\partial n} + b_{43}u_c u_{b,s} + b_{43}u_{c,s}u_b + b_{33}v_c v_{b,s} \\
& + b_{33}v_{c,s}v_b + b_{33}u_c v_{b,n} + b_{33}u_{c,n}v_b + b_{33}u_b v_{c,n} + b_{33}u_{b,n}v_c \\
& + b_{34}u_c d_{b,s} + b_{34}u_{c,s}d_b + b_{34}u_b d_{c,s} + b_{34}u_{b,s}d_c + b_{35}v_c d_{b,n} \\
& + b_{35}v_{c,n}d_b + b_{35}v_b d_{c,n} + b_{35}v_{b,n}d_c + b_{36}u_{c,n}d_{b,n} + b_{36}u_{b,n}d_{c,n} \\
& - b_{36}F_{ru}^2 u_{c,n}h_{b,n} - b_{36}F_{ru}^2 u_{b,n}h_{c,n} - 2b_{44}d_{c,n}d_{b,n} + b_{44}d_{b,n}h_{c,n} \\
& + b_{36}u_c\frac{\partial^2 d_b}{\partial n^2} + b_{36}u_b\frac{\partial^2 d_c}{\partial n^2} - b_{36}u_c\frac{\partial^2 h_b}{\partial n^2} - b_{36}u_b\frac{\partial^2 h_c}{\partial n^2} \\
& + b_{38}d_c\frac{\partial^2 d_b}{\partial n^2} + b_{38}d_b\frac{\partial^2 d_c}{\partial n^2} - b_{38}F_{ru}^2 d_c\frac{\partial^2 h_b}{\partial n^2} - b_{38}F_{ru}^2 d_b\frac{\partial^2 h_c}{\partial n^2}
\end{aligned}
$$

where the b_i coefficients are reported in section B.3 ($i = 1, 6$) and B.4 ($i =$

7, 38), whereas the b_i coefficients ($i = 39, 44$) read as:

$$b_{39} = -\beta_u C_{fu} \left[\frac{2 + 9C_{fT} - 3C_{fT}^2}{(1 - C_{fT})^2} \right] \quad b_{40} = -\beta_u C_{fu} \left[\frac{2(C_{fT} + C_{fD} - 1)}{(1 - C_{fT})^2} \right]$$

$$b_{41} = -k_2 \sqrt{C_{fu}} \left(\frac{C_{fD}}{1 - C_{fT}} \right) \qquad b_{42} = \frac{2\Phi_T}{1 - C_{fT}}$$

$$b_{43} = -\frac{\Phi_T(5 + 3C_{fT})}{(1 - C_{fT})^2} \qquad\qquad b_{44} = \frac{r}{\beta_u \sqrt{\tau_{*u}}} \left[\Phi_D + C_{fD} \left(\Phi_T - \frac{1}{2} \right) \right]$$

Appendix C

Solution of the linearized form of the problem

C.1 Solution forced by width variations $\mathcal{O}(\delta)$

The solution (13.13) of the four ordinary differential Equation (13.11) is composed by the solution of the corresponding homogeneous differential Equation (I term) and by the particular solution (II term). The homogeneous differential Equation reads as:

$$\lambda_{bm}^4 + \sigma_{b3}\lambda_{bm}^3 + \sigma_{b2}\lambda_{bm}^2 + \sigma_{b1}\lambda_{bm} + \sigma_{b0} = 0$$

where σ_{bi} $(i = 0, 4)$ coefficients are determined as follows:

$$\sigma_{bi} = [\xi_i + \Delta_0\xi_{i+1} + \Delta_2(\alpha_2\,\epsilon_{i+2} - \delta_2\,\beta_{i+2})]/\xi_4 \qquad (\sigma_{b4} = 1)$$

with:

$$\xi_i = \Delta_1(\delta_2\beta_{i+1} - \alpha_2\epsilon_{i+1}) - \delta_2(\delta_2\beta_i - \alpha_2\epsilon_i) + \Delta\epsilon_{i+1}$$

and:

$$\Delta = \delta_2\alpha_1 - \delta_1\alpha_2 \qquad\qquad \Delta_0 = \frac{\delta_2\alpha_0 - \delta_0\alpha_2}{\Delta}$$

$$\Delta_1 = \delta_2\Delta_0 - \delta_1 \qquad\qquad \Delta_2 = \Delta_1\Delta_0 + \delta_0$$

$$\alpha_0 = a_2 \qquad\qquad \alpha_1 = \frac{a_6}{F_{ru}^2 \, \widehat{a}_6} \qquad\qquad \alpha_2 = \frac{1 - \widehat{a}_5}{M_b^2 F_{ru}^2 \, \widehat{a}_6}$$

$$\delta_0 = -M_b^2 a_6 \qquad\qquad \delta_1 = \widehat{a}_5 - 1 - F_{ru}^2 \, \widehat{a}_6 a_3 \qquad \delta_2 = -F_{ru}^2 \, \widehat{a}_6 a_7$$

$$\beta_2 = a_1 \qquad \beta_3 = 1 \qquad \beta_4 = \frac{1 - \widehat{a}_4}{M_b^2 F_{ru}^2 \, \widehat{a}_6} \qquad\qquad \beta_1 = \beta_5 = \beta_6 = 0$$

$$\epsilon_3 = \widehat{a}_4 - 1 - F_{ru}^2 \, \widehat{a}_6 a_3 \qquad \epsilon_4 = -F_{ru}^2 \, \widehat{a}_6 a_7 \qquad\qquad \epsilon_1 = \epsilon_2 = \epsilon_5 = \epsilon_6 = 0$$

Note that:

$$\widehat{a}_4 = a_4 + \frac{a_3 a_8}{a_7} \qquad\qquad \widehat{a}_5 = a_5 + \frac{a_3 a_8}{a_7} \qquad\qquad \widehat{a}_6 = a_6 + \frac{a_8}{F_{ru}^2 a_7}$$

Moreover, the coefficients g_{bjk} $(k = 1, 4)$ appearing in the II term of the solution (13.13) are:

$$g_{bj0} = \frac{W_{mj}}{W_m} \sum_{k=0}^{4} \rho_{bk} \lambda_{bmj}^k \qquad\qquad g_{bjk} = \frac{W_{mj}}{W_m} \sum_{i=k}^{4} \rho_{bi} \lambda_{bmj}^{i-k}$$

where W_m is the Wronskian determinant of the fundamental system and W_{mj} are the Wronskian determinant of the fundamental system with the ith column replaced by $(0, 0, 0, 1)$:

$$W_m = \begin{vmatrix} 1 & 1 & 1 & 1 \\ \lambda_{bm1} & \lambda_{bm2} & \lambda_{bm3} & \lambda_{bm4} \\ \lambda_{bm1}^2 & \lambda_{bm2}^2 & \lambda_{bm3}^2 & \lambda_{bm4}^2 \\ \lambda_{bm1}^3 & \lambda_{bm2}^3 & \lambda_{bm3}^3 & \lambda_{bm4}^3 \end{vmatrix}$$

$$W_{m1} = - \begin{vmatrix} 1 & 1 & 1 \\ \lambda_{bm2} & \lambda_{bm3} & \lambda_{bm4} \\ \lambda_{bm2}^2 & \lambda_{bm3}^2 & \lambda_{bm4}^2 \end{vmatrix} \qquad W_{m2} = \begin{vmatrix} 1 & 1 & 1 \\ \lambda_{bm1} & \lambda_{bm3} & \lambda_{bm4} \\ \lambda_{bm1}^2 & \lambda_{bm3}^2 & \lambda_{bm4}^2 \end{vmatrix}$$

$$W_{m3} = - \begin{vmatrix} 1 & 1 & 1 \\ \lambda_{bm1} & \lambda_{bm2} & \lambda_{bm4} \\ \lambda_{bm1}^2 & \lambda_{bm2}^2 & \lambda_{bm4}^2 \end{vmatrix} \qquad W_{m4} = \begin{vmatrix} 1 & 1 & 1 \\ \lambda_{bm1} & \lambda_{bm2} & \lambda_{bm3} \\ \lambda_{bm1}^2 & \lambda_{bm2}^2 & \lambda_{bm3}^2 \end{vmatrix}$$

The other terms that appear in the coefficients g_{bjk} are defined as follows:

$$\rho_{bi} = [\mu_i + \Delta_0 \mu_{i+1} + \Delta_2 (\alpha_2 \, \eta_{i+2} - \delta_2 \, \gamma_{i+2})]/\xi_4$$

with:

$$\mu_i = \Delta_1(\delta_2\gamma_{i+1} - \alpha_2\eta_{i+1}) - \delta_2(\delta_2\gamma_i - \alpha_2\eta_i) + \Delta\eta_{i+1}$$

and:

$$\eta_4 = -\delta_1\overline{d}_{b1} \qquad \eta_5 = -\delta_2\overline{d}_{b1} - \delta_1\overline{d}_{b2}$$

$$\eta_6 = -\delta_2\overline{d}_{b2} \qquad \eta_1 = \eta_2 = \eta_3 = 0$$

$$\gamma_3 = -a_2\overline{d}_{b1} \qquad \gamma_4 = -\overline{h}_{b1} - a_2\overline{d}_{b2} \qquad \gamma_5 = -\overline{h}_{b2} - \alpha_2\overline{d}_{b1}$$

$$\gamma_6 = -\alpha_2\overline{d}_{b2} \qquad \gamma_1 = \gamma_2 = 0$$

Note that:

$$\overline{h}_{b1} = -\frac{a_3}{2} \qquad\qquad \overline{h}_{b2} = -\frac{a_7}{2}$$

$$\overline{d}_{b1} = -\frac{a_3}{2}F_{ru}^2 \qquad\qquad \overline{d}_{b2} = -\frac{a_7}{2}F_{ru}^2 - \frac{a_8}{2a_6}$$

Once the coefficients of the perturbed solution for the longitudinal velocity have been determined, the coefficients of the other perturbed variables are readily determined from the relations (13.12), in which appear the terms:

$$d_{bmi} = -\frac{\xi_i}{\Delta\,\Delta_2} \qquad\qquad d_{bmi}^b = \frac{\mu_i}{\Delta\,\Delta_2}$$

$$v_{bm1} = V_{bm1}/M_b \quad v_{bm2} = (V_{bm2} - 1)/M_b \quad v_{bm3} = V_{bm3}/M_b \quad v_{bm4} = V_{bm4}/M_b$$

$$v_{bm2}^b = V_{bm2}^b/M_b \quad v_{bm3}^b = (V_{bm3}^b - \overline{d}_{1b})/M_b \quad v_{bm4}^b = (V_{bm4}^b - \overline{d}_{2b})/M_b$$

$$h_{bm1} = H_{bm1} \qquad h_{bm2} = H_{bm2} + \beta_4 \qquad h_{bm3} = H_{bm3} \qquad h_{bm4} = H_{bm4}$$

$$h_{bm2}^b = H_{bm2}^b \qquad h_{bm3}^b = H_{bm3}^b + \alpha_2\,\overline{d}_{1b} \qquad h_{bm4}^b = H_{bm4} + \alpha_2\,\overline{d}_{2b}$$

where:

$$V_{bmi} = \Delta_0 d_{bmi} + \frac{\delta_2\,\beta_{i+1} - \alpha_2\,\epsilon_{i+1}}{\Delta}$$

$$V_{bmi}^b = \Delta_0 d_{bmi}^b + \frac{\alpha_2\,\eta_{i+1} - \delta_2\,\gamma_{i+1}}{\Delta}$$

$$H_{bmi} = (\alpha_1 - \Delta_0\,\alpha_2)d_{bmi} - \alpha_2\frac{\delta_2\,\beta_{i+1} - \alpha_2\,\epsilon_{i+1}}{\Delta}$$

$$H_{bmi}^b = (\alpha_1 - \Delta_0\,\alpha_2)d_{bmi}^b - \alpha_2\frac{\alpha_2\,\eta_{i+1} - \delta_2\,\gamma_{i+1}}{\Delta}$$

C.2   Solution forced by channel curvature $\mathcal{O}(\nu)$

The solution (13.21) of the four ordinary differential Equation (13.19) is composed by the solution of the corresponding homogeneous differential Equation (I term) and by the particular solution (II term). The homogeneous differential Equation reads as:

$$\lambda_{cm}^4 + \sigma_{c3}\lambda_{cm}^3 + \sigma_{c2}\lambda_{cm}^2 + \sigma_{c1}\lambda_{cm} + \sigma_{c0} = 0$$

where σ_{ci} $(i = 0, 4)$ coefficients are determined as follows:

$$\sigma_{ci} = (\xi_i + \Delta_0\xi_{i+1} + \Delta\Delta_2 T_{i+1})/\xi_4 \qquad (\sigma_{c4} = 1)$$

with:

$$\xi_i = -\Delta\Delta_1 T_i + \delta_2\Delta T_{i-1} + \Delta\epsilon_{i+1}$$

and:

$$\Delta = \delta_2\alpha_1 - \delta_1\alpha_2 \qquad\qquad \Delta_0 = \frac{\delta_2\alpha_0 - \delta_0\alpha_2}{\Delta}$$

$$\Delta_1 = \delta_2\Delta_0 - \delta_1 \qquad\qquad \Delta_2 = \Delta_1\Delta_0 + \delta_0$$

$$T_0 = -\Delta_0 \qquad\qquad T_i = -\frac{1}{\Delta}(\delta_2\beta_{i+1} - \alpha_2\epsilon_{i+1})$$

$$\alpha_0 = a_2 \qquad\qquad \alpha_1 = \frac{a_6}{F_{ru}^2\widehat{a}_6} \qquad\qquad \alpha_2 = \frac{1 - \widehat{a}_5}{M_c^2 F_{ru}^2\widehat{a}_6}$$

$$\delta_0 = -M_c^2 a_6 \qquad\qquad \delta_1 = \widehat{a}_5 - 1 - F_{ru}^2\widehat{a}_6 a_3 \qquad \delta_2 = -F_{ru}^2\widehat{a}_6 a_7$$

$$\beta_2 = a_1 \qquad \beta_3 = 1 \qquad \beta_4 = \frac{1 - \widehat{a}_4}{M_c^2 F_{ru}^2\widehat{a}_6} \qquad\qquad \beta_1 = \beta_5 = \beta_6 = 0$$

$$\epsilon_3 = \widehat{a}_4 - 1 - F_{ru}^2\widehat{a}_6 a_3 \qquad \epsilon_4 = -F_{ru}^2\widehat{a}_6 a_7 \qquad\qquad \epsilon_1 = \epsilon_2 = \epsilon_5 = \epsilon_6 = 0$$

Note that:

$$\widehat{a}_4 = a_4 + \frac{a_3 a_8}{a_7} \qquad\qquad \widehat{a}_5 = a_5 + \frac{a_3 a_8}{a_7} \qquad\qquad \widehat{a}_6 = a_6 + \frac{a_8}{F_{ru}^2 a_7}$$

The coefficients g_{cjk} $(k = 1, 4)$ appearing in the expression of the longitudinal velocity perturbation (13.13) are formally similar to those derived for the

problem forced by width variations (g_{bjk}), but with the coefficients ρ_{ci} that take the form:

$$\rho_{ci} = (\mu_i + \Delta_0\mu_{i+1} - \Delta\Delta_2 T_{i+1}^c)/\xi_4$$

where:

$$\mu_i = \Delta\Delta_1 - \delta_2\Delta T_{i-1}^c + \Delta\eta_{i+1}$$

with:

$$T_i^c = \frac{1}{\Delta}(\delta_2\gamma_{i+1} - \alpha_2\eta_{i+1})$$

and:

$$\eta_3 = -\delta_1\overline{d}_{c1} \qquad \eta_4 = -\delta_2\overline{d}_{c1} - \delta_1\overline{d}_{c2} \quad \eta_5 = -\delta_2\overline{d}_{c2} - \delta_1\overline{d}_{c3}$$

$$\eta_6 = -\delta_2\overline{d}_{c3} \qquad \eta_1 = \eta_2 = 0$$

$$\gamma_2 = b_1 - a_2\overline{d}_{c1} \qquad \gamma_3 = -\overline{h}_{c1} - a_2\overline{d}_{c2} \qquad \gamma_4 = -\overline{h}_{c2} - a_2\overline{d}_{c3} - \alpha_2\overline{d}_{c1}$$

$$\gamma_5 = -\overline{h}_{c3} - \alpha_2\overline{d}_{c2} \quad \gamma_6 = -\alpha_2\overline{d}_{c3} \qquad \gamma_1 = 0$$

Once the coefficient of the perturbation of the longitudinal velocity has been determined, the coefficient of the other perturbed variables are readily determined from the relations (13.20), in which appear the terms:

$$v_{cmi} = (V_{ci} + T_{c0}d_{cmi})/M_c \qquad v_{cmi}^c = (V_{ci}^c + T_{c0}d_{cmi}^c)/M_c$$

$$h_{cmi} = H_{ci} + H_{c0}d_{cmi} \qquad h_{cmi}^c = H_{ci}^c + H_{c0}d_{cmi}^c$$

with:

$$d_{cm0} = -(M_c^2 H_{c0} + a_7 T_0^2 + a_3 T_0)$$

$$d_{cm1} = (M_c^2 H_{c1} + a_7 T_0 T_1 + a_3 V_{c1})/d_{cm0}$$

$$d_{cm2} = (M_c^2 H_{c2} + a_7 T_0 T_2 + a_3 V_{c2} + a_7 V_{c1})/d_{cm0}$$

$$d_{cm3} = (M_c^2 H_{c3} + a_7 T_0 T_3 + a_3 V_{c3} + a_7 V_{c2})/d_{cm0}$$

$$d_{cm4} = (a_7 V_{c3})/d_{cm0}$$

$$d_{cm1}^c = (M_c^2 H_{c1}^c + a_7 T_0 T_1^c + a_3 V_{c1}^c)/d_{cm0}$$

$$d_{cm2}^c = (M_c^2 H_{c2}^c + a_7 T_0 T_2^c + a_3 V_{c2}^c + V_{c1}^c)/d_{cm0}$$

$$d_{cm3}^c = (M_c^2 H_{c3}^c + a_7 T_0 T_3^c + a_3 V_{c3}^c + V_{c2}^c)/d_{cm0}$$

$$d_{cm4}^c = (M_c^2 H_{c4}^c + a_7 T_0 T_4^c + a_3 V_{c4}^c + V_{c3}^c)/d_{cm0}$$

$$d_{cm5}^c = (a_7 V_{c4}^c)/d_{cm0}$$

where:

$$V_{c1} = T_1 \qquad\qquad V_{c2} = T_2 + 1 \qquad\qquad V_{c3} = T_3$$

$$V_{c1}^c = T_1^c \qquad\qquad V_{c2}^c = T_2^c + \overline{d}_{c1} \qquad V_{c3}^c = T_3^c + \overline{d}_{c2}$$

$$V_{c4}^c = T_4^c + \overline{d}_{c3} \qquad V_{c5}^c = 0$$

$$H_{c0} = \alpha_1 + \alpha_2 T_0 \qquad H_{c1} = \alpha_2 T_1$$

$$H_{c2} = \alpha_2 T_2 + \beta_4 \qquad H_{c3} = \alpha_2 T_3$$

$$H_{c1}^c = \alpha_2 T_1^c \qquad\qquad H_{c2}^c = \alpha_2 (T_2^c + \overline{d}_{c1})$$

$$H_{c3}^c = \alpha_2 (T_3^c + \overline{d}_{c2}) \quad H_{c4}^c = \alpha_2 (T_4^c + \overline{d}_{c3}) \quad H_{c5}^c = 0$$

List of Symbols

a_i	$(i = 0, 1)$ constant coefficients
a_1	structure parameter
a_i	$(i = 1, 8)$ constant coefficients in Part II
a_N	matrix coefficient corresponding to the neighbour N
a_P	central coefficient
B	channel width in Part I
B, B_{avg}, B_0	local, average and maximum half channel width
$\mathcal{B}$	dimensionless width perturbation
b_i	$(i = 1, 10)$ constant coefficients
C_d	constant of the dynamic eddy viscosity model
C_{DES}	model parameter
C_f, C_{fu}	local and uniform flow friction coefficient
C_{fi}	$(i = 1, 4)$ constant coefficients
C_i	convective terms
$\mathcal{C}$	curvature of the channel axis
$\mathcal{C}_s$	curvature of the streamlines
c_{bmj}, c_{cmj}	integration constants
c_f	friction factor
D	flow field domain in Part I
D, D_u	local and uniform flow depth
D_E, D_I	discrete operator representing the off-diagonal diffusive terms and the diagonal viscous terms, respectively
d	turbulence length scale

d_{50}	sediment diameter intercepted for 50% of the cumulative mass
d_{min}	distance to the closest boundary
d_{sg}	geometric mean grain size
d_s	sediment grain size
F	face flux
F_r, F_{ru}	Froude number based on the bulk velocity and Froude number of the uniform flow
$\mathcal{F}$	vertical distribution of the uniform flow with local flow characteristics
f	flow field variable, point in the centre of the face
f_{ij}	constant coefficients
G	filter function
G^{mn}	mesh skewness tensor
$\mathcal{G}_i$	vertical structure of the secondary flow due to channel axis curvature ($i = 0$) and longitudinal convection ($i = 1$)
$\mathbf{G}$	dimensionless second order 2-D tensor
g	gravitational constant
g_{ij}	constant coefficients
g_{bjk}, g_{cjk}	constant coefficients
H	average water depth in Part I
H, H_r	local and reference water surface elevation with respect to a given horizontal datum in Part II
h	local water surface elevation with respect to the horizontal plane containing n
$\tilde{h}$	free surface perturbation
I	identity matrix
J^{-1}	inverse of Jacobian of the coordinate transformation or cell volume
K_i^{cb}, K_i^{cc}	($i = 1, 4$) forcing terms
k	von Karman constant

k_i	redistribution coefficients due to centrifugal ($i = 0, 2$) and convective ($i = 1, 3$) secondary flow effects or due to non-linear interactions ($i = 4, 6$) between secondary and longitudinal flow
k_s	equivalent roughness height
L	length of the investigated river reach
L_{ij}	resolved turbulent stresses
$\mathcal{L}, \mathbb{L}$	differential operators
m_{ij}	constant coefficients
N	longitudinal metric coefficient
$\mathcal{N}$	vertical distribution of the eddy viscosity
n_{ij}	constant coefficients
$\mathbf{n}_b$	unit vector normal to the banks
p	kinematic pressure
Q	flow rate
q_s, q_n	longitudinal and lateral components of the unit width sediment flux, $\mathbf{q}$
R	centreline radius of curvature in Part I and local radius of curvature of the channel axis in Part II
R_0	typical value of the radius of curvature
R_i	discrete operator for pressure gradient terms
R_p	particle Reynolds number
Re	Reynolds number
r	empirical constant
$\mathbf{r}$	source term
S	magnitude of the vorticity
$\overline{S}_{ij}$	resolved strain rate tensor
s, n, z	intrinsic longitudinal, lateral and vertical coordinate in Part II, respectively
$\mathbf{s}_f$	face area vector
T_{ij}	subtest scale stresses

t	time
U_m	volume flux
U, V	local values of depth-averaged longitudinal and transverse velocities in Part II, respectively
u_i^*	intermediate velocity
u_τ	average shear velocity
u, v, w	longitudinal, lateral and vertical components of the local velocity in Part II, respectively
u_b, v_b, d_b, h_b	flow field perturbations due to width variations
u_c, v_c, d_c, h_c	flow field perturbations due to channel axis curvature
$u_{cb}, v_{cb}, d_{cb}, h_{cb}$	flow field perturbations due to channel axis curvature and width variations interaction
$u_{cc}, v_{cc}, d_{cc}, h_{cc}$	flow field perturbations due to channel axis curvature at second-order
u_s, v, w_s	spanwise, vertical and streamwise velocity in Part I, respectively
$\mathbf{u}$	velocity vector
v_n^+	wall-normal velocity dimensionless with u_τ
$\tilde{v}$	local distribution of the centrifugally induced secondary flow
W_{av}	bulk velocity
w_*	friction velocity
x	arbitrarily selected reference Cartesian axis in Part II
x, y, z	lateral, vertical and longitudinal space coordinates in Part I, respectively
z_0	reference level at which the no slip condition is applied
z_n^+	wall-normal coordinate dimensionless with ν/u_τ (wall units)
α	momentum correction factor
β_u	aspect ratio of the uniform flow
$\overline{\Delta}$	filter width

Δ	local grid size
$\Delta x, \Delta y, \Delta z$	grid size in x, y and z directions, respectively
δ	intensity of longitudinal width variations
δ	Kronecker Delta
ϵ	controlling parameter of bottom variation intensity
η	local bed elevation
θ	angle between the channel axis and the x-direction
$\lambda_{bm_j}, \lambda_{cm_j}$	characteristic exponents
$\lambda_{cbm_j}, \lambda_{ccm_j}$	characteristic exponents
ν	kinematic viscosity in Part I and curvature ratio in Part II
ν_T	turbulent eddy viscosity
ξ, η, ζ	curvilinear coordinate in Part I
ξ	normalized vertical coordinate
ξ_0	normalized reference level
ρ, ρ_s	water and sediment density, respectively
ρ_0	reference density
ρ_{bi}, ρ_{ci}	constant coefficients
$\overline{\rho}_{cbm}, \overline{\rho}_{ccm}$	functions of the longitudinal coordinate s
$\overline{\rho}_{cbm_i}, \overline{\rho}_{ccm_i}$	functions of the longitudinal coordinate s
σ_1, σ_2	principal stresses
$\sigma_{bi}, \sigma_{ci}, \sigma_{cbi}, \sigma_{cci}$	constant coefficients
τ_{ij}	subgrid-scale stresses
τ_*, τ_{*u}	local and uniform flow Shields stress
τ_{*i}	$(i = 1, 4)$ constant coefficients
τ_{bs}	total bed shear stresses
τ_s, τ_n	longitudinal and transverse components of the bed shear stress, τ
υ	molecular viscosity
$\tilde{\upsilon}$	modified eddy viscosity
Φ, Φ_u	local and uniform flow intensity of sediment transport
Φ_i	$(i = 1, 4)$ constant coefficients

ϕ	projector pressure operator
ω_y	vertical vorticity
ω_s	streamwise vorticity

Bibliography

[1] ARMENIO, V., AND PIOMELLI, U., 2000. *A Lagrangian Mixed Subgrid-Scale Model in generalized coordinates*, Flow, Turbulence and Combustion, 65, 51-81.

[2] BAGNOLD, R. A., 1960. *Some aspects of the shape of river meanders*, US Geological Survey Professional Paper, 282-E, US Geological Survey, Washington, DC.

[3] BATHURST, J. C., THORNE, C. R., AND HEY, R. D., 1977. *Direct measurements of secondary currents in river bends*, Nature, 269, 504-506.

[4] BATHURST, J. C., THORNE, C. R., AND HEY, R. D., 1979. *Secondary flow and shear stress at river bends*, J. Hydraulics Division, ASCE, 105, 1277-1295.

[5] BLANCKAERT, K., 2001. *Discussion on: Bend-flow simulation using 2D depth-averaged model, by H. C. Lien et al.*, J. Hydraul. Eng., Am. Soc. Civ. Eng., 127(2), 167-170.

[6] BLANCKAERT, K., 2009. *Saturation of curvature-induced secondary flow, energy losses, and turbulence in sharp open-channel bends: Laboratory experiments, analysis, and modelling*, J. Geophys. Res., 114, F03015.

[7] BLANCKAERT, K., 2010. *Topographic steering, flow recirculation, velocity redistribution and bed topography in sharp meander bends*, Water Resour. Res., 46, W09506.

[8] BLANCKAERT, K., 2011. *Hydrodynamic processes in sharp meander bends and their morphological implications*, J. Geophys. Res., 116.

[9] BLANCKAERT, K., 2015. *Flow separation at convex banks in open channels*, J. Fluid Mech., 779, 432-467.

[10] BLANCKAERT, K., AND DE VRIEND, H. J., 2003. *Non-linear modeling of mean flow redistribution in curved open channels*, Water Resour. Res., 39(12), 1375.

[11] BLANCKAERT, K., AND DE VRIEND, H. J., 2004. *Secondary flow in sharp open-channel bends*, J. Fluid Mech., 498, 353-380.

[12] BLANCKAERT, K., AND DE VRIEND, H. J., 2005. *Turbulence characteristics in sharp open-channel bends*, Phys. Fluids, AIP, 17(5), 055102.

[13] BLANCKAERT, K., AND DE VRIEND, H. J., 2005. *Turbulence structure in sharp open-channel bends*, J. Fluid Mech., 536, 27-48.

[14] BLANCKAERT, K., AND GRAF, W. H., 2001. *Experiments on flow in an open-channel bend: Mean flow and turbulence*, J. Hydraul. Eng., 127(10), 835-847.

[15] BLANCKAERT, K., AND GRAF, W. H., 2004. *Momentum transport in sharp open-channel bends*, J. Hydraul. Eng., Am. Soc. Civ. Eng., 130(3), 186-198.

[16] BLONDEAUX, P., AND SEMINARA, G., 1985. *A unified bar-bend theory of river meanders*, J. Fluid Mech., 157, 449-470.

[17] BLONDEAUX, P., COLOMBINI, M., SEMINARA, G. AND VITTORI G., 2018. *Introduction to Morphodynamics of Sedimentary Patterns*,

Morphodynamics of Sedimentary Patterns, GENOVA UNIVERSITY PRESS.

[18] BOLLA PITTALUGA, M., NOBILE, G., AND SEMINARA, G., 2009. *A nonlinear model for river meandering*, Water Resour. Res., 45, W04432.

[19] BOOIJ, R., 2003. *Measurements and large eddy simulations of the flows in some curved flumes*, J. Turbul., 4, 8.

[20] BRESSAN, F., BALLIO, F., AND ARMENIO, V., 2011. *Turbulence around a scoured bridge abutment*, J. Turbul., 12, 3.

[21] BRICE, J. C., 1975. *Air photo interpretation of the form and behavior of alluvial rivers*, Final Report to the U.S. Army Research Office, Durham, 10, Washington Univ., St Louis, Mo.

[22] BROGLIA, R., PASCARELLI, A., AND PIOMELLI, U., 2003. *Large-eddy simulations of ducts with a free surface*, J. Fluid Mech., 484, 223.

[23] CALHOUN, R. J., AND STREET, R. L., 2001. *Turbulent flow over a wavy surface: Neutral case*, J. Geophys. Res., Oceans, 106, 9277.

[24] CAMPOREALE, C., PERONA, P., PORPORATO, A., AND RIDOLFI, L., 2007. *Hierarchy of models for meandering rivers and related morphodynamic processes*, Rev. Geophys., 45, RG1001.

[25] CONSTANTINESCU, G. S., AND SQUIRES, K. D., 2003. *LES and DES investigations of turbulent flow over a sphere at Re=10000*, J. Flow, Turbul. Combust., 70, 267.

[26] CONSTANTINESCU, G. S., AND SQUIRES, K. D., 2004. *Numerical investigations of flow over a sphere in the subcritical and supercritical regimes*, Phys. Fluids, 16, 5.

[27] CONSTANTINESCU, G., KOKEN, M., AND ZENG J., 2011. *The structure of turbulent flow in an open channel bend of strong curvature with*

deformed bed: Insight provided by detached eddy simulation, Water Resour. Res., 47, W05515.

[28] CONSTANTINESCU, G., KASHYAP, S., TOKYAY, T., RENNIE, C. D., AND TOWNSEND, R. D., 2013. *Hydrodynamics processes and sediment erosion mechanisms in an open channel bend of strong curvature with deformed bathymetry*, J. Geophys. Res. Earth Surf., 118, 1-17.

[29] CROSATO, A., 2008. *Analysis and modeling of river meandering*, PhD thesis, Delft Univ. of Technol., Delft, Netherlands.

[30] CROSATO, A., 2009. *Physical explanations of variations in river meander migration rates from model comparison*, Earth Surf. Processes Landforms, 34, 2078-2086.

[31] DEAN, R. B., 1974. *Reynolds number dependence on skin friction in two dimensional rectangular duct flow and a discussion on the law of the Wake*, Aero Rep. 74-11, Imperial Coll. London, London.

[32] DIETRICH, W. E., AND SMITH, J. D., 1983. *Influence of the point bar on flow through curved channels*, Water Resour. Res., 19(5), 1173-1192.

[33] EINSTEIN, A. H., 1950. *The bedload function for sediment transport in open channel flow*, U.S. Dep. Agric. Tech. Bull. 1026, Washington, D. C.

[34] ENGELUND, F., AND HANSEN, E., 1967. *A Monograph on Sediment Transport in Alluvial Streams*, Dan. Tech. Press, Copenhagen.

[35] FERGUSON, R. I., PARSONS, D. R., LANE, S., AND HARDY, R. J., 2003. *Flow in meander bends with recirculation at the inner bank*, Water Resour. Res., 39(11), 1322.

[36] FRASCATI, A., AND LANZONI, S., 2009. *Morphodynamic regime and long-term evolution of meandering rivers*, J. Geophys. Res., 114, F02002.

[37] FRASCATI, A., AND LANZONI, S., 2010. *Long-term river meandering evolution as a part of chaotic dynamics? A contribution from mathematical modeling*, Earth Surf. Processes Landforms, 35, 7, 791-802.

[38] FRASCATI, A., AND LANZONI, S., 2013. *A mathematical model for meandering rivers with varying width*, J. Geophys. Res. Earth Surf., 118, 1-17.

[39] GERMANO, M., 1992. *The filtering approach*, J. Fluid Mech., 238, 325-336.

[40] HOLMES, M., 1995. *Introduction to Perturbation Methods*, Texts Appl. Math., 20, Springer, New York.

[41] HOOKE, J. M., AND YORKE, L., 2011. *Channel bar dynamics on multi-decal timescales in an active meandering river*, Earth Surf. Processes Landforms, 36, 1910-1928.

[42] HOWARD, A. D., 1992. *Modeling channel migration and floodplain development in meandering streams*, in Lowland Flood-Plain Rivers: Geomorphological Perspectives, edited by P. A. Carling and G. E. Petts, 1-41, John Wiley, Chichester, U. K.

[43] IKEDA, S., PARKER, G., AND SAWAI, K., 1981. *Bend theory of river meanders. Part 1: Linear development*, J. Fluid Mech., 112, 363-377.

[44] ISSA, R. I., 1985. *Solution of the implicitly discretized fluid flow equations by operator-splitting*, J. Comput. Physics, 62, 40.

[45] ISSA, R. I., GOSMAN, A. D., AND WATKINS, A. P., 1986. *The computation of compressible and incompressible recirculating flows by a non-iterative implicit scheme*, J. Comput. Physics, 62, 66.

[46] JASAK, H., 1996. *Error analysis and estimation for the finite volume method with applications to fluid flows*, Phd Thesis, University of London.

[47] JASAK, H., AND WELLER, H., 2000. *Application of the finite volume method and unstructured meshes to linear elasticity*, Int. J. for Num. Meth. in Eng., 48, 267-287.

[48] JASAK, H., AND TUKOVIĆ, Z., 2007. *Automatic mesh motion for the unstructured finite volume method*, Transactions of FAMENA, 30, 2, 1-18.

[49] JEFFERSON, M. S. W., 1902. *Limiting width of meander belts*, Natl. Geogr. Mag., 13, 373-384.

[50] JOHANNESSON, H., AND PARKER G., 1989. *Linear theory of river meanders*, in River Meandering, Water Resour. Monogr. Ser., 12, edited by S. Ikeda and G. Parker, 181-213, AGU, Washington D.C.

[51] KALKWIJK, J. P., AND DE VRIEND, TH. H. J., 1980. *Computation of the flow in shallow river bends*, J. Hydraul. Res., 18, 327-342.

[52] KOKEN, M., CONSTANTINESCU, G., AND BLANCKAERT, K., 2013. *Hydrodynamic processes, sediment erosion mechanisms, and Reynolds-number-induced scale effects in an open channel bend of strong curvature with flat bathymetry*, J. Geophys. Res. Earth Surf., 118, 2308-2324.

[53] LAGASSE, P. F., SPITZ, W. J., ZEVENBERGEN, L. W., AND ZACHMANN, D. W., 2004. *Handbook for predicting stream meander migration*, NHCRP Rep. 533, 107, Natl. Coop. Highway Res. Program, Washington, D. C.

[54] LAGASSE, P. F., ZEVENBERGEN, L. W., SPITZ, W. J., AND ARNESON, L. A., 2012. *Stream Stability at Highway Structures (Fourth Edition)*, Hydraulic Engineering Circular No. 20, Publication No. Fhwa-Hif-12-004, U. S. Department of Transportation, Federal Highway Administration.

[55] LANZONI, S., AND SEMINARA, G., 2006. *On the nature of meander instability*, J. Geophys. Res., 111, F04006.

[56] LILLY, D.K., 1992. *A proposed modification of the Germano subgrid-scale closure method*, Phys. Fluids, A 4, 633-635.

[57] LUCHI, R., BERTOLDI, W., ZOLEZZI, G., AND TUBINO, M., 2007. *Monitoring and predicting channel change in a free-evolving, small Alpine river: Ridanna Creek (North East Italy)*, Earth Surf. Processes Landforms, 32, 14, 2104-2119.

[58] LUCHI, R., BOLLA PITTALUGA, M., AND SEMINARA, G., 2012. *Spatial width oscillations in meandering rivers at equilibrium*, Water Resour. Res., 48, W05551.

[59] LUCHI, R., ZOLEZZI, G., AND TUBINO, M., 2011. *Bend theory of river meanders with spatial width variations*, J. Fluid Mech., 681, 311-339.

[60] LUMLEY, J. L., 1978. *Computational modeling of turbulent flows*, Adv. Appl. Mech., 18, 123-176.

[61] LUND, T.S., AND MOIN, P., 1996. *Large-eddy-simulation of a concave wall boundary layer*, Int. J. Heat Fluid Flow, 17, 290-295.

[62] MONCHO-ESTEVE, I., PALAU-SALVADOR, G., SHIONO, K. AND MUTO, Y., 2010. *Turbulent structures in the flow through compound meandering channels*, Proceedings of River Flow 2010, 1543-1550.

[63] MOSSELMAN, E., 1998. *Morphological modelling of rivers with erodible banks*, Hydrol. Processes, 12, 1357-1370.

[64] MÜNCH, C., AND MÉTAIS, O., 2007. *Large eddy simulations in curved square ducts: Variation of the curvature radius*, J. Turbulence, 8, 290-295.

[65] ODGAARD, A. J., 1986. *Meander flow model. I: Development*, J. Hydraul. Eng., 112, 12, 1117-1136.

[66] ODGAARD, A. J., AND BERGS, M. A., 1988. *Flow processes in a curved alluvial channel*, Water Resour. Res., 24, 45-56.

[67] PARKER, G., DIPLAS, P., AND AKIYAMA J., 1983. *Meander bends of high amplitude*, J. Hydraul. Eng., 109, 1323-1337.

[68] PARKER, G., SEMINARA, G., AND SOLARI, L., 2003. *Bed load at low Shields stress on arbitrarily sloping beds: Alternative entrainment formulation*, Water Resour. Res., 39, 7, 1183.

[69] PARKER, G., SHIMIZU, Y., WILKERSON, G. V., EKE, E. C., ABAD, J. D., LAUER, J. W., PAOLA, C., DIETRICH, W. E., AND VOLLER, V. R., 2011. *A new framework for modeling the migration of meandering rivers*, Earth Surf. Processes Landforms, 36, 70-86.

[70] PETRONIO, A., ROMAN, F., NASELLO, C., AND ARMENIO, V., 2013. *Large eddy simulation model for wind-driven sea circulation in coastal areas*, Nonlinear Processes in Geophys., 1095-1112.

[71] PIZZUTO, J. E., 2008. *Streambank erosion and river width adjustments, in Sedimentation Engineering: Processes, Measurements, Modeling and Practice*, ASCE Manuals Rep. Eng. Pract., 110, edited by M. Garcia, 387-438, Am. Soc. of Civ. Eng., Reston, Va.

[72] PIZZUTO, J. E., AND MECKELNBURG, T. S., 1989. *Evaluation of a linear bank erosion equation*, Water Resour. Res., 25, 5, 1005-1013.

[73] POPE, S. B., 2004. *Turbulent Flows*, Cambridge, UK: Cambridge University Press.

[74] REPETTO, R., TUBINO, M., AND PAOLA, C., 2002. *Planimetric instability of channels with variable width*, J. Fluid Mech., 457, 79-109.

[75] ROZOVSKII, I. L., 1957. *Flow of Water in Bends of Open Channels*, Acad. of Sci. of the Ukrainian SSR, Kiev. (Isr. Program for Sci. Transl., Jerusalem, 1961.)

[76] SCHWARZ, W. R., AND BRADSHAW, P., 1994. *Turbulence structural changes for a three-dimensional turbulent boundary layer in a 30° bend*, J. Fluid Mech., 272, 183-209.

[77] SEMINARA, G., 2006. *Meanders*, J. Fluid. Mech., 554, 271-297.

[78] SEMINARA, G., AND SOLARI, L., 1998. *Finite amplitude bed deformations in totally and partially transporting wide channel bends*, Water Resour. Res., 34, 6, 1585-1598.

[79] SEMINARA, G., AND TUBINO, M., 1992. *Weakly nonlinear theory of regular meanders*, J. Fluid Mech., 244, 257-288.

[80] SEMINARA, G., ZOLEZZI, G., TUBINO, M., AND ZARDI, D., 2001. *Downstream and upstream influence in river meandering. Part 2. Planimetric development*, J. Fluid Mech., 438, 213-230.

[81] SHUR, M. L., SPALART, P. R., STRELETS, M. K., AND TRAVIN, A. K., 1999. *Detached eddy simulation of an airfoil at high angle of attack*, Fourth International Symposium on Engineering Turbulence Modelling and Measurements, Corsica, France.

[82] SILVA LOPES, A., PIOMELLI, U., AND PALMA, J. M. L. M., 2006. *Large-eddy simulation of the flow in an S-duct*, J. Turbulence, 7, 1-25.

[83] SIMONSEN, A. J., AND KROGSTAD, P. -Å., 2005. *Turbulent stress invariant analysis: Clarification of existing terminology*, Phys. Fluids, 17, 088103.

[84] SMITH, J. D., AND MCLEAN, S. R., 1984. *A model for flow in meandering streams*, Water Resour. Res., 20, 1301-1315.

[85] SPALART, P. R., 2000. *Trends in turbulence treatments*, AIAA Paper, 2000-2306, Fluids 2000, Denver.

[86] SPALART, P., 2009. *Detached eddy simulation*, Annu. Rev. Fluid Mech., 41, 181-202.

[87] STOESSER, T., RUETHER, N., AND OLSEN, N. R. B., 2010. *Calculation of primary and secondary flow and boundary shear stresses in a meandering channel*, Adv. Water Resour., 33, 158-170.

[88] STRUIKSMA, N., OLESEN, K. W., FLOKSTRA, C., AND DE VRIEND, H. J., 1985. *Bed deformation in curved alluvial channels*, J. Hydraul. Res., 23, 1, 57-79.

[89] SUN, T., MEAKING, P., JOSSANG, T., AND SCHWARZ, K., 1996. *A simulation model for meandering rivers*, Water Resour. Res., 32, 9, 2937-2954.

[90] TALMON, A. M., STRUIKSMA, N., AND MIERLO, M. C. L. M. V., 1995. *Laboratory measurements of the sediment transport on transverse alluvial-bed slopes*, J. Hydraul. Res., 33, 495-517.

[91] THORNE, C. R., AND RAIS, S., 1985. *Direct measurement of secondary currents in a meandering sand-bed river*, Nature, 315, 746-747.

[92] VAN BALEN, W., BLANCKAERT, K., AND UIJTTEWAAL, W. S. J., 2010. *Analysis of the role of turbulence in curved open channel flow at different water depths by means of experiment, LES and RANS*, J. Turbul., 11(12), 1-34.

[93] VAN BALEN, W., UIJTTEWAAL, W. S. J., AND BLANCKAERT, K., 2009. *Large-eddy simulation of a mildly curved open-channel flow*, J. Fluid Mech., 630, 413-442.

[94] VAN BALEN, W., UIJTTEWAAL, W. S. J., AND BLANCKAERT, K., 2010. *Large-eddy simulation of a curved open-channel flow over topography*, Physics of Fluids, 22, 075108.

[95] VAN RIJN, L. C., 1984. *Sediment transport, part 1: Bed load transport*, J. Hydr. Eng., 110, 1431-1456.

[96] VARDY, A., 1990. *Fluid Principles*, McGraw-Hill, London.

[97] WELLER, H. G., TABOR, G., JASAK, H., FUREBY, C., 1998. *A tensorial approach to computational continuum mechanics using object-oriented techniques*, Computers in Physics, 12, 6, 620-631.

[98] WONG, M., AND PARKER, G., 2006. *Reanalysis and correction of bed-load relation of Meyer-Peter and Müller using their own database*, J. Hydraul. Eng., 132, 1159-1168.

[99] YALIN, M. S., 1992. *River Mechanics*, Pergamon Press, Oxford.

[100] YEN, B. C., 1965. *Characteristics of subcritical flow in a meandering channel*, technical paper, Inst. of Hydraul. Res. Univ. of Iowa, Iowa City.

[101] ZANG, Y., STREET, R. L., AND KOSEFF, J. R., 1994. *A non-staggered grid, fractional step method for time-dependent incompressible Navier-Stokes equations in curvilinear coordinates*, J. Comput. Physics, 114, 18-33.

[102] ZENG, J., CONSTANTINESCU, G., BLANCKAERT, K., AND WEBER, L., 2008. *Flow and bathymetry in sharp open-channel bends: Experiments and predictions*, Water Resour. Res., 44, W09401.

[103] ZOLEZZI, G., GUALA, M., TERMINI, D., AND SEMINARA, G., 2005. *Experimental observation of upstream overdeepening*, J. Fluid Mech., 531, 191-219.

[104] ZOLEZZI, G., LUCHI, R., AND TUBINO, M., 2009. *Morphodynamic regime of gravel bed, single-thread meandering rivers*, J. Geophys. Res., 114, F01005.

[105] ZOLEZZI, G., LUCHI, R., AND TUBINO, M., 2012. *Modeling morphodynamic processes in meandering rivers with spatial width variations*, Rev. Geophys., 50, RG4005.

[106] ZOLEZZI, G., AND SEMINARA, G., 2001. *Upstream influence in erodible beds*, Phys. Chem. Earth, Part B, 26, 1, 65-70.

Acknowledgements

My boyfriend, who always believes in me and has constant supported me all these years, despite the weight of distance.

Finally, I gratefully acknowledge the Prof. K. Blanckaert for the experimental data supplied to me and the Italian computing center CINECA for providing the computer time.

Thank you